TECHNISCHE UNIVERSITÄT MÜNCHEN

Lehrstuhl für Numerische Mechanik

Modeling and experimental investigation of the mechanobiological environment associated with alveolar pneumocytes

Robert W. Metzke

Vollständiger Abdruck der von der Fakultät für Maschinenwesen der Technischen Universität München zur Erlangung des akademischen Grades eines

Doktor-Ingenieurs (Dr.-Ing.)

genehmigten Dissertation.

Vorsitzender:	Univ.-Prof. Dr.-Ing. Michael W. Gee
Prüfer der Dissertation:	1. Univ.-Prof. Dr.-Ing. Wolfgang A. Wall 2. Prof. Mohammad R. K. Mofrad, Ph.D. University of California Berkeley / USA

Die Dissertation wurde am 10. Dezember 2013 bei der Technischen Universität München eingereicht und durch die Fakultät Maschinenwesen am 13. Oktober 2014 angenommen.

Acknowledgment

More than 10 years ago I was sitting in a confined office space in Cambridge, when my former supervisor asked me to take care of a visiting professor from my home university in Munich. Surprisingly, I didn't know him and my former supervisor began to doubt whether I really am from this university in Munich. It turned out the visitor was new to my university, but he was instrumental to my decision to work in industry after graduation. He introduced me to a new way of thinking about biomechanics which I had missed all the years I was in Munich and which was one reason why I ended up spending so much time abroad. Immediately captivated by his fascinating ideas, I decided to participate in his work. The result of this adventure is much more than the thesis at hand, but an interesting and character-shaping experience for me. The visitor was Prof. Wolfgang A. Wall, my Ph.D. advisor and an inspiring example for me to date. I would like to thank him for all the lessons I learned from him.

There is another person I would like to thank: Prof. Mohammad R. K. Mofrad. He was much more than a co-advisor and kind host for me when I spent some weeks working on my research in his lab. He was constantly a source of inspiration for me and his encouraging words helped me more than everything else. I would like to thank the Bavarian Research Foundation for the kind financial support during my stay in Berkeley.

Working at the Institute for Computational Mechanics in 2004 was a wild time; our group built everything more or less from scratch. There are countless stories of events which welded this first generation of assistants together. My gratitude goes to all of them. I would especially like to thank Dr. Burkhard Bornemann for all the long discussions about principal invariants, industrial design, steel frames and so much more. Thanks also to Dr. Burkhard for introducing me to road biking, which has become a big passion in my life.

I have had the luck in my life to work with a lot of inspiring persons, and not only in Munich or Berkeley. My special thanks to Prof. Lim Chwee Teck for showing me a completely new engineering world. My

time at the Nano Biomechanics Lab will never be forgotten. Another milestone in my development was my stay at the Mechanobiology Laboratory of Prof. Roger D. Kamm. I will always remember this visit as one of my most inspiring experiences.

Finally, I would like to thank my family. My father, mother and sisters supported me all the time. Your moral support was and is most welcome and acknowledged. But my biggest gratitude goes to my wife Yuree and my kids Jenny, Leoni and Klara. The countless hours they had to spend without me and the many weekends when I had no time for them are over forever. I hope that we can spend so much more time together in the mountains and places all around the world. Thank you for your understanding and for holding on with me. I love you.

Traunstein, December 2014 Robert Metzke

Abstract

In this work mechanical stimulus, transferred from biological tissue to alveolar cells due to natural or forced breathing and its relevance to mechanobiology, has been investigated. The mechanical stimulus is measured in terms of the local tissue strain. This alveolar strain was investigated with a stress-strain machine and fluorescence microscopy. It was found that the localized tissue strain is around 15% for an external strain of 30%, or an equivalent intrapulmonary pressure of 20 cmH_2O. The alveolar strain is transferred to cells which adhere to the tissue matrix. In order to simulate in silico the intracellular stresses and strains in the parenchym, a cell material model was formulated based on the mechanical description of the main mechanical constituents. The material model is based on strain energy density functions and was enhanced with a term modeling the contraction of the cell. The distinctive connections between cells and tissue, the focal adhesions, have been modeled by a continuum model enhanced by molecular information. Since focal adhesions are of great importance for the strain transfer, the mechanical behavior of single integrin to collagen bonds has been resolved with molecular dynamics. The molecular dynamics results have been connected to Finite Element simulations achieving a more detailed and accurate mechanical description of focal adhesions. It was possible to reproduce single unbinding events around the metal ion binding site. The unbinding forces were validated with the help of the well-described water dimer and lay in range of experimental results. The presented models and experimental results enable an improved insight into the mechanobiological environment of alveolar pneumocytes, and, hopefully, will serve as a step towards a complete understanding of signal transduction and mechanobiology of the lung.

Zusammenfassung

In dieser Arbeit wurde die mechanische Dehnung des Parenchyms aufgrund natürlicher Atmung oder künstlicher Beatmung und seine Relevanz für mechanobiologische Vorgänge untersucht. Zur Durchführung der Untersuchung wurden alveolare Dehnungen mit einer uniaxialen Zugmaschine aufgebracht und einzelne Alveolen per Fluoreszenzmikroskopie aufgenommen und ausgewertet. Im Ergebnis wurde festgestellt, dass die direkt an den Alveolen gemessene Dehnung circa 15% entspricht, bei einer von der Zugmaschine aufgebrachten Dehnung von 30%. Letzteres entspricht einem transpulmonaren Druck von 20 cmH_2O. Diese Dehnung wird von den Alveolen zu den Zellen transferiert, die an der extrazellulären Matrix anhaften. Um intrazelluläre Spannungen und Dehnungen zu simulieren, wurde eine mechanische Beschreibung für adhärente Zellen entwickelt, die auf den wichtigsten mechanischen Bestandteilen der Zelle aufbaut. Die Formulierung dieser Beschreibung wurde hier um eine Funktion erweitert, die die Kontraktion der Zelle berücksichtigt. Die charakteristischen Verbindungen zwischen Zelle und Gewebe, die sogenannten fokalen Adhesionen, wurden mit einem Ansatz simuliert, der die kontinuumsmechanische Materialbeschreibung mit molekularen Informationen anreichert. Da die fokalen Adhesionen eine wichtige Funktion bei der Übertragung der Dehnung haben, wurde eine einzelne Bindung zwischen einem Integrin und einer Kollagenfaser mit einer molekulardynamischen Simulation aufgelöst. Im Anschluss wurden die molekulardynamischen Ergebnisse dann mit einer Finiten Element Simulation verknüpft, um eine detailliertere mechanische Beschreibung der Verbindung zu erreichen. Die errechneten Kräfte wurden schließlich mit Hilfe des in der Literatur gut beschriebenen Wasserdimers validiert und liegen im Bereich von experimentellen Ergebnissen. Die in der vorliegenden Arbeit erarbeiteten Algorithmen und Ergebnisse geben eine verbesserte Einsicht in die mechanobiologische Umgebung von alveolaren Pneumozyten. Auf lange Sicht dienen sie hoffentlich einem tieferen Verständnis der Signaltransduktion und Mechanobiologie in der menschlichen Lunge.

Contents

Chapter 1

Alveolar biomechanics in the perspective of mechanical ventilation

In recent years procedures in hospitals have improved constantly and allowed the successful treatment of patients with severe illnesses, which were hardly treatable before. These improvements come very often with an increased number of patients requiring mechanical ventilation due to longer treatment periods in intensive care units. This development has placed new focus on ventilation strategies. While there is no doubt that mechanical ventilation is absolutely necessary to ensure oxygen saturation of the patient's blood, it has emerged more and more that mechanical ventilation itself can also harm patients, especially when they are ventilated over a longer period of time. The Acute Respiratory Distress Syndrome network [139] has found that over-stretching alveolar tissue by large tidal volumes increases mortality of patients with acute lung injury (ALI) or acute respiratory distress syndrome (ARDS). The tidal volume is hereby defined as the gas volume which is applied to the patient's lung by mechanical ventilators. The study was stopped after preliminary results found that the group with the lower tidal volume showed decreased mortality as compared to the group with the traditional tidal volume. The difference between the tradi-

tional group and the group with the lower tidal volume was 8.8% in mortality [139]. This study shows impressively how improved mechanical ventilation strategies can influence patient's outcome.

One important question which arises from the ARDS network study is how the tidal volume is connected to biochemical processes such as inflammation inside the lung. To narrow down this question, it is necessary to take a look at lung alveoli and biochemical processes. The lung consists typically of 700 million alveoli which are located in the respiratory zone of the lung. Here, the gas exchange with the blood takes place. But how do alveoli connect back to parameters of a mechanical ventilator? During mechanical ventilation, the patient is connected to the ventilator through an endotracheal tube which is placed in the lower airways. The ventilator pushes either pressure or volume controlled air into the lung to ensure oxygen supply for the blood. This procedure is actually in contrast to breathing where a negative pressure between the diaphragm and the lung inside the chest sucks air into the lung. In order to control the ventilation process, physicians can either regulate the air volume (tidal volume) or the maximum pressure. By using large tidal volumes or high pressures, the air volume applied to the lung is larger than by normal breathing. As a consequence alveolar tissue is over-stretched. Consequences of this treatment may be the disruption of tissue or cells in the alveoli (ventilator induced lung injury; VILI) or the beginning of an inflammation in the alveoli (ARDS). One could argue that by reducing the tidal volume or pressure, this can be avoided. But unfortunately it is not simply possible to reduce the tidal volume or the pressure, because on the other hand, the oxygen saturation in the blood must be sufficiently high enough for the patient to survive. This makes it so important for the physician to choose on the one hand a ventilation strategy which ensures sufficient oxygen saturation in the blood and on the other hand a ventilation strategy which treats the lung with care. This fine line, which physicians need to balance every day, makes it important to investigate in detail how alveoli react to mechanical ventilation and how alveolar tissue is deformed when the alveolar volume is increasing. The latter point can help to understand, what the cause of VILI or ARDS might be.

The deformation of the alveolar tissue and constituents of the tissue

is hereby in part a biomechanical question as it requires mechanical descriptions of the alveolar tissue and cells. The following section gives an overview of important mechanical constituents of the lung as the biological basis to build mechanical models.

1.1 The biomechanical composition of the lung

Fredberg and Kamm [52] are proposing that the transfer of stresses and strains is taking place at a wide range of scales from organ to cell in the lung. Here, emphasis is placed on lung tissue, alveolar cells and the interface between tissue and cells.

1.1.1 Lung tissue

The lungs are a pair of cone shaped, highly elastic and spongy organs located in the chest. They are the main organs of the respiratory system. The lungs stretch from the clavicles down to the edge of the rib cage, and are composed of lobes. The right lung has three lobes, while the left lung has only two. The lobes itself are divided into functional subunits, called lung segments. The lung segments are composed by parenchym and small airways. The whole organ is surrounded by the pleura. The pleura is divided into two components, the pleura parietalis and the pleura visceralis. The first one is directly connected to the parenchym while the latter one is connected to the rib cage. Inbetween both pleuras is a fluid film allowing the lung to move relatively to the rib cage without much friction.

The lung is a collection of different systems and tissues. The two most important systems are the respiratory system and the pulmonary blood circuit. Both systems contribute to the mechanical environment of the lung. The respiratory part itself can be divided again into three different scales: the lower airways with supporting cartilage inside the walls up to the 20th generation of airways, the lower airways without any mechanical supporting structures, and the parenchym, the tissue at the scale of the air-blood interface, forming alveoli. From a modeling point of view the important constituents are small airways (bronchioles), the blood circuit around alveoli and, most important, the alveolar

tissue.

Small airways The composition of small airways is given by Benninghoff et al. [12]. Additional information can be found at Netter et al. [105].

The airways are constructed by layers. The first layer (starting from inside) is the epithelial layer with the cilia. The epithelial layer is not always smooth within the airway. It exhibits sometimes a folded structure. The mechanical influence of this layer is limited predominantly to cellular properties. The epithelial layer is placed on a basement membrane with a longitudinal fiber orientation. Behind the basement membrane, a layer of smooth muscle cells is located. The muscle cells are linked to the surrounding parenchym by connective tissue. Interestingly, the muscle cells are not circularly orientated in the airway, but have a screw like thread.

Lung blood circuit The lung blood circuit is made up from pulmonary arteries and pulmonary veins. Both blood vessels belong to the low pressure circuit of the body. The mechanical properties of the artery down to the capillary and back to the vein are that of soft tissue. The pulmonary artery is following the bronchial tree, whereby the pulmonary vein is following the surfaces of the different lung segments. Both blood vessels consist of connective tissue with some muscle parts. Instead of a membrane they feature a light fiber net. Due to the structural composition of the lung blood vessels, they do not contribute significantly on a global scale to lung mechanics. Locally however they might play a role especially when the pressure in the capillaries is increased. The influence of the pressure was shown recently by Albu et al. [3].

Alveolar tissue As soon as 1972 Sugihara et al. [130] speculated about the influence of the fiber system and how the different components contribute to the macroscopic behavior of lung tissue. The difficulty in measuring mechanical behavior, of the parenchyma or even single alveolar walls, was the starting point for material models which are based on the microstructural composition of lung tissue. The main constituents were defined recently by Suki et al. [132]:

- Collagen (mainly type I and III)
- Elastin
- Proteoglycans
- Type I and type II pneumocytes, alveolar macrophage

Beside these structural elements of parenchyma, there exists a fluid surface film in the alveoli called surfactant. The function of the surfactant is to reduce the surface tension in the alveoli.

Collagen and elastin The importance of collagen and elastin for the mechanical properties of lung tissue has been known for a long time. In recent years a new functionality of collagen and elastin fibers emerged: a regulatory function to transfer forces to the cellular level. Suki et al. [132, 133] speculated about the role of mechanical forces in terms of biological functions. Firstly, Suki identified collagen as the main load bearing element in the alveolar wall. The influence of muscle cells in the lower airways was also recognized, but was found not to be as important as collagen. Interesting is that Suki concentrated on collagen alone and not on elastin which is supposed to be the dominant load bearing element in case of small strains. Secondly, Suki looked into the effect of proteases, inflammation and mechanical forces on emphysema with emphasis on collagen, the regulatory function of the fiber system. It was found that imbalance of protease and anti-protease as well as inflammation can lead to emphysema. The spreading of emphysema is then enhanced by mechanical forces.

By using collagenase and elastase Yuan et al. [154, 155] investigated the influence of fibers on the overall mechanical behavior of alveolar tissue. Both treatments resulted in a decrease of storage and loss modulus of the tissue, whereby the hysteresis remained constant. Similar results have been found by Moretto et al. [103] by applying elastase to lung tissue strips.

Proteoglycans Proteoglycans are molecules made up of a protein core with attached Glycosaminoglycans (GAG). Glycosaminolycans are long unbranched carbohydrate chains with negatively charged areas, closely packed, and cause large electrostatic repulsive forces.

The influence of proteoglycans on lung tissue was shown by Jamal et al. [72] and Cavalcante et al. [25]. Jamal measured the change in viscoelastic behavior due to inhibition of GAGs. By degrading specific GAGs (chondroitin sulfate and dermatan sulfate) the viscoelastic behavior of lung tissue changed by increased energy dissipation while resistance stayed constant. This finding is very interesting because, considering GAGs are the interconnection of fibrils, one would expect that resistance is decreased and less energy is dissipated when some of them are missing. But as shown, the opposite is the case. The degradation of another GAG (heparan sulfate) did not show any influence on the viscoelastic tissue behavior.

Cavalcante et al. [25] looked into the influence of the electrostatic environment. By changing the media from hypotonic to hypertonic and measuring the mechanical properties it was found that the stress-strain curve is shifted to the right. A possible explanation of this shift might be found in inflating and deflating GAGs. GAGs inflate by increasing electrostatic forces and deflate by decreasing electrostatic forces, caused by the media change. Taking into account that osmolarity has no influence on collagen and elastin, currently only shown for cartilage, the finding would mean that only proteoglycans are regulated by osmolarity.

1.1.2 Alveolar cells

Cells play an important regularity role in the parenchym [57, 143] but no dominant mechanical role. But the fact that cells are one possible origin of signal pathways made their role as mechanosensors more important in recent times [143]. For mechanosensors, even small forces can make a difference and cell deformation may contribute to micromechanical properties, perhaps not directly but indirectly [9].

In the parenchym mainly the following types of cells can be found:

Bronchioles:	Alveoli:
Goblet cells	Type I pneumocytes
Clara cells	Type II pneumocytes
Muscle cells	Alveolar macrophages
	Fibroblasts
	Endothelial cells in the blood vessels

Table 1.1: Cell types in bronchioles and alveoli

Type I pneumocytes are the "cloth" of alveoli. They line the inner part of alveoli and are stretched cells shaped like a thin foil. Type II pneumocytes are located in between type I cells and have the important obligation to produce surfactant. They are entitled as well as defenders of alveoli and fulfill several biological functions as e.g. proliferation and innate immunity [92]. But by numbers, they are smaller than type I cells. Both cells together represent the epithelial layer.

Alveolar macrophages are the "vacuum cleaner" of the lung. They transport molecular products, such as non-functional surfactant, away from the alveoli into the interstitium. For that reason they are able to move.

Fibroblasts are located in the basal membrane or interstitium and are responsible for producing the molecular building blocks for the fiber system.

Finally there are endothelial cells on the surface of the capillaries as in all blood vessels.

Mechanically, cells consist of a hard nucleus, an actin filament network, and a plasma membrane [15]. The mechanical properties, especially of the actin network, was the focus of a lot of recent research work [15, 157, 86, 31] and shall not be discussed in detail here.

Mechanical properties of epithelial cells Epithelial cells have been mechanically characterized by Trepat et al. [140, 141]. The complex shear modulus $G^* = G' + jG'' = G'(1 + j\eta)$ of the cells was measured with the magnetic twisting technique. The cells were treated with thrombin and the underlying collagen gel was stretched as well. The results for the mechanical properties of the cell are given as follows:

Trepat et al. 2004	G' $[Pa/\mu m]$	G'' $[Pa/\mu m]$
baseline	722 ± 83	231 ± 27
stretched (14.3 %)	~ 1184	~ 300
Trepat et al. 2006	G' $[Pa/nm]$	η
confluent cells	1.20 ± 0.06	0.344 ± 0.007
subconfluent cells	1.03 ± 0.06	0.336 ± 0.006

Table 1.2: Mechanical properties of alveolar epithel cells for unstretched (baseline) and stretched substrate from Trepat et al. [140, 141]

It should be mentioned that Trepat et al. seeded the cells on gel which might influence the mechanical behavior of the cells. All measurements were conducted by a frequency of $f = 1\ Hz$. One interesting result is that mechanical properties changed with increasing underlying strain, which indicates a non-linear behavior of cells.

Magnetic twisting				
C $[pN \cdot \mu m]$	444 ± 6	768 ± 18	987 ± 29	1205 ± 46
$E[Pa]$	34 ± 4.7	46 ± 7.4	51 ± 7.0	58 ± 9.0
τ $[s]$	–	1.2 ± 1.1	1.3 ± 0.4	1.5 ± 0.9
Optical tweezer				
C $[pN \cdot \mu m]$	$0 - 400$	–	–	–
$E[Pa]$	125 ± 72	–	–	–
τ $[s]$	3.1 ± 2.0	–	–	–

Table 1.3: Mechanical properties of alveolar epithel cells from Laurent et al. [83]. C is the applied torque, E the Young's modulus and τ the relaxation time.

In order to compare different techniques, Laurent et al. [83] used epithelial cells to measure the mechanical properties with the magnetic twisting and optical tweezer technique. The results for the Young modulus E and the relaxation time τ are given in Table 1.3. The relaxation time τ is related to elasticity E and viscosity η by $\tau \approx 3\eta/E$.

Using a third common technique, Rico et al. [113] reported the mechanical results for epithel cells using Atomic Force Microscopy (AFM). In the experiments, they calculated the Young modulus E and storage modulus G' and loss modulus G'' as shown in Table 1.4.

	$E[kPa]$	$G'[kPa]$	$G''[kPa]$
pyramidal tip	0.91 ± 0.47	0.32 ± 0.16	0.07 ± 0.03
spherical tip	0.47 ± 0.18	0.15 ± 0.07	0.03 ± 0.02

Table 1.4: Mechanical properties of alveolar epithel cells measured by AFM with two different tips from Rico et al. [113]

A nice overview of additional measurements can be found at Dailey et al. [39].

1.1.3 Connection of alveolar cells to tissue

Cells interact with their environment in several ways, e.g. biochemically, mechanically, etc. In the case of soft tissue the mechanical interaction of cells takes place mainly with the Extra-Cellular Matrix (ECM). The interaction can come from the ECM or the cell. The first possibility, from the ECM, is straight-forward to understand. When the ECM is stretched, attached cells will be stretched as well. The second interaction possibility, from the cell to the ECM, is not so obvious. A mechanical change in the cell can be sensed by the ECM and can start a change in mechanical properties of their collagen substrate [48].

In a recent review from Ingber [70], an overview of mechanical pathways is given. Ingber argued in his review that a view on all scales is necessary to understand mechanotransduction and that the force transfer from tissue to cells plays an important role and is insufficiently studied up to now. Especially prestress, or, perhaps better expressed, balance of forces within tissue and cells plays an important role. The distortion of this balance may lead to mechanotransduction as shown for the hearing mechanism [67, 70]. But what magnitude of force would

be expected to arrive at the cell? Curtis [35] looked into that subject by comparing different measurement methods, all based on cells seeded on substrates. He comes to the conclusion that a minimum force of 1 nN can be detected by cells between substrate and cellular membrane. In terms of the force direction he concludes that the force is approximately aligned along the principal axis of an elongated cell. Using another technique, Curtis was able to measure the forces exerted on the surroundings of the cell. For fibroblasts, he measures forces in the pN range up to 30 μm away from the cell. These investigations give some feeling about the magnitude of forces which exist at the cellular level. But how exactly is the force transferred from the ECM to the cell membrane and further on into the cell?

For the trans-membrane transmission of forces, focal adhesions play a vital role. Focal adhesions consist of hundreds of proteins and serve primarily as an anchor for cells. Their function is not limited to anchorage of cells, but they are signal carriers as well. The connection between focal adhesions and the ECM generally includes integrins. Integrins are trans-membrane proteins which are built of two different molecular subunits, α and β. There are eight known β subunits and 18 known α subunits, which can form 24 distinct integrins [40]. Not all combination dock directly onto the cytoskeleton, the intra-cellular fiber network, and/or are involved in mechanotransduction [66]. For instance, lung carcinoma cells can use either the $\alpha_v\beta_3$ or $\alpha_v\beta_5$ integrin to attach to vitronectin. On the other side, Extra-Cellular Matrix proteins own normally a distinct motif of recognition [82]. Collagen I is known to be one of those proteins. Clark et Brugge [32] gave an overview of some different combinations, summarized in Table 1.5, for ECM binding partners.

Integrin	Charateristics
β_1	lntegrin receptors containing the β_1 subunit and any 1 of 10 α subunits; ECM ligands include fibronectin, laminin, collagen, and vitronectin.
β_2	lntegrin receptors containing the β_2 subunit; found in leukocytes; mainly involved in cell-cell adhesion; ligands include ICAMs and fibrinogen.

β_3	lntegrin receptors containing the β_3 subunit and any one of two α subunits; ligands include fibrinogen and vitronectin.

Table 1.5: Transmembrane integrins and extracellular binding partners; adopted from [32].

Elastin binds to the elastin receptor of the cell membrane, which is build up by the elastin binding protein (EBP) and two additional surface proteins. EBP is also responsible for the intracellular transport of tropoelastin, the structural element of elastin [115]. But besides the elastin receptor, recently a couple of other receptors have been identified to bind to elastin: G protein coupled receptors (through elastonectin, a 120 kDa glycoprotein) and integrins. Hereby, it is not clear up to now if only tropoelastin is binding to the $\alpha_v\beta_3$ integrin or whole elastin fibers.

Beside the ECM-cell connection, cells are connected to each other as well, e.g. in the epithelial monolayer. Cell-cell contacts take place through cadherins and gap junctions. This connections can be disrupted by over-stretching, which was shown for pulmonary endothelial cells by Birukova et al. [14]. Confluent cell cultures, seeded on collagen I gel, were stretched to 5% and 18%. In the experiments high stretches resulted in a decrease in gap formation. The same is proposed for epithelial cell cultures on collagen substrates, whereby it is not clear if detaching from the substrate or detaching from neighboring cells was observed [140]. The applied stretches were around 18% as well. All stretches mentioned here apply to cyclic stretch applied to the substrate. Actual stretches of substrate and membrane are, depending on the experimental setup, probably lower.

1.2 Three hypotheses of possible signal pathways in alveoli

Mechanical stimuli applied to cells or tissue are only half of the story of mechanotransduction. After the cell is exposed to the stimuli, the

cell eventually answers with a biochemical reaction, a signaling cascade. From an engineering viewpoint, the cell behaves much like a sensor. This process, the transformation of a mechanical stimulus to a biochemical reaction, is not yet fully understood. Only parts of possible signaling pathways could be revealed in recent years. Here three possible signaling pathways in alveoli are discussed.

First of all, it is known that the disruption of the cell membrane and the following discharge of intra-cellular proteins leads to inflammation of neighboring cells. This disruption of the cell membrane can be, for instance, caused by mechanical ventilation. Let's assume a partial lung inflammation where only certain alveoli are taking part in gas exchange. In order to ensure sufficient oxygen saturation in the blood, the pressure (or volume) of the mechanical ventilator must be increased. Remaining healthy alveoli need to take over the work of diseased alveoli. The increased pressure leads to an over-stretching in healthy parts of the lung and can damage the epithelial layer in healthy alveoli. The disruption of cell membranes by over-stretching was shown by Gajic et al. [53]. Following the disruption different cytokines are released and can start an inflammation.

Secondly, cells are not disrupted, but part of the extracellular matrix is disrupted. Damage of the extracellular matrix due to high tidal volumes was shown by Pelosi et al. [107]. Especially two proteoglycans, versican and perlecan, have been identified as possible origins for the beginning of an inflammatory process. The idea of this extra-cellular signaling pathway is that over-stretching parenchym results in release and disruption of proteoglycans. These proteoglycans can dock to receptors on the cell membrane and start an inflammation.

Third, inflammatory processes cannot only start by tissue or cell damage. Another possibility is that the mechanical stimulus is transferred to the intracellular lumen through the cell membrane or to the cell membrane itself [143], where again, inflammatory pathways can start. With respect to cell membranes, one possible pathway is related to stretching the cell membrane. Caveolae on the membrane are opened and receptors are then able to dock onto the cell membrane.

Regarding the force transfer to the intracellular lumen, one can look directly at integrins. The stimulus is transferred from the extra-cellular matrix to the actin network by integrins and intracellular proteins, as

e.g. FAK or FAT, associated to integrins. Then a biochemical reaction is started inside the cell.

These are all complicated processes within alveoli which require an exact and appropriate mathematical description in case models shall help to understand possible signaling pathways. Therefore the next section introduces essential principles of continuum and molecular mechanics, which build the foundation for the later derived models.

1.3 A brief introduction to continuum and molecular mechanics

Physical bodies consist of atoms which are connected through a series of weak and strong bonds. Except some manufactured materials as e.g. graphene sheets, all real materials are inhomogeneous on an atomistic scale. In order to understand and model the mechanical behavior of these bodies it is very often unnecessary to model atoms and their interaction themselves. Deformations and stresses can be described in a phenomenological way with the method of continuum mechanics, where the body of interest is described as a continuous medium. The atomistic structure is hereby replaced by field quantities such as density, temperature and velocity. Here only a brief introduction to the basic principles is presented. For a more comprehensive insight into the mechanics of continua the reader is referred to Holzapfel [60] or Bonet and Wood [16].

Tissue and even cells can be described as a continuous medium because the body of interest is large compared to atoms and their bonds. For that reason, using the continuum mechanics framework to describe the mechanics of alveolar tissue and alveolar cells is sufficiently accurate for overall behavior. But the connections between cell and tissue, the integrins, are in a similar magnitude as atomistic bonds. This makes it interesting to look at the atomistic structure of these proteins for two reasons. First, single atomistic bonds play an important role in the mechanics of integrins, which makes the body inhomogeneous. Second, the experimental derivation of parameters to describe integrin mechanics within the continuum framework is difficult. For that reason molecular dynamics simulations are used to simulate integrins.

The second part of this section gives a brief introduction to molecular mechanics which is used later on to derive material parameters for the integrin. An extensive overview of molecular dynamics simulations is given e.g. by Haile [56].

1.3.1 Continuum mechanics

The continuum mechanics section first introduces kinematics of continuous bodies. Following kinematics, the concept of invariants is highlighted. Next, a short introduction to the stress concept is given. Finally, the section finishes with a very brief description of the governing equations.

Kinematics The continuous body of interest is denoted by $\mathcal{B} \subset \mathbb{R}^3$, parameterized in $\boldsymbol{X}$, in the reference configuration. In the current or actual configuration it is denoted by $\mathcal{S} \subset \mathbb{R}^3$, parameterized in $\boldsymbol{x}$. With the nonlinear deformation map $\varphi_t : \mathcal{B} \to \mathcal{S}$ at time $t \in \mathbb{R}_+$ points $\boldsymbol{X} \in \mathcal{B}$ are mapped onto points $\boldsymbol{x} \in \mathcal{S}$. The important gradient $\boldsymbol{F}$ of the deformation is defined by

$$\boldsymbol{F}(\boldsymbol{X}) = \nabla \varphi_t(\boldsymbol{X}) = \frac{\partial \boldsymbol{x}}{\partial \boldsymbol{X}}. \tag{1.1}$$

The deformation gradient $\boldsymbol{F}$ is a two field tensor because one basis vector ($\boldsymbol{x}$) is associated to the actual configuration while the other basis vector ($\boldsymbol{X}$) is associated to the reference configuration. The deformation gradient is not allowed to be singular to make sure that the transformation map is one-to-one. In order to ensure the local invertibility, a sufficient condition is that the determinant of the deformation gradient $\boldsymbol{F}$ is unequal zero. Together with the continuity of $\varphi_t(\boldsymbol{X})$ the Jacobian J can be postulated to be strictly positive.

$$J(\boldsymbol{X}) := \det[\boldsymbol{F}(\boldsymbol{X})] > 0 \tag{1.2}$$

The physical interpretation of the positive Jacobian J is that a body cannot penetrate itself. The deformation of an infinitesimal line element $d\boldsymbol{x}$, which is mapped from its reference configuration to the current configuration, is written with help of the deformation tensor in the following form:

$$d\boldsymbol{x} = \boldsymbol{F} d\boldsymbol{X}. \tag{1.3}$$

In a similar way, the mapping of an infinitesimal area $d\boldsymbol{A}$ in its reference configuration to the area $d\boldsymbol{a}$ in its actual configuration can be written with the deformation tensor via Nanson's formula:

$$d\boldsymbol{a} = \mathrm{cof}[\boldsymbol{F}] d\boldsymbol{A} \tag{1.4}$$

with the cofactor of $\boldsymbol{F}$ defined as $\mathrm{cof}[\boldsymbol{F}] = det[\boldsymbol{F}]\boldsymbol{F}^{-T}$. Using an area element and a line element to calculate a volume, the volume in the actual configuration $d\boldsymbol{v}$ can be related as

$$d\boldsymbol{v} = \det[\boldsymbol{F}] d\boldsymbol{V} \tag{1.5}$$

with $d\boldsymbol{V}$ its volume in the reference configuration.

One important deformation tensor, the symmetric right Cauchy-Green tensor $\boldsymbol{C}$ is based on the square of the infinitesimal line element $d\boldsymbol{x}$ or $d\boldsymbol{X}$ respectively.

$$\boldsymbol{C} := \boldsymbol{F}^T \boldsymbol{F} \tag{1.6}$$

In the same manner the left Cauchy-Green tensor $\boldsymbol{b}$ is denoted as

$$\boldsymbol{b} := \boldsymbol{F} \boldsymbol{F}^T. \tag{1.7}$$

Taking the difference between the square of the line elements of the actual and reference configuration ($d\boldsymbol{x} \cdot d\boldsymbol{x} - d\boldsymbol{X} \cdot d\boldsymbol{X}$) the Green and the Almansi strain tensor can be written as

$$\boldsymbol{E} := \frac{1}{2} \left(\boldsymbol{C} - \boldsymbol{I} \right) \text{ and } \boldsymbol{e} := \frac{1}{2} \left(\boldsymbol{I} - \boldsymbol{b}^{-1} \right) \tag{1.8}$$

with the identity tensor $\boldsymbol{I}$.

Invariants Looking at second-order isotropic tensor functions $\boldsymbol{f}$ which are dependent of first, second (e.g. strain tensors) or higher order tensors, the representation theorem states that each isotropic tensor function can be expressed by scalar valued invariants I_k [79, 78]. Especially for description of the mechanical behavior of materials, the

second-order tensor $\boldsymbol{C}$ shall be used as an example. The invariants of the tensor $\boldsymbol{C}$ are determined by the characteristic polynomial

$$\det[\tilde{\lambda}\boldsymbol{I}-\boldsymbol{C}] = \sum_{k=0}^{3} (-1)^k \, I_k \tilde{\lambda}^{3-k} = I_0\tilde{\lambda}^3 - I_1\tilde{\lambda}^2 + I_2\tilde{\lambda}^1 - I_3\tilde{\lambda}^0 = 0 \quad (1.9)$$

with the eigenvalues $\tilde{\lambda}$ of $\boldsymbol{C}$. Since $I_0 = 1$ and $\tilde{\lambda}^0 = 1$, the principal invariants I_k, $k = 1, 2, 3$, of the second order tensor $\boldsymbol{C}$ are explicitely given by

$$I_1 := \mathrm{tr}[\boldsymbol{C}], \; I_2 := \mathrm{tr}[\mathrm{cof}\boldsymbol{C}], \; I_3 := \det[\boldsymbol{C}]. \quad (1.10)$$

In order to model anisotropic behavior of materials, an anisotropic invariant J_4 is introduced. The orientation of the anisotropic direction varies according to an orientation density distribution. A general structural tensor $\mathbf{H}$ is introduced following Gasser et al. [55] (exemplarily for the case of a transversely isotropic material with preferred direction $\boldsymbol{h}$) with

$$\mathbf{H} = \kappa\mathbf{I} + (1 - 3\kappa)\, \boldsymbol{h} \otimes \boldsymbol{h}. \quad (1.11)$$

Thereby, κ represents a parameter, which can be derived from the orientation density distribution function $\rho(\theta)$.

$$\kappa = \frac{1}{4} \int_0^{\pi} \rho\,(\theta) \sin^3\,(\theta)\, d\theta \quad (1.12)$$

The parameter κ is hereby a simple scalar measure for the degree of anisotropy of the material. The parameter is defined between $\kappa = 0$ for a completely anisotropic material and $\kappa = \frac{1}{3}$ for a homogeneous material.

The new anisotropic invariant J_4 of the right Cauchy-Green tensor is defined by

$$J_4 = \mathrm{tr}(\boldsymbol{H} \cdot \boldsymbol{C}). \quad (1.13)$$

The invariant J_4 is a so-called mixed invariant. More structural mixed invariants can be constructed by, e.g., using $\boldsymbol{C}^2$ instead of $\boldsymbol{C}$ in equation (1.13). The reader is referred to Spencer [128] for more information

and references given there.

For convenience, the derivatives of the invariants I_1, I_3 and J_4 with respect to $\boldsymbol{C}$ are given here:

$$\frac{\partial I_1}{\partial \boldsymbol{C}} = \boldsymbol{I},\ \frac{\partial I_3}{\partial \boldsymbol{C}} = \boldsymbol{C}^{-1},\ \frac{\partial J_4}{\partial \boldsymbol{C}} = \boldsymbol{H}^T \tag{1.14}$$

Stress concept Physical bodies are normally deformed by external forces. The occurring internal loading is generally described by the notion of stresses. Taking an arbitrary cross-section through a continuous body, the resulting loading depends on the orientation of the cross section. The orientation of the load vector is hereby described by the orientation of the normal vector $\boldsymbol{n}$, perpendicular to the cross-section. Defining the load vector as a measure of average force per unit area, the stress vector $\boldsymbol{t}$ can be written as load vector. Both notations are in the actual configuration. For a more general formulation it would be preferable to have a notation of stress which does not depend on the normal vector. For that reason the stress tensor is denoted in the following form:

$$\boldsymbol{t} = \boldsymbol{\sigma}\boldsymbol{n}, \tag{1.15}$$

which maps the normal vector to the resulting stress vector, that is the Cauchy theorem. Equation (1.15) can be rewritten in the reference configuration with the referential stress vector

$$\boldsymbol{T} = \boldsymbol{P}\boldsymbol{N}, \tag{1.16}$$

with the referential normal vector $\boldsymbol{N}$ and the 1. Piola-Kirchhoff stress tensor $\boldsymbol{P}$, which is in general non-symmetric. Using equation (1.4), (1.15) and $\boldsymbol{T}d\boldsymbol{A} = \boldsymbol{t}d\boldsymbol{a}$, the 1. Piola-Kirchhoff stress tensor is

$$\boldsymbol{P} = J\boldsymbol{\sigma}\boldsymbol{F}^{-T}. \tag{1.17}$$

The 1. Piola-Kirchhoff stress tensor relates stresses in the actual configuration to areas in the reference configuration. Like the Cauchy stress tensor $\boldsymbol{\sigma}$, the components of the 1. Piola-Kirchhoff stress tensor vary when the body rotates without change in the stress state. For material formulations it would be preferable to have a tensor which is invariant

to rigid body rotations. The 2. Piola-Kirchhoff stress tensor possesses this property. The stress tensor relates stresses in the reference configuration to areas in the reference configuration. The 2. Piola-Kirchoff tensor can be derived from a pull-back operation of the Cauchy stresses $\boldsymbol{\sigma}$ weighted by the Jacobian J.

$$\boldsymbol{S} = J\boldsymbol{F}^{-1}\boldsymbol{\sigma}\boldsymbol{F}^{-T} \tag{1.18}$$

One possible way to describe the mechanical behavior of a body and to derive the stress tensor is to model it with a potential function, the strain-energy density function Ψ. In the context of thermodynamic the strain-energy density Ψ is called Helmholtz Free energy A. In case Ψ is a function of the right Cauchy-Green tensor $\boldsymbol{C}$, the 2. Piola-Kirchhoff stress tensor is

$$\boldsymbol{S} := 2\frac{\partial \Psi\left(\boldsymbol{C}\right)}{\partial \boldsymbol{C}}. \tag{1.19}$$

In order to get engineering stresses for analysis, the 2. Piola Kirchhoff stresses can be transformed by a pull forward operation ($\boldsymbol{\sigma} = J^{-1}\boldsymbol{F}\boldsymbol{S}\boldsymbol{F}$) to Cauchy stresses $\boldsymbol{\sigma}$.

For methods like the Finite Element Method, the elasticity tensor is important. This tensor can be obtained in a straightforward way as the second derivative of the Helmholtz Free energy Ψ with respect to the right Cauchy-Green tensor $\boldsymbol{C}$.

$$\mathbb{C} := 2\frac{\partial \boldsymbol{S}\left(\boldsymbol{C}\right)}{\partial \boldsymbol{C}} = 4\frac{\partial^2 \Psi\left(\boldsymbol{C}\right)}{\partial \boldsymbol{C}^2} \tag{1.20}$$

It shall be mentioned that the 81 (3^4) components of the elasticity tensor $\mathbb{C}$ are not independent due to symmetry properties. In general $\mathbb{C}$ possesses the so-called minor symmetries:

$$C_{ABCD} = C_{BACD} = C_{ABDC}. \tag{1.21}$$

The symmetry of the stress tensor (conservation of the angular momentum) and strain tensor (objectivity) makes it possible to reduce the elasticity tensor $\mathbb{C}$ to 36 independent components. This yields for

any material description of bodies. If a strain energy function Ψ is assumed, as proposed earlier, the elasticity tensor $\mathbb{C}$ holds also the major symmetries

$$\mathbb{C} = \mathbb{C}^T \text{ or } C_{ABCD} = C_{CDAB}. \tag{1.22}$$

The major symmetries allow further reduction of the elasticity tensor $\mathbb{C}$ to 21 independent components.

Governing equations The governing equation of a three-dimensional elastic continuum is given in its weak form in equation (1.23). The equation consists of inertia forces, the constitutive equation and body and boundary forces.

$$\int_\omega \rho \boldsymbol{a} : \delta \boldsymbol{u} \, d\omega + \int_\omega \boldsymbol{\sigma} : \delta \boldsymbol{e} \, d\omega = \int_\omega \hat{\boldsymbol{b}} \cdot \delta \boldsymbol{u} \, d\omega + \int_{\gamma_\sigma} \hat{\boldsymbol{t}} \cdot \delta \boldsymbol{u} \, d\gamma \tag{1.23}$$

The first term consists of the density ρ, the acceleration $\boldsymbol{a}$ and displacements $\boldsymbol{u}$. The second part describes the constitutive equations with the Cauchy stresses $\boldsymbol{\sigma}$ and the Euler-Almansi strains $\boldsymbol{e}$. The body and traction parts are described by body forces $\hat{\boldsymbol{b}}$ and traction forces $\hat{\boldsymbol{t}}$. Everything is denoted in the physical space with the domain ω and the boundary γ of the domain.

Of special interest for the later work is the constitutive part in equation (1.23). This part is currently denoted in the physical configuration. Earlier the concept of current configuration and reference configuration was introduced. Here the physical configuration can be interpreted as the current configuration.

The reference configuration can be interpreted as the material space from a Finite Element point of view and the constitutive term can be written in the following form

$$\int_\omega \boldsymbol{\sigma} : \delta \boldsymbol{e} \, d\omega = \frac{1}{2} \int_\Omega \boldsymbol{S} : \delta \boldsymbol{C} \, d\Omega \tag{1.24}$$

with the material domain Ω, the second Piola-Kirchhoff stress tensor $\boldsymbol{S}$ and the right Cauch-Green strain tensor $\boldsymbol{C}$.

1.3.2 Molecular mechanics

Even small molecular problems with as few as 100 atoms in three dimensions produce in every time-step 600 values for position and momentum. Taking into account that typical time-steps are in the range of femtoseconds, it becomes apparent that a huge amount of data has to be processed in a molecular dynamics simulation. One way to handle this problem is the introduction of phase-space trajectories, which shall be presented here in short. For a more detailed description of the subject the reader is referred to Haile [56].

Newtonian dynamics The spherical atom i is moved by an external force $\boldsymbol{F}_i$ in the Newtonian interpretation of dynamics. The motion and the applied force are related by Newton's second law,

$$\boldsymbol{F}_i = m\ddot{\boldsymbol{r}}_i \tag{1.25}$$

Here, m is the mass of the atom, which is assumed to be independent of time, position and velocity. The acceleration $\ddot{\boldsymbol{r}}_i$ is given by

$$\ddot{\boldsymbol{r}}_i = \frac{d^2\boldsymbol{r}_i}{dt^2} \tag{1.26}$$

where $\boldsymbol{r}_i$ is the location vector of an atom within a fixed set of coordinate axes and t is the time. For N spherical molecules, Newton's second law results in 3 N second-order, ordinary differential equations of motion.

If no force is acting on an atom equation (1.25) simplifies to $\dot{\boldsymbol{r}}_i = \text{const}$ which means that an atom initially at rest will stay at rest and an atom moving with a certain velocity will go on moving with that certain velocity. This is Newton's first law.

Assuming that a system of atoms is isolated and has no external forces acting on it, the sum of all forces must be zero,

$$\boldsymbol{F}_{total} = \sum \boldsymbol{F}_i = 0 \tag{1.27}$$

Looking at a system with only two atoms, the force exerted by the first to the second atom must balance the force exerted vice versa,

$$\boldsymbol{F}_1 = -\boldsymbol{F}_2 \tag{1.28}$$

This is Newton's third law. Taking all three laws of Newton, the kinetic energy E_k to move a spherical atom from rest to velocity $\dot{\boldsymbol{r}}$ can be derived as

$$E_k = \frac{1}{2} m \dot{\boldsymbol{r}}^2 \tag{1.29}$$

Hamiltonian dynamics Newton's second law (1.25) is invariant under time translations. For that reason we can expect that there is some function of the position and velocity of a set of atoms which is constant in time. This function is called the Hamiltonian $\mathscr{H}$.

$$\mathscr{H}\left(\boldsymbol{r}^N, \boldsymbol{p}^N\right) = \text{const} \tag{1.30}$$

with the momentum $\boldsymbol{p}_i$ of the atom i defined by

$$p_i = m \dot{\boldsymbol{r}}_i \tag{1.31}$$

Let's assume an isolated system, where the conserved quantity is the energy E, the combined potential and kinetic energy. Here the Hamiltonian $\mathscr{H}$ takes the form

$$\mathscr{H}\left(\boldsymbol{r}^N, \boldsymbol{p}^N\right) = \frac{1}{2m} \sum_i \boldsymbol{p}_i^2 + \mathscr{U}\left(\boldsymbol{r}^N\right) = E \tag{1.32}$$

with $\mathscr{U}$ the potential energy which results from intermolecular interactions.

The equations of motions for the Hamiltonian dynamics can be derived from equation (1.32) and are here given without any further derivation. For a detailed derivation the reader is referred to the book of Haile [56].

$$\frac{\partial \mathscr{H}}{\partial t} = \frac{\boldsymbol{p}_i}{m} = \dot{\boldsymbol{r}}_i \tag{1.33}$$

$$\frac{\partial \mathscr{H}}{\partial \boldsymbol{r}_i} = -\dot{\boldsymbol{p}}_i \tag{1.34}$$

Using the equations of motion of the Hamiltonian dynamics and comparing it to Newton's law (1.25) yields

$$\boldsymbol{F}_i = -\frac{\partial \mathscr{H}}{\partial \boldsymbol{r}_i} = -\frac{\partial \mathscr{U}}{\partial \boldsymbol{r}_i} \tag{1.35}$$

Expression (1.35) is equivalent to the definition of a conservative force, which can be written as the negative gradient of some potential $\mathscr{U}$.

The difference between the Newtonian dynamics and Hamiltonian dynamics can be recognized in the above derivation. The Newtonian dynamics is driven by an external force to which the system is answering, while in case of the Hamiltonian mechanics, there is no force given explicitly. The system moves in order to satisfy the Hamiltonian $\mathscr{H}$.

Potential energy functions In order to compute the intermolecular forces $\boldsymbol{F}_i$ an appropriate potential function $\mathscr{U}$ is necessary. For a system with N atoms, the interactions can be described by pairwise interactions

$$\mathscr{U}\left(\boldsymbol{r}^N\right) = \sum_{i<j}\sum u(r_{ij}) \tag{1.36}$$

It should be noted that this description of the interactions neglects multibody interactions, which would substantially increase computational time. For some atoms or molecules it might not be justifiable to describe interactions by a two-body potential.

The potentials to describe the interaction between atoms can be grouped into bonded interactions u_{bonded} and non-bonded interactions $u_{\text{non-bonded}}$. The non-bonded interactions include the van-der-Waals potential u_{vdW} and the Coulomb potential u_{elec} while the bonded interactions are commonly described by out of equilibrium distances and angles within a molecule.

Bonded interactions Bonded interactions are described by changes of the equilibrium position of the atoms to each other. Molecules with covalent bonds generally prefer a position to each other, where the potential energy is minimal. Every move out of this position changes the potential energy of the molecule. Any positional changes of atoms, connected to covalent bonds, are combined and called bonded interactions.

$$
\begin{aligned}
u_{\text{bonded}} &= k_b(b-b_0)^2 + k_\theta(\theta-\theta_0)^2 + \\
&\quad k_\phi[1+\cos(n\phi-\delta)] + k_\omega(\omega-\omega_0)^2 + \\
&\quad k_{UB}(b^{UB}-b_0^{UB})^2
\end{aligned} \tag{1.37}
$$

The bonded interactions and their description is taken as defined in CHARMM [19] and the CHARMM force field [89]. Here, the first term describes the bond stretches between neighbouring covalent bound atoms. The parameter k_b is the force constant and $b - b_0$ is the distance the atoms have moved out of their relative equilibrium positions. The second term is responsible for bond angles with k_θ the angle force constant and $\theta - \theta_0$ the difference angle from equilibrium between three bonded atoms. The third term accounts for dihedrals interactions (torsion angles) where k_ϕ is the dihedral force constant, n is the multiplicity of the function, ϕ is the dihedral angle, and δ is the phase shift. The fourth term describes the improper interactions or the out of plane bending interactions. Their force constant is k_ω and $\omega - \omega_0$ is the out of plane angle. The last term describes the Urey-Bradley component, a cross-term component accounting for angle bending using 1,3 non-bonded interactions. Here, k_{UB} is the force constant and $b^{UB} - b_0^{UB}$ the distance from the current position to the equilibrium position.

Non-bonded interactions Non-bonded interactions are described by van-der-Waals and Coulomb interactions.

The most common potential model for non-bonded van-der-Waals interactions was introduced by J. E. Lennard-Jones in 1924 for a soft-sphere pair potential [74].

$$
u(r)_{\text{vdW}} = 4\epsilon\left[\left(\frac{\sigma}{r}\right)^{12} - \left(\frac{\sigma}{r}\right)^{6}\right] \tag{1.38}
$$

The necessary parameters to compute the potential $u(r)$ in equation (1.38) are σ, the distance of the atoms, where the potential energy $u(r)$ is zero, and ϵ, the depth of the potential well.

The Lennard-Jones potential attempts to model the short-range repulsive force as well as the long-range attractive forces. By convention,

repulsive forces are defined as positive while attractive forces are defined as negative.

As a side-note, the reader might find it interesting that the potential proposed by Lennard-Jones is not per se defined with the exponents 6 and 12, but with the parameters n and m. The exponent m can be hereby physically motivated by London's theory [88] for dispersion as $m = 6$. The second exponent was then set as $n = 2m = 12$ which makes sense as Lennard-Jones defined $n > m$, but has no further physical justification. Choosing the exponents as just explained results in the Lennard-Jones (12,6) potential in equation (1.38), which is commonly used for two-body interactions.

The electrostatic interactions are modeled by a Coulomb law with q the respective charges, ϵ the effective dielectric constant and r the distance between the two atoms.

$$u(r)_{\text{elec}} = \frac{q_i q_j}{\epsilon r} \tag{1.39}$$

Phase-space trajectories The aim of molecular mechanics simulations is to create molecular trajectories over a finite time. Instead of using only the positions of the spherical atoms it is possible to extent the idea to additionally store the momentum of each atom. Consider a system with N atoms which is isolated to its surrounding. The position of each atom is described by its position vector $\boldsymbol{r}_i$. The atoms are moving according to Newton's law governed by interaction potentials. The resulting trajectories are time-dependent position vectors $\boldsymbol{r}_i(t)$. As the atoms move along their trajectory, their momenta are changing as well. As a result, each atom has time-dependent momentum vectors $\boldsymbol{p}_i(t)$.

If the position and moment vectors are plotted at a certain configuration at time t, the plot will be a 6N-dimensional hyper-space. Such a space is called phase-space. It consists of a $3N$-dimensional configuration space, representing the position of each atom, and the $3N$-dimensional momentum space, in which the coordinate axes are the components of the momentum vector $\boldsymbol{p}_i(t)$. At a certain configuration, the complete isolated system is represented by one point in the phase-state space. Moving on in time, the point moves and gener-

ates a trajectory. The first objective of molecular dynamics simulations is to produce such phase-state trajectories over a finite time. This is achieved by solving either Newton's second law (1.25) or, equivalently, Hamilton's equations (1.33) and (1.34) numerically.

1.4 Objective and outline of the thesis

As explained earlier, lung inflammation can start due to mechanical ventilation, though the exact mechanism is not yet understood. In order to evaluate different theories, it would be beneficial to know more about the actual mechanical stimuli a cell is exposed to during ventilation. The magnitude and nature of these forces and deformations can provide more insight into possible signaling pathways. This aspect, what kind of strains and forces are acting on alveolar cells during mechanical ventilation, has currently not been very well investigated. To describe this aspect, the term "mechanobiological environment" (MBE) is used. The MBE is the mechanical environment that contributes to mechanotransduction. The investigation of the MBE of alveolar pneumocytes shall be the focus of the thesis at hand.

For the investigation a mixture between experimental and modeling approaches is chosen to improve the understanding of biomechanical events in alveoli. Experimental difficulties to investigate strains and stresses on a cellular level *in vivo* or even *in vitro* makes the *in silico* approach very promising. However the *in silico* approach alone is not sufficient. Only in combination with experimental work and validation of the developed models, the MBE of alveolar cells can be investigated.

The transfer of mechanical stimuli originating from the mechanical ventilation machine to the alveolar scale is a multi-scale problem. Within the MBE at least two scales are present, the continuum scale covering cells and tissues, and the atomistic scale, important for integrins. Several experimental and theoretical techniques have been employed to investigate the MBE of alveolar pneumocytes. The core of the investigation is on a mechanical description of the MBE with models for the most important constituents. Figure 1.1 shows schematically the modeling process. The two main components, tissue and cells, are described by continuum-based material descriptions. For both compon-

ents it is necessary to formulate stable and biologically interpretable mechanical descriptions. With a continuum-based material model it is only a small step to create a Finite Element computational framework. With help of Finite Element simulations the computed stresses and strains can be used as a basis for interpreting mechanical signaling pathways. Since the strain transfer from the Extra-cellular Matrix (ECM) to the cell is important for the MBE, it is necessary to model the connections between cell and ECM, i.e., the focal adhesions. In order to be as accurate as possible, focal adhesions are modeled by an approach where the mechanical model is enriched by molecular dynamics (MD) simulations. This approach allows an improved mechanical description of integrins. Besides modeling the cell, tissue, and interface, boundary conditions are also important. Especially the applied strain is of importance as it is the up-scale source for all following stimuli. Here, experimental work accompanies the modeling process. Neutron Computed Tomography (NCT), a new method for biomechanics, was tested to see if it is suitable to image the lung and its structure. Additionally, conventional confocal microscopy was combined with a stretching device to image local strains in alveoli.

The structure of the thesis follows the modeling approach of Figure 1.1, investigating mechanical environment of alveolar pneumocytes. The following topics are presented in Chapters 2 to 4.

In search of a method to image alveoli, Neutron Computed Tomography (NCT) was tested. Although NCT is currently not able to resolve alveoli, the characteristics of neutrons, to discriminate clearly between air and water, showed very beneficiary results. Applying NCT to rat lungs, lung structures with a spatial resolution of up to 50 μm could be resolved. The three-dimensional image stacks enable to follow the alveolar tree from the trachea consistently to the 6^{th} generation, in some cases even to the 10^{th} generation. This new technique for lung imaging is presented in Chapter 2.1.

Chapter 2.2 investigates alveolar strains with the help of uni-axial tension and two-photon microscopy. Living tissue strips were mounted on the machine and stretched in discrete steps. At every step, the tension force was recorded and a three dimensional stack of the same alveoli was imaged. Using the image data, local strains on the alveolar

level can be connected with the global strain, applied by the machine.

The modeling of the cell is described in Chapter 3. The different mechanical components of the cell are described with strain energy density functions and are additively combined for an overall cell model. The important characteristics of convexity and stress-free reference configuration are discussed. The cell model is extended with a term describing the contraction of cells. Parameter identification for the contraction model is also discussed.

The mechanical stimuli, i.e. strains, are transferred from the tissue to the cell through focal adhesions. Focal adhesions themselves consist of integrins, which are transmembrane proteins with a long extracellular and a short intracellular tail. The mechanical behavior of the integrin-ECM interaction is important for investigating the strain transfer from ECM to cells. To describe the mechanical behavior of the integrin-ECM connection, a Finite Element material model was enhanced with molecular dynamics simulations. Details can be found in Chapter 4. As a result, the material properties of the $\alpha_2\beta_1$ I domain bound to tropocollagen were computed. Besides the mechanical description, another benefit of the proposed method is that the molecular scale is fully resolved and the reaction of single bonds to the mechanical stimuli can be studied in detail.

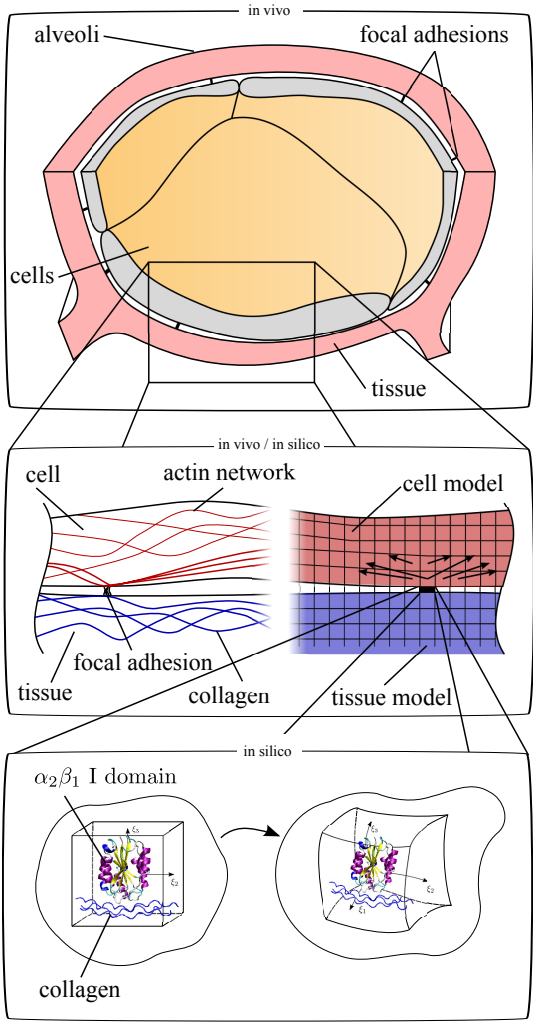

Figure 1.1: Modeling the mechanobiological environment: Tissue and cells are modeled by Finite Elements (FE) and appropriate material descriptions. Focal adhesions are modeled by a coupling approach between FE and molecular dynamics.

Chapter 2

Experimental investigations and observations

Two experimental techniques were used to investigate alveolar mechanics. The first technique, Neutron Computed Tomography (NCT), is new to biomechanics and was previously applied to classical engineering problems. It uses neutrons to image an object in three dimensions like conventional tomography. Though current image resolutions of NCT are only close to the size of alveoli, the unique properties of neutrons to detect water made it interesting to test the method for a biological object, especially the lung.

The second method is confocal microscopy. The microscope was combined with a uniaxial tension machine to stretch tissue and simultaneously record images of alveoli.

2.1 Lung imaging by Neutron Computed Tomography

Standard clinical imaging methods like Magnetic Resonance Imaging (MRI), Computed Tomography (CT), Positron Emission Tomography (PET) and Single Photon Emission Computed Tomography (SPECT) can image airways in vivo, but only with limited resolution. In humans, the spatial resolution of CT is typically in the range of up to the 5th or 6th airway generation and up to the 3rd airway generation for MRI. Research methods such as μCT [87, 114], two photon microscopy [112, 108], Optical Coherence Tomography [95] and microscopy on the open chest [24, 135] provide better temporal and spatial resolution, but are generally applied ex vivo. In addition, for lung stabilization and improved imaging quality, these methods usually require some degree of lung preparation (e.g. fixation, injection of liquid or a contrast substance). Recently the use of gadolinium or hyperpolarized gas with MRI shows promising results to further enhance the resolution [149, 27]. With the latter method, lung structures of $70\mu m$ could be resolved.

In the following, we present a new technique for imaging central airways, which employs neutrons [97]. It takes advantage of the characteristic of neutrons to not interact with the atom shell, but with the nucleus itself. Neutrons are thus either absorbed or scattered by the target nuclei. Since protons (i.e., the hydrogen nuclei) have about the same mass as neutrons, they have a very high scattering cross-section for neutrons, resulting in strong attenuation even for small amounts of hydrogen. This characteristic of neutrons provides good contrast between intrapulmonary air and lung tissue (which consists of hydrocarbons). Special preparation of biological samples is thus no longer required for imaging. The high hydrogen attenuation (and thus the high sensitivity) limits the applicability of the technique to the presence of a small amount of hydrogen in the sample. This, however, is not a problem when it comes to lungs, because they mostly consist of air, with only thin layers of tissue surrounding airways and alveoli. While X-rays fail to pick up the small amount of tissue of smaller lung structures, the hydrogen content in the lungs delivers sufficient contrast for neutrons to reconstruct a computed tomography.

2.1.1 Experimental setup and lung preparation

At the Neutron Computed Tomography (NCT) facility for neutron imaging, ANTARES [120], at the FRM II reactor of Technische Universität München, neutrons enter through a small pinhole (typically 20 mm diameter) into a 16-meter-long evacuated flight tube, delivering a quasi-parallel beam without intrinsic image magnification. After penetrating the sample, neutrons are detected by a nuclear reaction (^{6}Li(n,α)^{3}H) in a ZnS(Ag,Cu) scintillation screen. As this reaction is highly exothermic (kinetic energy products 4.7 MeV), it has to be stopped in the scintillation material within a certain distance. Resolution is thus limited to about 100 micron on a standard screen and to about 30 micron on specially-thinned screens. For CT, the biological sample is rotated in front of the screen. The resulting image is recorded with a high-resolution, cooled CCD camera (Andor DW436, 2024x2024 pixel, 16bit).

The animal experiments were conducted under the animal protection law of the state of Bavaria, Germany. The rats were anaesthetized with $2-3$ vol% isoflurane and subsequently killed by exsanguination. The thorax was opened and the lung, heart, thymus and esophagus were excised en bloc. After separating the lung from the adjacent organs, a cannula was inserted into the trachea. A total of six lungs were excised from Wistar rats (Charles River Laboratories, Schweinfurt, Germany). Following excision, each lung was placed immediately into an aluminum tube with an inner diameter of 25 mm (Figure 2.1). This tube was used to simulate the confinement of the rib cage. Aluminum was chosen because it is highly transparent for neutron beams. The lung was supported additionally from the bottom by an adjustable plate. The aluminum tube was placed on a turntable within the neutron beam as described earlier. The lung was inflated with normal air and the inflation pressure was kept between 20 and 30 cmH_2O. The inflation pressure kept the lung in place and provided stable conditions during the subsequent imaging process. The surrounding cylinder was cooled to 4-5 degrees Celsius by a peltier cooler to slow down decay of the lung tissue. The cylinder was introduced into the NCT-system in the upright position and rotated by 180° (which is sufficient in the case of parallel beam geometry) over a period of 140 minutes.

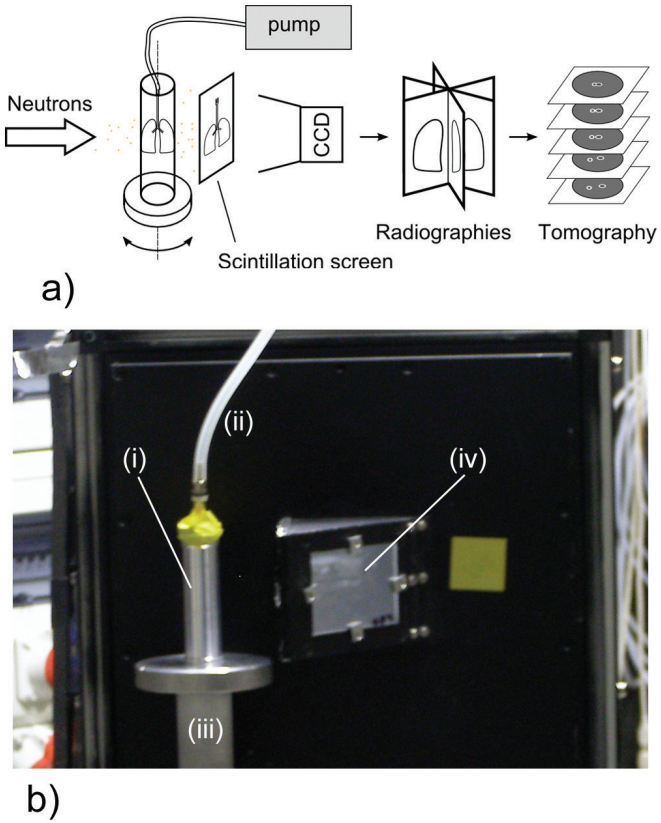

Figure 2.1: (a) Schematic setup of the experiment where neutrons penetrating the lung embedded in an aluminum tube from the left, getting scattered, with the remaining neutrons interacting with the scintillation screen. Images are recorded by a CCD camera and computed to a 3-dimensional stack. (b) Experimental setup with the aluminum tube (i) placed on a turntable (iii) and the tube (ii). Opposite the incoming neutrons is the scintillation screen (not visible), whose emitted light is diverted by a mirror (iv) to the CCD camera, which is placed behind the black board.

2.1.2 Lung images

The characteristic behavior of neutrons results in good contrast between intrapulmonary air and lung tissue (which consists of hydrocarbons). It makes special preparation of the organ for imaging unnecessary. The high hydrogen attenuation is an advantage when it comes to the lung because it mostly consists of air with only thin layers of tissue.

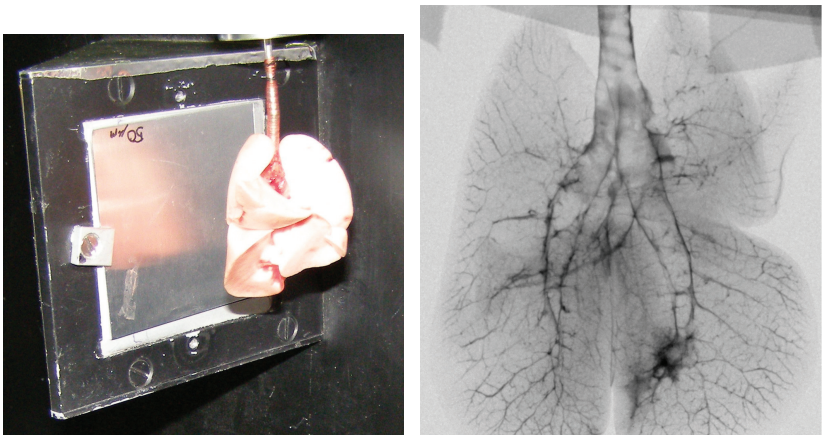

(a) Lung suspended in front of screen (b) Radiograph of freely suspended lung

Figure 2.2: Radiograph (b) of an unconfined rat lung suspended in front of the scintillation screen (a).

Using the NCT system, the trachea with the attached cannula and the first bifurcations of the lower airways are clearly visible (Figure 2.2b and 2.3). As neutron imaging and the corresponding detection system uses mostly positive images (i.e., showing intensity, not attenuation), dark spots reflect greater attenuation. The dark linings represent the walls of the trachea and the first bifurcation is clearly visible. Smaller airways cannot be identified this way, because of the limited contrast and spatial resolution of a single radiograph. However, branching of the airways can be followed to the very periphery of the lung. The resolution of these radiographies is in the range of $50-60\ \mu m$. This makes

neutron tomography highly suitable when the area of interest is large and must be measured with high accuracy. The faint vertical lines on the outer left and right hand sides and the grey area at the bottom of each image indicate the aluminum cylinder. Some water content lining the aluminum tube can be observed in Figure 2.3 (left on the bottom), and in Figure 2.4 (left at the lower right part and upper left part). These are water drops that occur sometimes due to condensation but do not represent any lung structures.

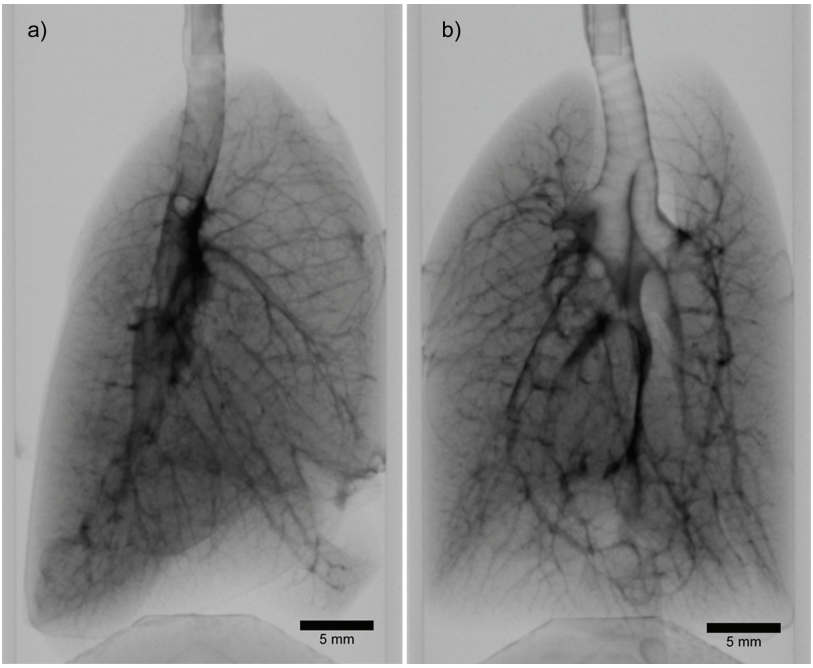

Figure 2.3: Lateral (a) and frontal (b) radiographs of a rat lung. The dark structures represent hydrogen-containing tissue and the lighter structures represent air-containing airways. The fine lines on the outer left and right hand sides and the gray area at the bottom of each image reflect the aluminum cylinder. At the top, the cannula introduced into the trachea can be observed.

The outer boundaries of the lung can be observed in Figure 2.3. In the upper part the lung is free while in the middle and the bottom it is pressed against the aluminum cylinder. The same can be observed as well in the cross-sectional slices of Figure 2.5. Here, both pulmonary lobes enclosing air space can be seen at the top right image above the center. The enclosed airspace is reduced but still existent in the lower cross-sectional image below. There is additional water content in between the pulmonary lobes (fissura obliqua / horizontalis), which allows the identification of the different lobes.

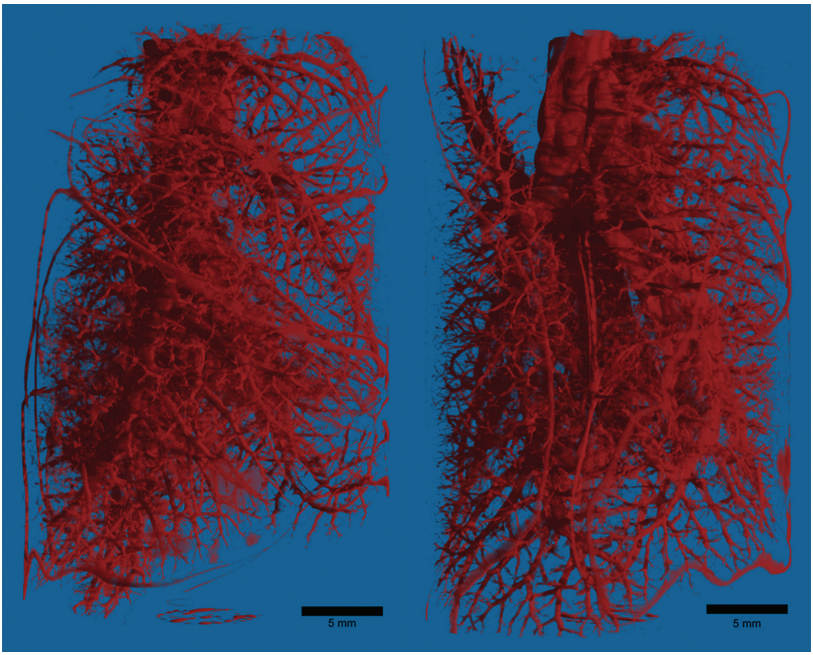

Figure 2.4: Lateral (left) and frontal (right) computed tomograms of a confined lung. Red structures reflect hydrogen-containing components of the lung, i.e. lung tissue.

Following removal of the inflated lung from the container and further inflation to more than twice its previous volume, lung structure

could be far better identified than in the confined state (Figure 2.3).

The ray-traced segmentation of the 3-dimensional volumetric data provided high quality computed tomograms, which allow identification of small airways in the very periphery of the lung and geometric reconstruction of several generations of the airway tree (Figures 2.4 and 2.5). The bifurcations of the airways can be traced down to the $6^{th} - 10^{th}$ generation, with airway walls clearly visible (Figure 2.5). The fluid content of blood vessels attached to airways causes the seemingly thicker airway walls at some locations. The inner diameter of the airways can easily be identified, which is important for successful segmentation of the images.

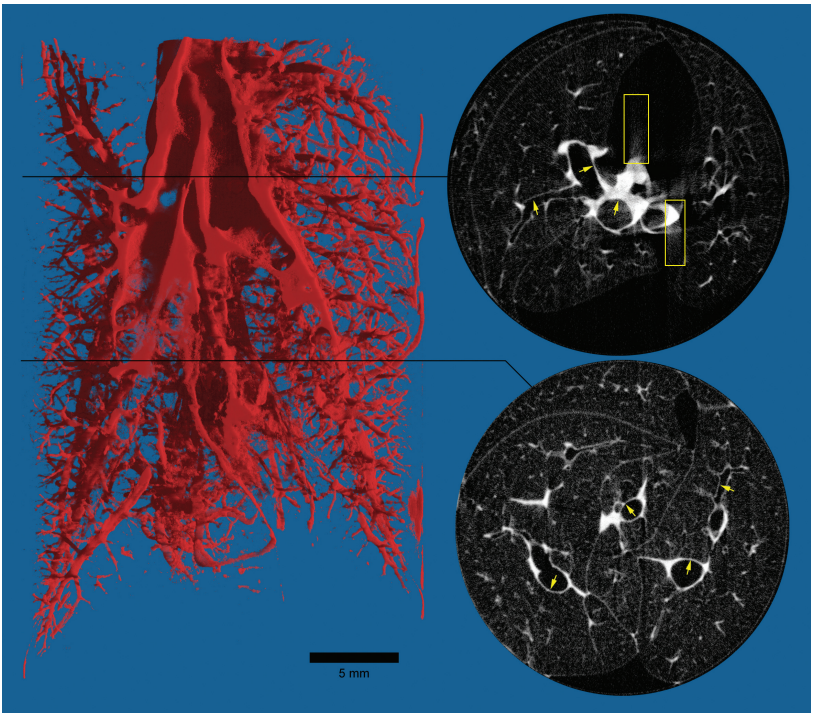

Figure 2.5: Frontal view of a cut 3-dimensional computed tomogram of a confined rat lung (left) and two tomogram slices (right) at the indicated levels (black lines). The airway walls can be clearly identified (arrows) and airways can be traced down from the trachea to the periphery. Small motion artifacts are present in areas with very high hydrogen content and where tissue cannot be properly stabilized (indicated by rectangles).

2.1.3 Possibilities and limitations of NCT

The main finding of our investigation is that NCT provides high-resolution lung imaging without the need of additional organ preparation. This high-resolution imaging is caused by the interaction of neutrons with the nucleus rather than the electron shell. It results in excellent detection of biological structures with high water content, such as in soft tissues of airways, lung parenchyma, and vasculature. The high quality of the 2-dimensional radiographs does not only allow identification of larger structures of the lower airways and the carina, but also allows discriminating between soft tissue and cartilage of the trachea.

Due to the 3-dimensional nature of the lung, two-dimensional images do not allow identification of very distal airways. However, 3-dimensional reconstruction enabled visualization of very distal and small lung structures and allowed an excellent insight into the complicated 3-dimensional organization of airways. Especially, the clear contrast between airway walls and the lumen makes it possible to identify the inner diameter of airways for several generations (yellow arrows, Figure 2.5). The current spatial resolution of NCT is approximately 50-60 μm. This allowed reliable measurements of the inner diameter of airways down to the 6^{th} generation. In some cases it was even possible to follow the airway tree down to the 10^{th} generation. This makes NCT a suitable technique for computational reconstruction of the airway tree. The limiting factor for even better spatial resolution is not the method itself but the thickness of the neutron detection screen placed behind the lung. Ongoing development of thinner neutron detectors will further improve resolution and image quality.

Blood vessels (wall and lumen) and airway walls contain comparable amounts of water. Since NCT detects small amounts of water, blood vessels attached to airways are imaged the same way as walls of airways. This will make reliable differentiation between airway walls and attached blood vessels difficult. The high water content of blood vessels may be causing artifacts due to small movements of the probe during scanning (Figure 2.5, upper right tomogram). Similarly, as blood vessel lumen and wall contain comparably high water content, reliable differentiation between both is not possible.

The newly developed lung chamber was able to stabilize the lung during the entire measurement period of 3-4 hours. Motion artifacts due to occasional twisting of the intratracheally placed cannula may occur at the top of the trachea and the carina (Figure 2.5, yellow rectangles). The lung chamber offers the possibility of either increasing intrapulmonary pressure above atmospheric pressure to simulate positive pressure of mechanical ventilation, or reducing extrapulmonary pressure below atmospheric pressure to simulate spontaneous breathing, and to generate a transpulmonary pressure gradient.

Although NCT is not suited for *in-vivo* imaging, its high quality imaging makes it highly attractive for basic research in pulmonary physiology and pathophysiology. Structural analysis of large and small airways with high resolution can be performed in excised healthy and experimentally damaged lungs under a variety of experimentally set transpulmonary pressures. In the past years, the pulmonary stress-strain relationship came into the focus of scientific interest in the field of lung-protective ventilation [29]. Analyzing lungs under different transpulmonary pressures by NCT would enable accurate analysis of longitudinal and transversal strains in the airways. It may also help in investigating and understanding of cellular processes in airways [142] and of dynamic lung processes (e.g., small airway recruitment and de-recruitment [4, 131]). The ability of NCT to detect small amounts of liquids makes it likewise suitable to study clinical problems such as e.g. the formation and propagation of pulmonary edema.

Finally, NCT may generate data that can be used for the development of a computational lung model. Additional information provided from simulation data [146, 150] is of special interest in the area of research of lung physiology and pathophysiology because spatial and temporal limitations of most experimental methods make monitoring of small airways and alveoli under physiological conditions difficult, if not impossible.

In summary, our findings confirm our hypothesis that NCT provides high quality lung imaging. Although NCT of biological samples is still in its infant state, the ability to reliably image lung structures down

to the 6^{th} airway generation, in some cases even down to the 10^{th} generation, makes this technique a highly attractive research tool. It may improve understanding of basic pulmonary physiology and pathophysiology, which may ultimately lead to improved patient outcome.

2.2 Alveolar strains

The measurement of alveolar strains is important for reviewing possible signaling pathways in the lung. Depending on the intensity, straining alveolar tissue can lead to different inflammatory response in the lung.

First, large strains result in disruption of the cellular plasma membrane [53] followed by necrosis, which leads to the release of inflammatory mediators [143]. Such mediators stimulate nearby cells to produce more inflammatory mediators which leads ultimately to an inflammation. Second, small strains, which cause no disruption of cell membranes, might start other signaling pathways by transferring the external stimulus into cells via integrins.

The exact measurement of alveolar strains is difficult due to the nature of the parenchym. The complicated three-dimensional morphology and the high ratio of air to tissue makes it difficult to image alveoli. Currently, several optical methods are used to image and measure the deformation of alveoli: imaging through a thorax window with Optical Coherence Tomography (OCT) [95], intravital microscopy [96] or video microscopy [46]. Excised lungs can also be measured by OCT [94, 93]. By inflating the lung and imaging subpleural alveoli from the top (microscopy) or in three dimensions (OCT), it is possible to measure the expansion of single alveoli. But in general the resolution is insufficient to measure strains of alveolar walls. This is especially true for microscopic methods which look only on top of alveoli with the pleura visceralis covering them. A method with higher resolution is confocal laser scanning microscopy [108] or fluorescence microscopy [18]. Using these techniques, the resolution is typically in the range of 0.2 - 0.4 μm per pixel and is high enough to look at single alveolar walls, which are in the range of 6 - 8 μm. Indirect measurements of strains on the alveolar level have been conducted by measuring the surface area [47] occupied by alveoli, slicing parenchym [76], anatomical analysis [76], and diffuse light scattering [21]. Using a special constructed bioreactor to stretch the alveolar tissue might yield another possibility to measure alveolar strains [123]. Only recently, local strains of alveolar structures were investigated by Rausch et al. [110] using synchrotron-based X-ray tomographic microscopy in combination with a FE model and a non-

linear material description of alveolar walls [111].

In particular confocal microscopy, as introduced in the previous paragraph, is interesting as it provides the possibility to resolve alveolar walls and to image alveoli in three dimensions. Perlman et al. [108] measured the change in alveolar wall length for the first time by confocal microscopy. By increasing the intrapulmonary pressure up to 20 $cm\ H_2O$, they were able to measure the length increase of alveolar walls. Due to the experimental protocol, only subpleural alveoli were accessible. They found that the alveolar wall length increased from 0% up to 30% with a peak of the length distribution at around 20% of baseline length. Baseline length is hereby defined as the average length before inflation. As they used internal pressure to stretch the lung, they were able to measure the change in baseline length for inflation as well as deflation. They found a hysteresis behavior for the pressure to baseline length relation. Their exact measurement of alveolar walls also revealed the heterogenous nature of the parenchym.

Brewer et al. [18] came to the same conclusion regarding the heterogeneity. The main subject was the mechanical properties of lung tissue due to emphysema. By staining type I collagen in alveolar walls, they were able to image alveoli and their deformation in two dimensions. This results in an average elongation of alveolar walls of around 18% at a macroscopic strains of 30%. Macroscopic strains are hereby defined as the strains applied by the stretching device to the tissue strips.

Similar findings were reported by Mertens et al. [96] using darkfield intravital microscopy. In this study, the intrapulmonary pressure was increased from 0 to 24 $cm\ H_2O$, and the change in area of the subpleural alveoli was measured. They found an increase of up to 40% for the highest pressure.

Previously given experimental methods show either high resolution in two dimensions, or low resolution within a three dimensional approach. Due to the three dimensional nature of the parenchym and the small scale of alveolar walls, it would be preferable to fulfil both criteria, resolution and imaging in three dimensions.

In the present work an approach was adopted to use two photon microscopy together with an uniaxial tension machine in order to stretch tissue strips and simultaneously image one particular alveoli. The mi-

croscopic images provide sufficiently high resolution to resolve alveolar walls and, by following particular alveoli, the deformation can be analyzed in three dimensions. The image stacks are then used to measure the length change between particular points within alveolar walls as a measure for alveolar stretching.

2.2.1 Tissue preparation and experimental setup

To measure the stretch of alveolar tissue using two photon microscopy, the tissue needs to be prepared prior to mounting it onto the uniaxial tension machine. The stretching is achieved by fixating the tissue with two grips and is monitored in the area of interest by the microscope.

Tissue preparation Agarose-filled lung tissue of rat lungs is sliced in round tissue slices with a diameter of 10-15 mm and thickness of around 400 - 500 μm. The detailed protocol is given by Martin et al. [91]. The tissue samples are then cut into strips with a width of 7 mm. After incubating the strips overnight to dissolve the low-temperature agarose, the slices were collected for experiments. One slice per well was placed on a 24-well plate. Every well was covered with 500 μl incubation medium. To later visualize intracellular calcium (Ca^{2+}), the slices were loaded for 2 hours at 37° C with Oregon green (5 μM), 0.2% pluronic (Pluronic-F127; 5 μM) and sulfobromophthalein (100 μM).

Stretch measurement After successful incubation, tissue strips are mounted between two custom made grips, connected to a Bose ElectroForce 3100 (Bose Corporation, ElectroForce Systems Group, Eden Prairie, Minnesota, USA) uniaxial tension machine equipped with a 0.5 N load cell. The Bose machine is placed on a microscopic stage. Samples are excited at 750 nm with a Ti:Sa femtosecond laser (Maitai HP, Spectra Physics). The laser beam scanned an object field with 400 $\times$ 400 μm (Trim Scope, LaVision BioTec, Bielefeld, Germany), and light was detected by ultrasensitive PMTs ($d = 25\ mm$). Figure 2.6a shows the experimental setup with a magnified photo of the mounted tissue in the lower left corner. Figure 2.6b shows the schematic setup of the experiment. Due to limited space beneath the microscope, the tissue strip cannot be placed directly under the optical system using the original connectors for the clamps. Therefore, a special mount was constructed which moves the clamps towards the back of the microscope and down towards the microscope table. The additional construction is made of acrylic glass which is stiff enough to avoid influence on the measurement because of the low forces involved and the static measurement.

The table, where the tension machine is mounted, controls the global $\boldsymbol{X}$- and $\boldsymbol{Y}$-direction, while the objective of the microscope points in $\boldsymbol{Z}$-direction. Values for the $\boldsymbol{Z}$-direction can be directly taken from the microscope, while for the $\boldsymbol{X}$- and $\boldsymbol{Y}$-direction μm-measurement tools are installed. The tissue is stretched in $\boldsymbol{x}$-direction, and displacement of the right clamp is measured by the tension machine directly.

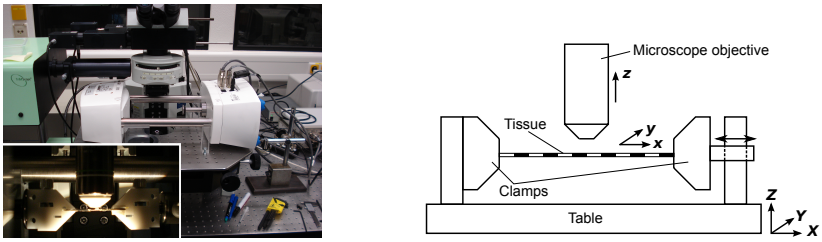

(a) Experimental setup (b) Schematic setup with coordinate systems

Figure 2.6: (a) Experimental setup with the uniaxial tension machine mounted on the microscope stage. (b) Setup of stretch measurement with microscope and tension machine.

The measurement starts after the tissue is mounted and the position of the imaging area in the coordinate system $\boldsymbol{XYZ}$ is recorded. The imaging area covers at least one alveoli, which is followed during stretching. The tissue is pre-stretched to a pre-force of 2 mN. The distance between the two clamps before pre-stretching was $l_0 = 2\ mm$. After pre-stretching, the first three-dimensional stack and the force is recorded. The tissue is stretched in 5%- or 7%-steps and the force is recorded immediately after the specified displacement is achieved. While stretching, the global coordinates $\boldsymbol{X}$, $\boldsymbol{Y}$ (controlled directly at the microscope table) and the $\boldsymbol{Z}$-direction (adjusted by the microscope) are controlled so that the imaging area stays constantly within the actual captured image. This ensures that the same area is always imaged for different global stretches. These steps are repeated for every global stretch. In general, 10 stacks with the dimension of 400 $\times$ 400 μm and 120 μm tissue penetration were recorded at 10 different global stretches.

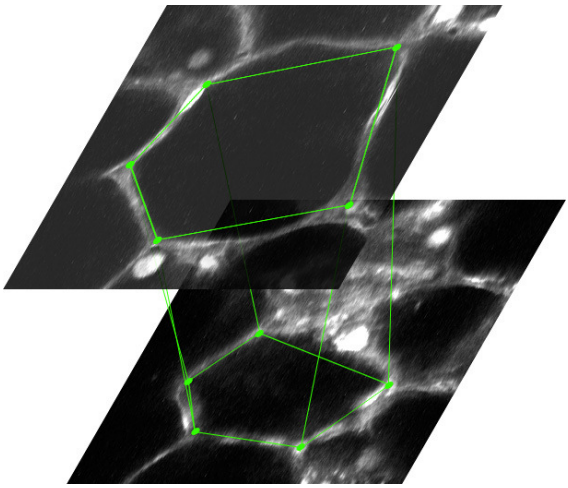

Figure 2.7: Measurement of stretches from three dimensional image stacks of alveoli.

Image analysis All images were analyzed using ImageJ [1]. Three dimensional renderings of alveoli were made with the help of Image-Pro Analyzer 3D (Media Cybernetics Inc., Bethesda, MD, USA). The three dimensional stacks follow one particular alveoli over different global stretches. In order to analyze the local stretch of single alveolar walls, the movement of particular points, namely crossings of alveolar walls, was measured on all images. This measurement was conducted for two different planes of the same alveoli. By computing the length between these points, an internal skeleton (Figure 2.7) inside the alveoli is created. The deformation of this skeleton is nearly equal to tissue stretches within one plane and represents the alveolar deformation for cross-plane connections. In general, the stretch λ was measured in the following form

$$\lambda = \frac{l}{l_{pre}} \tag{2.1}$$

with l being the actual measured length and l_{pre} being the length of the tissue strip after pre-stretching.

All stretches were averaged to compute one median stretch for every global stretch. In order to investigate the forces within the tissue, the stacks were cut perpendicular to the $\boldsymbol{X}$-direction to measure the area of the tissue in this plane. The median of all areas was used as a representative area to compute the first Piola-Kirchoff stress $\boldsymbol{P}$.

2.2.2 Stretch and stress results

The results gained from image analysis are organized in three main sections. The first section presents general observations and results of the analysis, as e.g. the position of the measured stacks within the tissue strip and results of the thickness measurement of the strips. The second section deals with the calculated stretches of alveolar walls. The third section looks into forces and stresses of the tissue.

General results and observations

In the following section, a distinction between global and local stretches is made. Global stretches are defined as those applied by the uniaxial tension machine. Local stretches represent the elongation of alveolar walls.

Imaging position As the position of the imaging area was recorded in the global coordinate system $\boldsymbol{XYZ}$, the position of the image stacks on the lung tissue strips can be recovered. Figure 2.8a shows the position of all measurements before stretching. The $\boldsymbol{y}$-axis represents the width of the tissue, while the $\boldsymbol{x}$-axis represents the length of the strip between the two clamps. The distance between the two clamps was $l_0 = 2\ mm$ when the tissue was mounted. The tissue was pre-stretched after mounting until a pre-stress of $F = 2\ mN$ was reached. The median and standard deviation of all lengths after pre-stretching was $l_{pre} = 2.93 \pm 0.26\ mm$. In general, it was attempted to place the imaging area in the middle of the strip. But the three-dimensional form of the imaged alveoli and the visibility of tissue were given priority over position. Therefore, imaging areas are not always centered as it can be seen in Figure 2.8a.

Comparison between global and local movement Tracking the movement in $\boldsymbol{X}$-direction of the table allows the comparison of these results with the $\boldsymbol{x}$-translation of the tension machine. For a more detailed explanation, let's assume we have a perfect system with the imaging area directly in the middle of the tissue strip. In this case, the

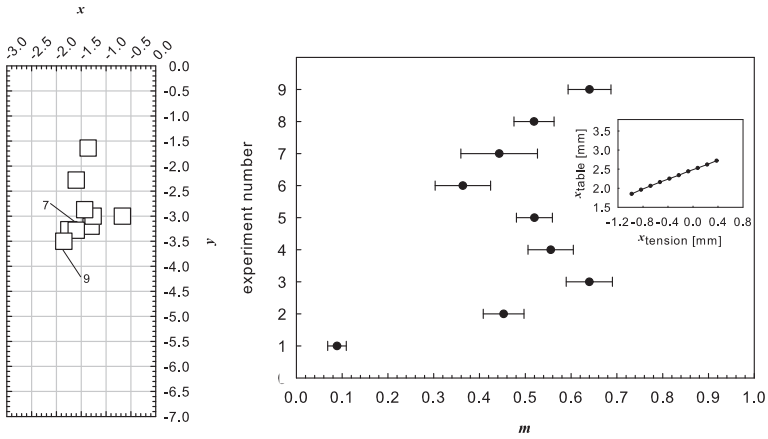

(a) (b)

Figure 2.8: (a) Area of measurement on the lung tissue strip. Every box represents one 400 μm × 400 μm image. (b) Comparison between machine and table movement. Small graph shows results for experiment number 9 (position marked in (a)).

table has to be moved half the distance in the opposite direction of the moving clamp to keep looking at the same imaging area through the microscope. This is due to the fact that only one clamp is moving while the other clamp is fixed on the table. Once the right clamp is moving, the table needs to get readjusted to stay with the same imaging area beneath the objective lens. As a measurement of the two movements, a gradient m can be defined in the following way, $m = |\Delta \boldsymbol{X}/\Delta \boldsymbol{x}|$. The gradient is shown for all analyzed experiments (y-axis in Figure 2.8b) and represents the straightness of the inclination between the $\boldsymbol{X}$ and $\boldsymbol{x}$ relation. In Figure 2.8b it can be observed that most values are around 0.5. The differences between the theoretical expected value of $m = 0.5$ and the actual value are mainly due to two factors and can hardly be discriminated. One is the fact that the measurement area is not perfectly in the middle of the strip. The second is that the tissue is not homogeneous.

The small graph in Figure 2.8b shows the relationship between the $\boldsymbol{x}$-direction of the uniaxial tension machine and the $\boldsymbol{X}$-direction of the microscope table for experiment number 9 as an example. The gradient of the curve is nearly constant throughout the complete experiment. Scaling of $\boldsymbol{x}$- and $\boldsymbol{y}$-axis is equal.

More important than the value of m is the standard deviation of m, shown as well in Figure 2.8b. The standard deviation is an indicator of whether the tissue was properly fixed with the clamps or not. If the tissue slides out of the clamps, the value of m would substantially decrease over increasing stretches. This effect was observed in early experiments (data not shown). The data of the given experiments shows a standard deviation typically in the range of lower than 10% of the mean. These results indicate that the tissue was not pulled out of the clamps.

Global movement of measured points Figure 2.7 shows an example measurement. For the computation of local stretches the change of position within one layer is considered. But as the global movement is also available, the global translation in all spatial directions can be investigated. Figure 2.9 follows the global movement of one specific experiment (nr. 9, 20100122-1). It can especially be observed

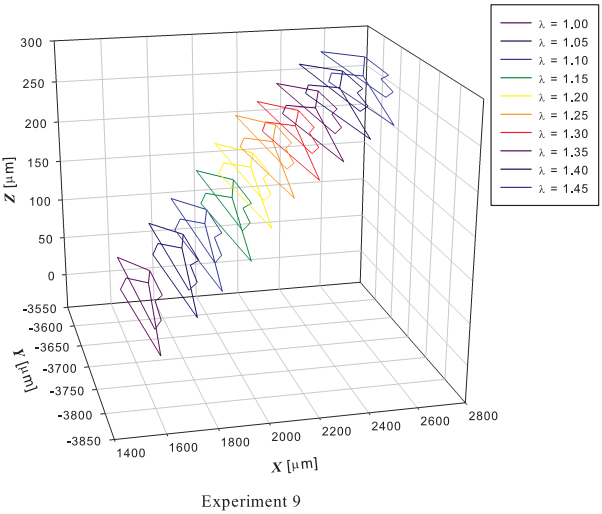

Figure 2.9: Global movement of one measured alveoli while stretching. λ denotes the global stretch applied from the tension machine.

that the movement in $\boldsymbol{X}$- and $\boldsymbol{Z}$-direction is large. The movement in $\boldsymbol{X}$-direction is discussed earlier and follows the main tension direction. The change in $\boldsymbol{Z}$-direction is unexpected, but is a consequence of the bended tissue due to gravity and, secondly, of slightly different clamp heights. The translation in $\boldsymbol{Z}$-direction shows a non-linear behavior which is probably rooted in the combination of two influence factors. At the beginning, the $\boldsymbol{Z}$-translation was larger but for larger global stretches it became smaller. The increase of forces from the beginning of the experiment to the end suggest a decrease of the sagging of the tissue stripe. This behavior is non-linear. Additionally, the different heights of the clamps add a linear shift to the $\boldsymbol{Z}$ translation. The two effects combined result in generally large $\boldsymbol{Z}$ translations while stretching. These kinematics add additional complexity to the experimental procedure for tracking the imaging area. In order to be able to follow the structure, the stretching must be performed slowly, which limits the possibility of imaging alveoli at higher strain rates.

Strip thickness Mechanically important for calculating stress is the thickness of the tissue strips. As the parenchym is a sponge-like material filled with liquid, the thickness of the tissue was measured before and after the experiments.

The experiments show a thickness change of $77.1 \pm 25.6\ \mu m$ (mean and standard deviation). Only the last experiment has an increased change of thickness with $\Delta z = 130\ \mu m$. For the last experiments, the protocol was exactly the same as before. The only difference was the preparation of the tissue. Here, in addition to the cytosol staining, the nucleus of the cells was stained with DAPI. However, there is no indication that this has any influence on slice thickness. The protocol of the experiment and recorded forces are similar to other experiments. The cause of the large change in thickness for the last experiment remains unknown.

short number	experiment number	λ_{global}	Δz [μm]
1	20100119-1	1.45	-
2	20100120-1	1.45	-
3	20100120-2	1.45	70
4	20100120-3	1.675	90
5	20100120-4	1.675	60
6	20100121-1	1.45	60
7	20100121-2	1.45	70
8	20100121-3	1.45	60
9	20100122-1	1.45	130

Table 2.1: Experiment number and thickness change over the experiments. For the first two experiments, the final thickness was not recorded, so that Δz cannot be calculated.

Stretch

Alveolar wall direction As shown in Figure 2.7, the distances between distinctive points were measured and compared to global stretches. Besides analyzing the length of these distances, it is possible to analyze the direction in comparison to the global direction of tension. For a better overview, the connections were placed in 4 subgroups: including when the angle α between the connections and the main direction of tension is smaller than 20 degrees; between 20 and 40 degrees; 40 to 60 degrees; and larger than 60 degrees. The results are shown in Figure 2.10. It can be observed that the fraction of the different directional groups is roughly constant during the experiments. One would expect that for larger global stretches the angle α would decrease because the alveoli become aligned into the main direction of tension. But the results actually suggest that the form of the alveoli stays intact while pulling on the tissue, and the alveolar walls do not become aligned towards the pulling direction.

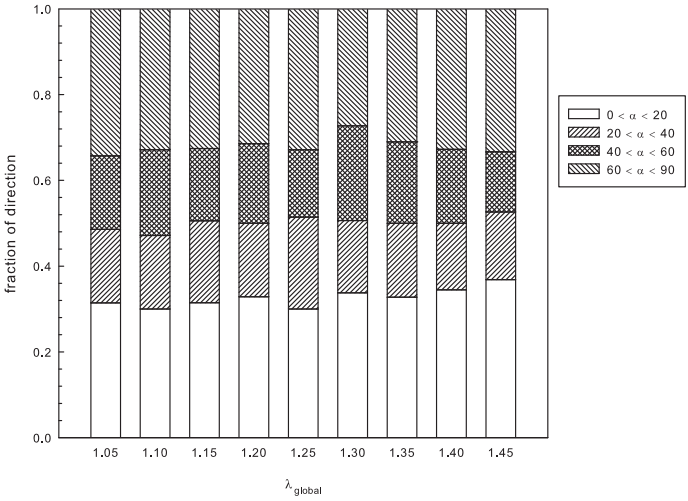

Figure 2.10: Fraction of different directions of local stretch compared to global stretch.

The alveolar tissue seems to form a three dimensional structure which is self-stabilizing and keeps its shape during external pulling. This result relates only to the average behavior. It was observed that especially near large alveoli the walls become aligned towards the pulling direction. But, as Figure 2.10 shows, there is no substantial change of the direction towards the group with $\alpha \leq 20°$. It should be mentioned that the current measurement protocol does not record any rotational effects of the alveoli. It is assumed that the measured points stay within one plane during the experiment. This assumption can be accepted because of the unidirectional tension.

Local to global stretches within one layer The same groups with different angles were used to calculate average stretches. Figure 2.11 shows the local stretches in comparison to the global stretches. In the

group with $\alpha \leq 20°$, the standard error of mean (see Table 2.2 for appropriate n) is also shown. The $\boldsymbol{x}$- and $\boldsymbol{y}$-axis have the same scaling. Figure 2.11 shows that the local stretch is not following the global stretch, otherwise the graph for $\alpha \leq 20°$ would have a 1:1 inclination. The standard error of mean for this group is in general less than 5% of the actual value. Looking at two specific experiments (Figure 2.12) it can be observed that the alveoli shape and the environment play an important role. The measurement line in Figure 2.12a has $\alpha = 11°$ and is more aligned towards the principal tension direction, though the stretch was smaller, than was the case in Figure 2.12b, where the measurement line had a larger inclination ($\alpha = -22°$).

λ_{global}	1.05	1.10	1.15	1.20	1.25	1.30	1.35	1.40	1.45
n	22	21	28	23	21	26	19	20	27

Table 2.2: Sampling size n for global stretches λ_{global}.

On average, the tissue is stretched up to $\lambda_{local} = 1.26$ (26%) with a global stretch of $\lambda_{global} = 1.45$ (45%). The curve in Figure 2.11 shows a linear increase up to $\lambda_{global} = 1.25$, followed by a more non-linear behavior with small increase in stretch from $\lambda_{global} = 1.25$ to $\lambda_{global} = 1.35$, and then rapidly increasing stretch up to $\lambda_{global} = 1.45$. Linear and non-linear behavior of the local stretch λ_{local} is in respect to the global stretch λ_{global}.

Similar behavior is evident in Figure 2.12a, which shows a light plateau region between $\lambda_{global} = 1.30$ and 1.40. The alveoli itself is 73.93 μm long (between measurement point 1 and 4) and nearly a square. The four corners of the square are connected to further alveolar walls. The surrounding tissue is of similar size. Here the measured stretch is very much the elongation of the wall itself. The alveoli is not undergoing large translational changes. The situation looks different in Figure 2.12b. Here the measured length between point 6 and 1 is 119.9 μm and the alveoli is larger. Looking at the three-dimensional data, it might be the case that the image shows an alveolar sac in the bronchial tree. First of all, the measured alveolar wall here is much more aligned towards the main tension direction, and the images do not clearly show

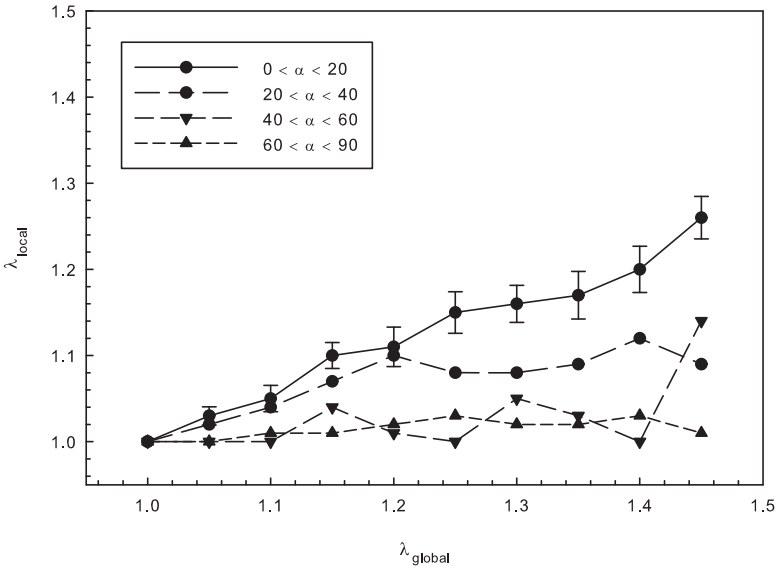

Figure 2.11: Local elongation λ_{local} of alveolar walls compared to the externally applied global stretch λ_{global} to the tissue strip.

how much wall is connected to the measurement points. The stretch curve in Firgure 2.12b is different than in Figure 2.12a. The increase in elongation in Firgure 2.12b is more linear with the exception of the measurement point at $\lambda_{global} = 1.20$.

Both results suggest that the exact stretch behavior is very much dependent on the local environment of the alveoli. The surrounding parenchym and the form and the size of the alveoli play a vital role. In addition to the environment, the average elongation gives important evidence of how local and global stretches are connected. In terms of mechanotransduction, where it is vital to assess the magnitude of local stretch and the biochemical reaction due to an external stretch or strain, the results close the important gap between external and local

stretch.

Beside looking at alveolar walls within the tension direction, the behavior of walls with inclinations larger than 20 degrees are also shown in Figure 2.11. The stretches, especially for inclinations larger then 40 degrees, are moving around $\lambda_{local} = 1.0$. In case of negative values, it was not possible to observe if the tissue was compressed or bending. The standard error of mean for groups with $\alpha > 20°$ is between 0.01 and 0.03 (with n between 9 and 24).

Local to global stretches between layers As shown in Figure 2.7, two layers were measured for every stack. Thus length change between single measurement points in separate layers was also analyzed. The connections do not always represent an alveolar wall. In general, a connection was sought which moves along an alveolar wall, but this was not always possible. The elongation therefore is not so much representing the tissue stretch itself, but more the complete deformation of alveoli. The identification of the second layer in all stacks is equally challenging. The first layer was the layer which was followed during experiments, making the identification of this layer exact. For the second layer, an initial structure in the first stack was identified and then followed in the consecutive stacks. As change of structure is discrete, unlike during experiments, the identification is more difficult.

Figure 2.13 shows the results for two single experiments (7 and 9) with the numbers of the connecting measurement points given in the legend. The first point is in the upper layer while the second point is in the lower layer (Figure 2.7). In general, the distance decreases throughout the experiment. This is in accordance with what would be expected for uniaxial tension. While pulling into $\boldsymbol{x}$-direction, the tissue becomes compressed in $\boldsymbol{y}$- and $\boldsymbol{z}$-direction. The actual magnitude of the compression depends on the actual position. In experiment 7, the shortening is around $\lambda_{local} = 0.85$. In experiment 9, the shortening is much smaller, with $\lambda_{local} = 0.96$. In the latter case, the small change in length is connected to the problem that both layers are not representing the same structure. The structure in experiment 9 (image in Figure 2.12b) has more of an alveoli sac-like structure, which is reflec-

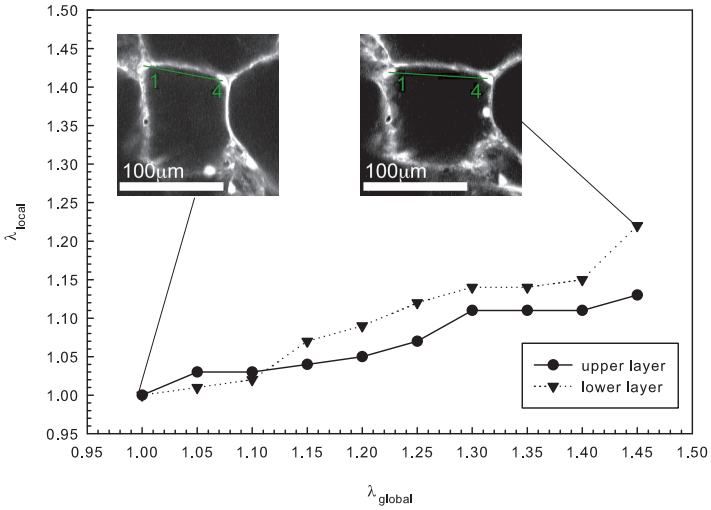

(a) Experiment 7

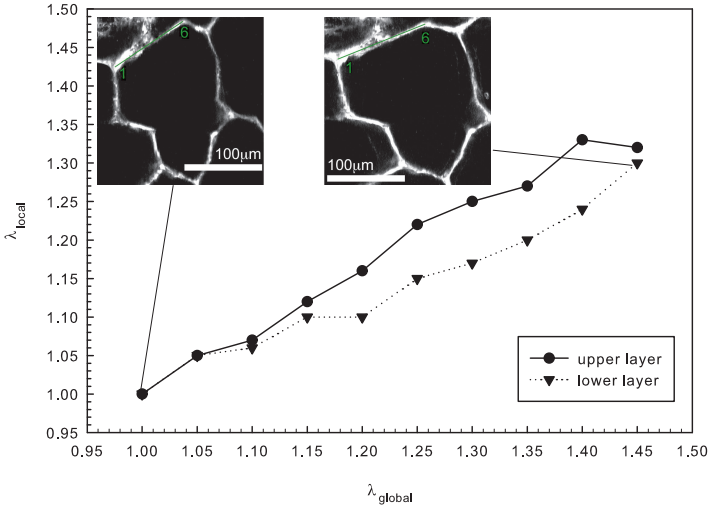

(b) Experiment 9

Figure 2.12: Local to global elongation for two single experiments.

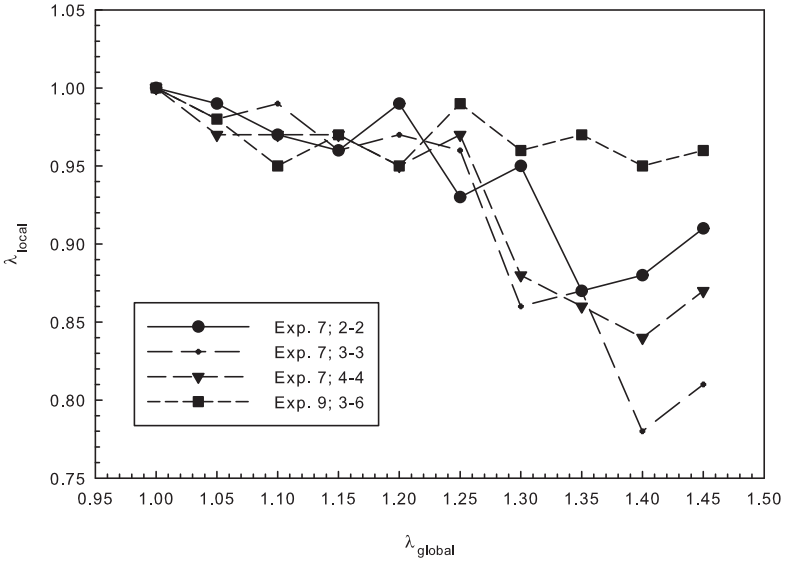

Figure 2.13: Stretch between measurement points (e.g. 2-2: point number 2 in the first layer and point number 2 in the second layer) in different layers of two single experiments (7 and 9).

ted by the fact that on the upper layer, the structure is more elongated in $\boldsymbol{y}$-direction and slimmer in $\boldsymbol{x}$-direction. The surrounding structure changes substantially as well.

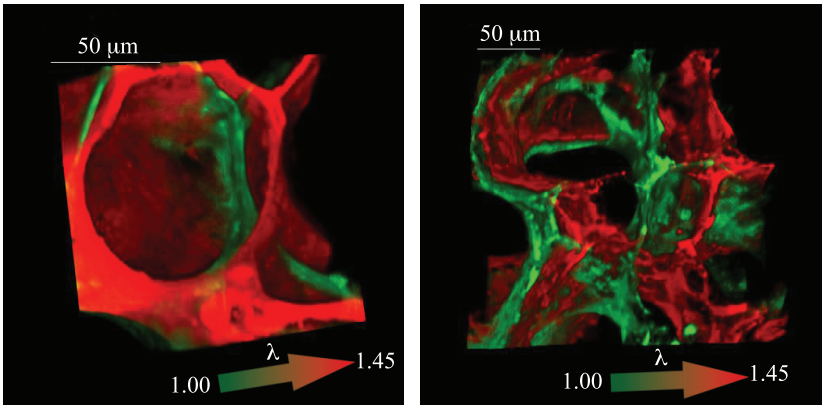

(a) Experiment 7 (b) Experiment 9

Figure 2.14: Three-dimensional representation of two experiments. Green is the reference configuration, red the configuration at $\lambda_{global} = 1.45$

Image rendering Three-dimensional renderings of the stacks of experiments 7 and 9 are shown in Figure 2.14. The change in shape from $\lambda_{glocal} = 1.00$ to 1.45 is clearly visible. The $\boldsymbol{x}$-translation of experiment 9 is larger than of experiment 7, as the size of the alveoli, or alveolar sac, allows larger movement. The latter experiment is shown in Figure 2.15 for different global stretches λ_{global}. The alveoli of interest, which was analyzed, is marked with a red circle. Though the three-dimensional representation may be difficult to interpret, the deformation of the alveoli towards the right lower corner can be observed.

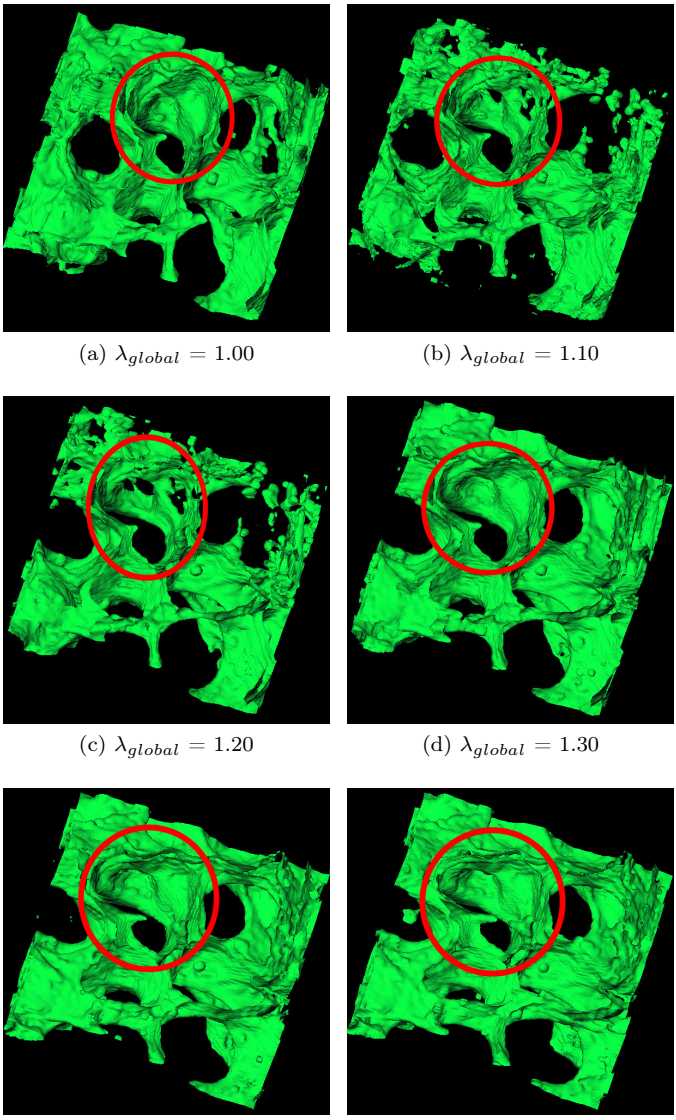

(a) $\lambda_{global} = 1.00$ (b) $\lambda_{global} = 1.10$

(c) $\lambda_{global} = 1.20$ (d) $\lambda_{global} = 1.30$

(e) $\lambda_{global} = 1.40$ (f) $\lambda_{global} = 1.45$

Figure 2.15: Three-dimensional rendering of one stretched alveoli (Experiment 9).

Estimation of alveolar stresses

Representative area for stress calculation As the tissue was stretched, the force was recorded with a 0.5 N force cell. To calculate the stress, the area perpendicular to the applied force must be known. As a straightforward method, it would be possible to use the overall area of the tissue, which is 7000 μm $\times$ 330 μm. But the parenchym has a foam-like structure. So the actual fraction of tissue was measured using the recorded image stacks. As such the fraction was measured in the middle of the alveoli where the stretch was measured. The average fraction of tissue was 0.12 ± 0.027. This results in an average area of $\bar{A} = 279643\ \mu m^2$ for the stress calculation.

The calculation of the occupied area of the tissue is an important parameter. In order to verify that the area fraction from the measured alveoli is representative for the complete tissue strip, the area fraction of all stacks was measured at arbitrary $\boldsymbol{x}$ values of 100, 200 and 300 μm. The average area fraction was 0.12 ± 0.041. The average value for this incidentally measured fraction is the same as the value for the analyzed alveoli given in the paragraph before. The only difference is the higher standard deviation. Evidently, the chosen fraction is representative for the stress calculation.

Stress calculation The following equations describe the calculated stresses from the experiments:

$$\bar{P} = \frac{\bar{F}}{\bar{A}} \tag{2.2}$$

$$P_{local} = \frac{F}{A} \tag{2.3}$$

$$P_{global} = \frac{F}{A_{strip}} \tag{2.4}$$

with $\bar{F}$ and $\bar{A}$ being the average forces and areas over all experiments, F being the recorded force from the tension machine, A being the fraction of area which the tissue occupied, and A_{strip} being the area of the tissue strip normal to the main tension direction $\boldsymbol{x}$. All areas are constant and

measured at the beginning of the experiments, which means that the areas are related to the reference configuration. The force is recorded for every global stretch and updated, meaning that it is related to the actual configuration. Therefore P is the first Piola-Kirchhoff stress as outlined in Chapter 1.3.1. $\bar{P}$ is the median first Piola-Kirchhoff stress over all experiments. P_{local} is the stress of one single experiment, with the recorded force divided by the fraction of tissue measured over all experiments. P_{global} is the force of a specific experiment divided by the area, including tissue and liquid, of the strip perpendicular to the main tension direction.

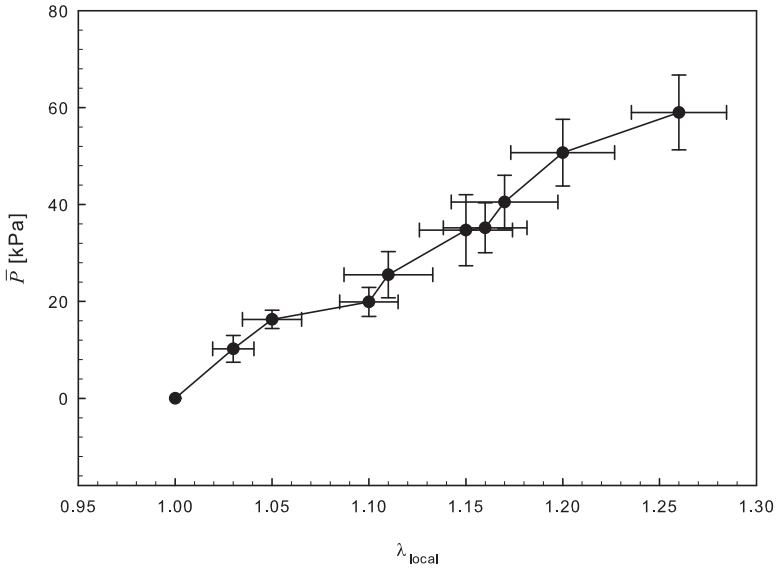

Figure 2.16: Averaged stress-stretch curve of alveolar walls. Averaged first Piola-Kirchhoff stress $\bar{P}$ against averaged local stretch λ_{local} with standard error of mean.

The forces for different stretch steps have been averaged and then

divided by the area A at the reference configuration. With the average local stretches λ_{local} it is possible to draw an average stress-stretch curve (Figure 2.16). The curve denotes on the $\boldsymbol{x}$-ordinate the local stretch λ_{local} and on the $\boldsymbol{y}$-axis the first Piola-Kirchhoff stress $\bar{P}$. The first Piola-Kirchhoff stress is used because it is not possible to measure the area change during experiments. The error bars in Figure 2.16 show the standard error of mean (SEM) for stretch and stress. All errors are based on averages depending on global stretches, and the sampling size for the stress is n = 8.

The stress-stretch curve shows almost a linear behavior. There is some small decrease in the inclination at $\lambda_{local} = 1.10$, but it is not big enough to dismiss a linear relation. The maximum stress is hereby $\bar{P} = 5.9 \times 10^{-8} N/\mu m^2$ or 59 kPa at $\lambda_{local} = 1.26$ with an applied stretch of $\lambda_{global} = 1.45$.

Side-by-side comparison of two alveolar stresses As reported earlier, the local stretches depend on the local environment of the alveoli. For the two experiments (7 and 9), which have been also analyzed earlier, Figure 2.17 shows the corresponding stress-stretch curves. The small graphs show the global stress P_{global} against λ_{global}. Both curves show similar results in terms of magnitude of stress at corresponding stretches. This is especially interesting when compared to the global results shown in the small graph. The maximum force of experiment 7 is around half the maximum force of experiment 9 at the same global stretch. But looking at the local scale, the stresses are comparable. At $\lambda_{local} = 1.15$ the stresses P_{local} are between 30 and 40 kPa. It should be noted that the same fraction of tissue was used to compute the stresses P_{local}. Hence, one would expect that the local scale follows the global. But stretches on the local level are different in experiments 7 and 9, which results in a similar stress-stretch curve on the local level (Figure 2.17). These results suggest that forces on the local scale are balanced by the structure. However, to generally prove that, it would be necessary to compare different areas of the same tissue strip, which was not possible in these experiments. Nevertheless, the result is interesting and it suggests that differences in the global stress-stretch curve might not turn out so differently on the local level. This result is

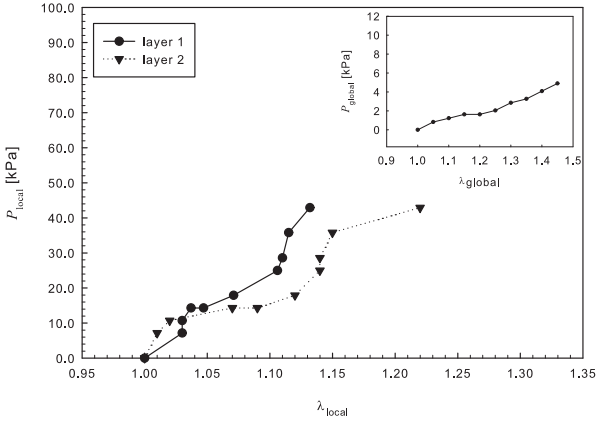

(a) Experiment 7

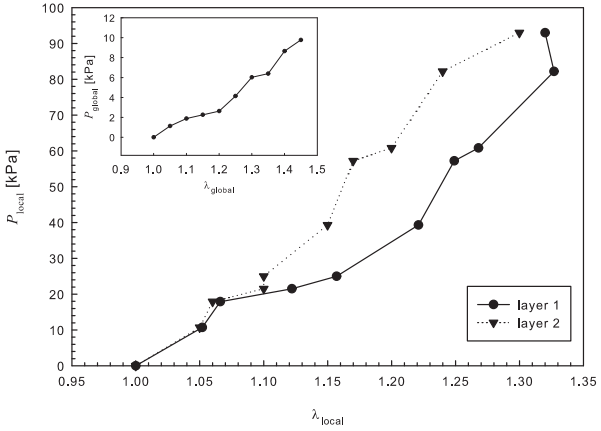

(b) Experiment 9

Figure 2.17: Stress-stretch curve for two single experiments. The large graphs show local values (local first Piola-Kirchhoff stress P_{local} vs. local stretch λ_{local}) while the small graphs show corresponding global values (global first Piola-Kirchhoff stress P_{global} vs. global stretch λ_{global}).

supported by the average stress-stretch curve (Figure 2.16), where the stresses $\bar{P}$ are in the range of 30 to 40 kPa.

2.2.3 Discussion

Previous research investigated alveolar strains either by varying transpulmonary pressure [108] or tension [18]. Both results suggest heterogeneity of parenchym, with the focus of the first study being on the expansion of walls and alveolar cells, and the second on differences between healthy lungs and emphysematic lungs, with an emphasis more on hysteresis than stretches. The results of both studies are in the same range of average strains on the alveolar level (local) compared to applied stimulus (global). On average, the walls are strained by around 20% with a global stretch of $\lambda = 1.3$ (Brewer et al. [18]) or with a transpulmonary pressure of 20 cmH_2O (Perlman et al. [108]). These results suggest that pulling lung tissue by 30% results in the same effect as using a transpulmonary pressure of 20 cmH_2O.

Both studies were carried out using microscopy, which provides sufficient resolution for imaging alveolar walls, though Brewer et al. looked only at the two-dimensional structure of parenchym and both studies did not follow single alveoli over the course of the experiment. The experimental protocol used by Perlman et al., imaged only sub-pleural alveoli, positioned directly below the pleura visceralis. Here we use confocal laser scanning microscopy, which images the tissue in three dimensions with a sufficient resolution to distinguish alveolar walls. Additionally, and in contrast to previous studies, the force is recorded while pulling on the tissue by using a uniaxial tension machine.

Stretch results in comparison to published data Our results show that alveolar walls are stretched by around 25%, with a global stretch of 45%. We find the same heterogeneity in previous studies. As an explanation for the heterogeneity, the three dimensional environment of the measured alveoli is important. Depending on the number of connections of the measured alveoli to surrounding alveoli, alveolar wall stretch can differ greatly. The deformation of the z-direction, the thickness-direction of the tissue strip, is as expected for uniaxial tension. The length increases up to 20%, but shows the same heterogeneity as all other results. Concerning the stretch of alveolar walls, our results confirm earlier two-dimensional findings, but the difference between average local and global stretch is here slightly smaller, 20% vs.

18% local stretch at 30% global stretch. Due to refined measurement points in 5% steps, our results show a clearer lapse between local and global stretches. Up to a global stretch of 25%, the relation between the local and global stretches seems to be linear. For stretches higher than 25%, the relation becomes non-linear with a smaller gradient at the beginning and larger gradient at the end. One interpretation of this curve might be that at the beginning the linear constituents of the alveolar tissue and network effects might play the dominant role, while later the non-linear collagen within the tissue becomes dominant. Another interpretation of this behavior, and of the heterogeneity as well, might be the pre-strain of the tissue. Although a pre-force of 2 mN was used before starting the measurement, it might be that some of the alveolar walls were not fully stretched. In the image stacks, the buckling of alveolar walls was not visible despite expectations since the walls perpendicular to the principal tension direction should buckle. Though stretches of $\lambda_{local} \leq 1.00$ were measured, buckling of walls was not observed in the images. So it was not possible to decide if all alveolar walls were initially stretched. If they were not fully stretched, that might be one source of the heterogeneity.

A second interpretation of the data might have to do with the fact that the tissue is filled with fluid and not with air. The Reynolds number of the fluid in the alveoli is around $Re = 0.02$ with the dynamic viscosity of water, a characteristic length of 100 μm and the assumption that the fluid is travelling for 1000 μm (10 times the average length of an alveoli) during the pulling, which takes around 1 minute. The Reynolds number was chosen so that it is probably overestimated. The low Reynolds number describes a fluid which is diffusion-dominated. Or to describe it more visually, the liquid behaves like thick honey. Looking at the results of the changing thickness of the tissue strips before and after the experiment, it becomes clear that fluid is flowing out of the tissue strip. Due to the high viscosity, the fluid is not able to immediately flow back into the tissue strip after the experiment. On the gradient of the global-local stretch curve, this behavior might be expressed with the two different regimes. Up to the global stretch of 25%, the measured local stretch might be still influenced by the outflow of the intra-alveolar fluid. For higher stretches, the fluid is still there, but might not be dominant anymore, leading to more nonlinear behavior of the local stretches.

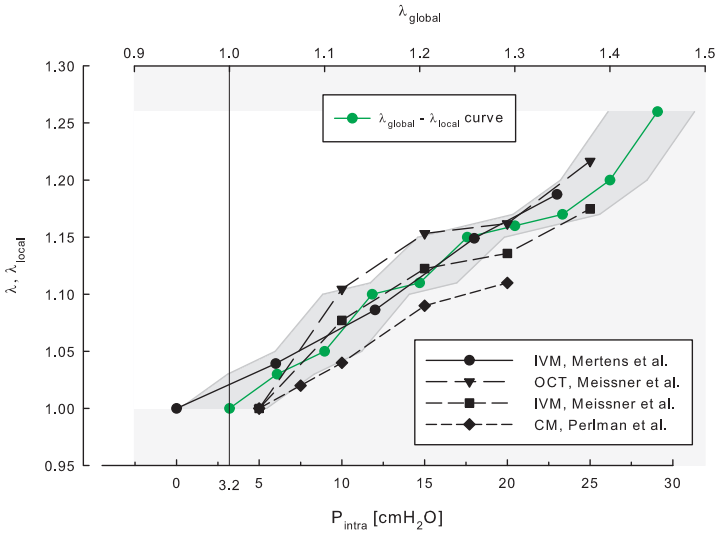

Figure 2.18: Comparison of local stretch results with Mertens et al. [96], Meissner et al. [94] and Perlman et Batthacharya [108]

Alveolar stretches and transpulmonary pressure In interpreting signaling transduction pathways caused by over-stretching, the correlation between the transpulmonary pressure P_{intra} and the global stretch λ_{global} is important. Only then the results from bioreactors or tension machines can be compared to physiological parameters. Here, our results shall be discussed with published data from OCT [94], IVM [96, 94] and confocal microscopy (CM) [108]. Mertens et al. and Meissner et al. measured the alveoli area while Perlman et Batthacharya measured the perimeter. Figure 2.18 shows the result in comparison with the global-local stretch curve from Figure 2.11 ($\alpha \leq 20°$). In order to compare both results, the pre-pressure of our results must be identified. We use the pre-stress and determine the corresponding local stretch $\lambda_{local} = 1.02$ with the help of Figure 2.16. Using the res-

ults from Perlman et Batthacharya, the stretch can be correlated to a corresponding pressure subject to the assumption of linearity. The pre-pressure was found to be $P_{pre} = 3.2\ cmH_2O$. It must be noted that the results from Perlman et Bathacharya represent the upper boundary for the pre-pressure. Now the curves can be correlated to each other and the connection between the global stretch λ_{global} and transpulmonary pressure can be determined. For example, to stretch tissue the same amount as with a transpulmonary pressure of 20 cmH_2O, the global stretch λ_{global} should be 1.38.

Comparison of measured and published stresses Besides the measurement of the local stretches, the forces were also recorded. By measuring the fraction of tissue perpendicular to the main tension direction, the local first Piola Kirchhoff $\bar{P}$ stress can be plotted against local stretches. Measuring the standard stress, here called P_{global}, which takes the whole area of the tissue strip into account, results can be compared with Jamal et al. [72] and Cavalcante et al. [25]. Both studies use rat lungs as well. The stresses of our study are in a comparable range with those of Jamal et al., but the stress results of Calvacante et al. are around 10 times smaller. Stress results can also be compared to other species than rats, e.g. rabbits [98] and dogs [62]. Our stresses are hereby in the same magnitude as those of rabbits and dogs. Interestingly, other publications [154] from the group of Calvacante et al., showed that stresses are around 10 times smaller than other published data. We speculate that the experimental protocol might deliver an explanation for the difference. While in this study low temperature agarose, which dissolves at normal incubation temperatures of 37 °C, was used for tissue slicing, the other study used a temperature of 55 °C, at which the molecular structure might already begin to disintegrate [127]. It should be noted as well that the parenchym of rats might be anisotropic (morphological, not mechanical) as recently shown for mice [100]. Depending on the location of the tissue strip within the lung, mechanical properties might vary.

A possible interpretation of our results is that stresses will get balanced out on the local scale. This interpretation is a result of the differences in local and global stress-stretch curves. As the compar-

ison of individual results shows, global stress is substantially higher in some cases than in others at the same stretch. Interestingly, on the local level, stresses have a comparable magnitude. Smaller local stretch in case of higher stress and vice versa results in similar stress-stretch curves. Though this interpretation should be strengthened in future work, it seems that on the local level, the mechanical properties are comparable. Another conclusion from this finding is that the relation between stress and stretch might be locally constant while the local-global stretch relation is not. One assumption of our model plays an important role here and should be considered in the discussion. The use of P_{local} with the area A representing the real tissue area or effective area results directly in increased stress level, but not in a change of the form of the stress curve. The measurement of a stress stretch curve of a single alveolar wall is currently not possible, so we believe due to this experimental limitation it is worthwhile to make this assumption. For further studies it would be of interest to compare the morphological anisotropic findings of Mitzner et al. [100] with the measurement of local stress-stretch curves.

There is another interesting point to discuss regarding the local stress-stretch curve in Figure 2.16. The curve shows a nearly linear behavior between stress and stretch. Looking at the constituents of alveolar walls — mainly collagen, elastin and proteoglycans — one would expect a non-linear behavior due to the highly non-linear behavior of collagen [51]. Though this form of the curve might result from assumptions made plus the long timescale between each measurement, the exponential answer, especially for collagen, is hard to miss. In consequence, micro-mechanical reasons might also play a part, at least partially. Elastin is shown to be linear, and the influence of proteoglycans for the lung tissue has been shown only for inhibited proteoglycans in comparison to normal tissue samples [72, 25]. In conclusion regarding our experiments, both constituents do not play a role in the discussion regarding the linearity of the curve. Collagen is supposed to be non-linear and shows an exponential stress answer in respect to stretch. Especially for larger stretches, as achieved here, the mechanical impact from collagen should be dominant. However, Figure 2.16 does not show this behavior.

There might be two possible explanations for the non-expected linearity; both involving collagen.

The idea behind the first explanation results from previous experiments. During the measurements of the stretch, Second Harmonic Generation (SHG) [119] was used to image collagen fibers. Unfortunately, this was not successful. One of the speculations at that time was that the free collagen fiber length is not long enough or the fibers are not elongated to be displayed as SHG. Additionally, that observation might now be an exact explanation for the linearity of the stress-stretch curve. The strong non-linearity of the collagen is measurable only for anisotropic collagen bundles or single collagen fibers. If the collagen is randomly orientated in a dense network-like sense, then the mechanical answer would be different and exponential behavior would not be expected.

A second explanation might be that type I collagen is fibrilar whereas the other collagen types are not. In the basal membrane, collagen IV can be found [90] which forms a distinctive network. The mechanical behavior of clearly defined network is hereby different than the mechanical behavior of single fibers. This might explain the linear stress answer as well.

Both explanations stress the same point: The mechanical answer of a network of collagen fibers would be different than the answer from single collagen fibers or collagen bundles. The assumptions made to calculate the stress, existing in the definition of the area, and the experimental protocol influencing both the local stress answer in Figure 2.16. The absence of the dominance of the exponential answer for large stretches, which should be visible even with the assumptions and protocols used here, raises questions about the micro-mechanical influence of the different constituents.

Limitations of experimental setup One limitation of the method should be mentioned and considered for the interpretation of the results. The current analysis protocol does not consider possible rotations of the measured alveoli. Although our results, especially the non-significant change in alveolar wall direction, suggest that this effect plays a minor role, it might lead to a disturbed measurement of the length between distinctive markers. With the current preparation of the tissue, this

effect is not measurable. Future work should be directed to find an appropriate fluorescence tag which binds specifically to localized elements of the tissue as, e.g., the focal adhesions of type I cells. Another idea might be the use of quantum dots, which can act as localized measurement points. Both improvements would substantially enhance the measurement of local alveolar stretches.

Chapter 3

Cell modeling

Mechanical descriptions of cells became an important part of biomechanics in recent years. Different cell models were developed as, e.g., continuum based models [38], tensegrity models [69, 68], fluid based models, and several specialized models. For a detailed overview of models, the reader is referred to Mofrad and Kamm [101] or Lim et al. [86]. Here, an elastic formulation for a cell model is given, followed by an idea to include cell contraction into a continuum based model.

First of all, cells have elastic properties like many engineering materials. The cell consists of constituents, which contribute mechanically, and constituents which are not so important from a mechanical point of view. Humphrey [64] gives a comprehensive overview of the most important mechanical constituents of adherent cells. Using the mechanical properties of the constituents as a basis, the formulation of a cell model in the framework of finite deformation based on invariants shall be investigated. Using strain energy density functions for cell models is motivated by the success of these models for soft tissue [71, 61]. These functions should have two important properties, convexity and stress-free reference configuration. Here, these two properties shall be the focus of the formulation and discussion.

Unlike classic engineering materials, cells can actively change their internal fiber structure over time. The fiber structure is also able to

contract. Therefore, one special area of interest in cell mechanics is the modeling of cell contraction. Deshpande et al. [43, 44] introduced a biochemical model to introduce stresses to account for contraction. His three step model – activation, orientation and assembly of actin stress fibers and contraction by myosin actin cross-bridging – is able to reproduce key elements of cell contraction. It was shown by Wei et al. [148] that the model of Deshpande et al. is also able to reproduce the general stress fiber direction for single imaged cells. Another detailed look at the myosin actin interaction and its geometric assembly in the context of stress distribution was given by Chandran et al. [26]. Taking the angle between myosin head and actin into account, the model replicates the more band-like structure of the stress distribution around actin stress fibers.

Here another approach is proposed, which takes an anisotropic formulation for stress fibers of cells into account. It allows the simulation of stress fiber remodeling, whereby only the change of the stress fiber direction and the degree of anisotropy is considered. The approach is motivated by an idea from tissue modeling. Gasser et al. [55] formulated a distributed anisotropy equation motivated by arterial walls. Here, this approach shall be extended to actin stress fibers. Regarding contraction of the cell, a new approach based on experimental data from cell traction microscopy [147] is investigated, and results are compared to experiments from Butler et al. [22].

3.1 Cell model composition

The cell model is divided into three parts: the isotropic formulation, the anisotropic formulation, and the contraction part. The formulations are based on the main mechanical constituents of adherent cells [64], which are shortly described here.

The cell is enclosed by a cell membrane. The cell membrane consists of several components as e.g. glycocalyx, phospholipid bilayer and actin-rich cortical sublayer. Within the cell there is cytoplasm, the cell nucleus, structural components like actin, intermediate filaments, microtubules, and many dispersed organelles (e.g. mitochondira, Golgi apparatus). The cell membrane can be modeled structurally as a shell as long as internal interactions within the membrane are not of interest. The cell nucleus is in general heterogeneous. Thus, modeling the nucleus as a notably stiffer material is sufficient in many cases. This simplification is not valid if the focus rests on modeling specific nucleus properties or gene transcriptions. The dispersed organelles are of interest for modeling only if specific problems related to them are the focus of the simulation. The main structural components are the actin network, the intermediate filaments, and the microtubules. They contribute substantially to the mechanical properties of cells.

The actin network can hereby form a homogeneous network, as normally observed *in vitro* and *in vivo*, or a bundle like network with distinctive stress fibers [129, 134]. In cell culture, the network shows strong stress fibers connecting focal adhesions with the inner part of the cell. The stress fibers themselves are highly non-linear and can be elongated up to 200% of their initial length. Moreover, stress fibers are believed to be pre-strained and have a motor which allows them to contract.

Microtubules are rigid cytoskeletal filaments with a cylinder form and a diameter of around 25 nm. Through their form, they are able to resist compression. Unlike actin, microtubules cannot build networks. In general, they work alone or in small groups [58].

Next, the isotropic and anisotropic formulation of the cell model is described. This is followed by a formulation to account for the contraction ability of the cell.

3.1.1 Isotropic and anisotropic contributions: strain energy density based formulations

Using continuum-based material descriptions, it is possible to build up a model from scratch mimicking the elastic contributions of different cell constituents (Table 3.1).

Cell constituent	Model	Description
Actin network	Isotropic	Covering the isotropic behavior of the actin network.
Stress fibers	Anisotropic	Dispersion model $J_4 \geq 1$; additional stiffness in the direction of stress fibers (principal stretches).
Microtubules	Anisotropic	Anisotropic dispersion model $J_4 < 1$; during compression microtubules contribution is dominant.

Table 3.1: "Onionskin-like" construction of the cell from a material point of view

Table 3.1 presents the different components which contribute to the mechanical cell model. Using the continuum mechanics framework, the material model shall be formulated in a general description which can later be specialized to emphase certain aspects. As mentioned earlier, the model is divided into an isotropic and an anisotropic part. The following set of equations is a material description for a cell model which tries to minimize the number of parameters but is flexible enough to reflect different mechanical behaviors of cells.

$$\Psi_{cell} = \Psi_{iso} + \Psi_{aniso} \tag{3.1a}$$

$$\Psi_{iso} = c_i\,(I_1 - 3) + \frac{c_i}{\beta}\left(J^{(-2\beta)} - 1\right) \tag{3.1b}$$

$$\Psi_{aniso} = \begin{cases} c_{asf}\left(\frac{J_4}{I_3^{1/3}} - 1\right)^{n_{asf}} & J_4 \geq 1,\ \kappa \in [0, 1/3] \\ c_{mt}\left(\frac{J_4}{I_3^{1/3}} - 1\right)^{n_{mt}} & J_4 < 1,\ \kappa = 0 \end{cases} \tag{3.1c}$$

The model has the following material parameters:

Material parameter	Description
c_i $[N\ mm^{-2}]$	Material parameter for the actin network.
β	Incompressibility parameter.
c_{asf} $[N\ mm^{-2}]$	Material parameter for actin stress fibers (on tension only).
n_{asf}	Material parameter describing the non-linearity of stress fibers.
c_{mt} $[N\ mm^{-2}]$	Material parameter for microtubules (on compression only).
n_{mt}	Material parameter describing the non-linearity of microtubules.

Table 3.2: Material parameters

The anisotropic invariant J_4 is given in equation (1.13). The structural tensor $\boldsymbol{H}$, which is used to derive J_4, is dependent on the orientation vector $\boldsymbol{h}$. For the cell model $\boldsymbol{h}$ is chosen to be the first eigenvector of the deformation tensor $\boldsymbol{C}$.

The corresponding second Piola-Kirchhoff stresses $\boldsymbol{S}$ are

$$\boldsymbol{S}_{iso} = 2\,c_i \left(\boldsymbol{I} - \frac{1}{I_3^{-\beta}} \boldsymbol{C}^{-1} \right) \tag{3.2}$$

$$\boldsymbol{S}_{aniso} = 2\,c_*\,n_* \left(\frac{J_4}{\sqrt[3]{I_3}} - 1 \right)^{n_*-1} \frac{1}{I_3^{\frac{1}{3}}} \left(\boldsymbol{H}^T - \frac{1}{3} \boldsymbol{C}^{-1} \right) \tag{3.3}$$

$$\text{with } * \equiv \begin{cases} asf & J_4 \geq 1,\ \kappa \in [0, 1/3] \\ mt & J_4 < 1,\ \kappa = 0 \end{cases}$$

The model tries to represent all isotropic and anisotropic contributions to the cell mechanics in one term each. The anisotropic direction follows hereby the principal stretch direction and thus depends on local strains. This behavior can be observed in cells, as actin stress fibers often follow the direct connection between focal adhesions and nucleus.

For the cell model described here, the orientation of the fibers in the reference configuration is not yet known. So it would be preferable to get the fiber orientation already in the reference configuration. One way to get the fiber direction in the reference configuration is to define the direction as an input parameter. It was the goal of this formulation to include the cell contraction, the contraction can also be used to derive the fiber direction in the "reference configuration". Actually, to speak here about the mechanical "reference configuration" would be problematic. It would be better to talk about the "equilibrium configuration" of the cell.

3.1.2 Contraction energy: an idea to include cell contraction

Cells are able to contract. With the help of cell traction microscopy, it is possible to measure the energy cells generate [147] by this contraction. Powered by ATP hydrolysis, the action-myosin motors within actin stress fiber bundles generate a force which is transmitted to the ECM. Measuring the deformation of the gel, where cells adhere, and knowing the mechanical properties of the gel, the energy necessary to generate the deformation can be computed. In general, cell traction microscopy is used for adherent cells, which are placed on top of the gel.

Therefore, the measurement of the traction forces is in two dimensions. Koch et al. [77] also showed that the measurement is possible in three dimensions. For lung cells (HASM cells) the energy was measured by Butler et al. [22] in two dimensions. He found values for the traction energy U_t from 0.11 pJ to 0.21 pJ.

Using this active behavior of the cells, it was assumed that the external energy U_t, necessary to deform the gel, is equal to the internal energy of the cell model:

$$\int_{\omega} \Psi_{con} d\omega = \frac{U_t}{V_\omega} = U_{td} \tag{3.4}$$

Here, Ψ_{con} is the strain energy density of the constitutive equation, ω the domain in the physical space, U_t the measured contraction energy from experiments, V_ω the volume of the domain ω and U_{td} the traction energy density.

Using the traction energy density U_{td}, the standard material model in equation (3.1c) can be extended with a contraction term. The question which arises immediately is how the distribution of the energy takes place in the domain ω. For the beginning, one can define an arbitrary function $\mathcal{F}$, the distribution function.

$$\Psi_{con} = \mathcal{F} \cdot U_{td} \text{ , with} \tag{3.5a}$$

$$\mathcal{F} \leq 1 \tag{3.5b}$$

The function $\mathcal{F}$ can be made dependent on mechanical factors or biochemical factors. In a straightforward approach, the function was defined as

$$\mathcal{F} = \frac{1}{n} \tag{3.6}$$

Here, equation (3.6) denotes the uniform distribution of the energy over the domain ω, with n being the number of FE nodes. Another possibility is that $\mathcal{F}$ is dependent on strain, stress, or time. In general, there is no reason not to formulate $\mathcal{F}$ in dependency on chemical potentials, which represent the actin myosin motor. Following the model

from Deshpande et al. [43, 44], which is based on a simplified Hill model [59], the notation of an appropriate distribution function can be made in the following way,

$$\mathcal{F}(J_4) = \begin{cases} 0 & \frac{\dot{J}_4}{\dot{J}_{4,0}} < -\frac{\eta}{\bar{k}_v}, \\ 1 + \frac{\bar{k}_v}{\eta}\left(\frac{\dot{J}_4}{\dot{J}_{4,0}}\right) J_4 & -\frac{\eta}{\bar{k}_v} \leq \frac{\dot{J}_4}{\dot{J}_{4,0}} \leq 0, \\ 1 & \frac{\dot{J}_4}{\dot{J}_{4,0}} > 0. \end{cases} \tag{3.7}$$

The equation uses a simplified Hill model, which is normally applied to muscle contraction. It is adopted to develop a relation between tension and the fraction of the contraction energy density U_{td}. The non-dimensional parameters $\bar{k}_v$ and η are the fractional reduction in tension when the shortening rate increases by the reference value, $J_{4,0}$, and the fraction of activation of the fiber bundle, with $\eta = 1$ the maximum biological activation. In the Hill model, J_4 would be the length of the fiber at the time of activation, depending on a calcium model. Here no calcium model is used to trigger the activation, so the assumption is made that the contraction starts at the reference configuration, which means that $J_{4,0}$ can be defined as 1.0. Equation (3.7) is also able to use a local energy level, e.g., based on ATP, instead of U_{td}. In terms of cell traction microscopy, it would instead be possible to use the energy of a single focal adhesion for the computation of equation (3.7). This would lead to a localized energy level which is experimentally available.

3.1.3 The complete cell model

The complete cell model is formulated as the summation of the isotropic, anisotropic, and contraction part as shown in equation (3.8a). Using the previously defined strain energy density function in equation (3.1c), the contraction part can be modeled as an additional anisotropic Neo-Hookean-based energy density function (equation (3.8b)) using the distribution function in equation (3.6). In order to compute equation (3.8b), the anisotropic invariant $J_{4,con}$ is used. The invariant can be derived from equation (3.5a) and the Neo-Hookean material law in its volumetric decoupled formulation.

$$\Psi_{cell} = \underbrace{\Psi_{iso} + \Psi_{aniso}}_{\text{elastic part}} + \underbrace{\Psi_{con}^{(g)}}_{\text{contraction part}} \tag{3.8a}$$

$$\Psi_{con}^{(g)} = c_{con}\Big(J_{4,con} - 1\Big)^{n_{con}}, \text{ with} \tag{3.8b}$$

$$J_{4,con} = I_3^{1/3}\left(\sqrt[n_{con}]{\frac{\mathcal{F}\cdot U_{td}}{c_{con}}} + 1\right) \tag{3.8c}$$

The material parameters are:

Material parameter	Description
c_{con} $[N\ mm^{-2}]$	Elastic parameter of actin fiber bundles; can be chosen as $c_{con} = c_{asf}$.
n_{con}	Describing non-linearity; generally defined as $n_{con} = 1$.

Table 3.3: Material parameters

The corresponding second Piola-Kirchhoff stress tensor $\boldsymbol{S}_{con}$ of equation (3.8b) is

$$\boldsymbol{S}_{con} = 2n_{con}c_{con}I_3^{-1/3}\left(J_{4,con} - 1\right)^{n_{con}-1}\boldsymbol{H}^T, \tag{3.9}$$

with $\boldsymbol{H}$ the structural tensor defined in equation (1.11).

It is important to mention that the usage of the contraction behavior of the cell serves two important purposes. The first is the generation of an anisotropic direction for the "equilibration configuration" of the cell. Secondly, it describes stresses of focal adhesion better than using only the isotropic and anisotropic part of the model, because otherwise forces generated by actin stress fibers would be neglected.

The data for the simulations are provided by Butler et al. [22]. The shear modulus of the cell was $G = 60\ kPa$, Poisson ratio $\nu = 0.35$, n_{asf} and $n_{con} = 2$ and $U_t = 0.12\ pJ$. A simplified model in the form of a cube with a length of 10 μm and a thickness of 1 μm was simulated.

The edges of the cube were treated as Dirichlet boundary conditions and the top and bottom parts were allowed to move only in $\boldsymbol{x}$- and $\boldsymbol{y}$-directions.

3.2 Results

Cells can be covered by a wide range of different models [101], from continuum-based models to biochemical models for transport processes. Here, the approach was to develop a general model based on strain energy density functions representing the different constituents of the cell in the framework of finite strains.

3.2.1 The isotropic and anisotropic formulation

The cell model consists of an isotropic part and an anisotropic part. The degree of anisotropy is adjustable with the parameter κ from equation (1.11). The parameter κ can either be set as a constant or as an active parameter which changes during the simulation. Hence the influence of κ on the global equation, in terms of stress, is of interest. Figure 3.1 shows this influence. The material parameter c_i and c_{asf} were both set to 100 Pa. The element was uni-axially stretched to $\lambda = 1.35$ in the $\boldsymbol{x}$-direction.

The isotropic result in Figure 3.1 shows the exclusive isotropic contribution of equation (3.1c). All other results show the stress result for different κ with the extreme values of $\kappa = \frac{1}{3}$ for the isotropic invariant J_4 and $\kappa = \frac{1}{24}$ for a nearly anisotropic case of J_4. It can be observed that, for the isotropic case, κ has only a small effect on the combined stress. Only 4% of the isotropic stress is contributed by the anisotropic part. The stress level rises, as expected, as the degree of anisotropy increases for smaller κ. The maximum stress for $\kappa = \frac{1}{24}$ is 2.11 times larger than for the isotropic case.

The influence of the direction for uniaxial tension is shown in Figure 3.2. The normalized stress (in respect to the isotropic stress) has been computed for different κ. The fiber direction is in $\boldsymbol{h} = \boldsymbol{e}_x$ or $\boldsymbol{h} = \boldsymbol{e}_y$ while the tension direction is always in $\boldsymbol{x}$-direction. The analyzed stress is also the stress in $\boldsymbol{x}$-direction. Only the anisotropic part in equation (3.4) has been used, and the volume has been preserved by a penalty function. The results show an expected increase of stress for higher anisotropy with the anisotropic direction in tension direction. The behavior is nearly linear. In case of an anisotropic direction perpendicular to the tension direction, the stress in tension direction

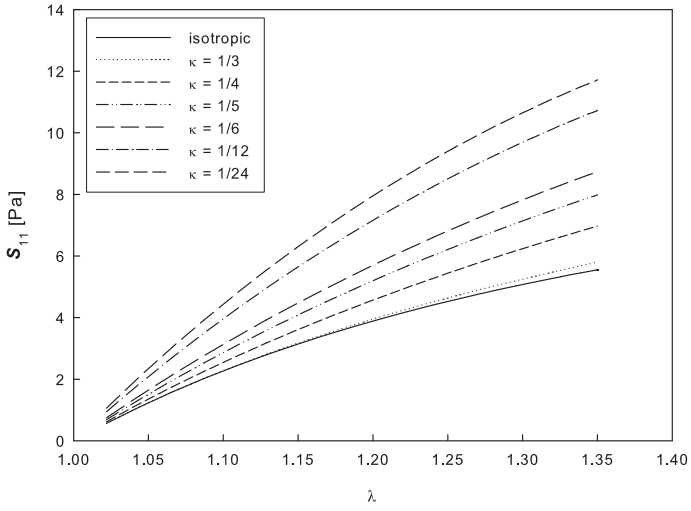

Figure 3.1: Influence of κ on second Piola-Kirchhoff stress $\boldsymbol{S}$.

decreases. Energy-wise, the $\boldsymbol{e_y}$-direction is able to absorb more energy, so less energy is left for the stress in $\boldsymbol{x}$-direction. For higher anisotropies of $\kappa \geq \frac{1}{7}$, the stress is even negative.

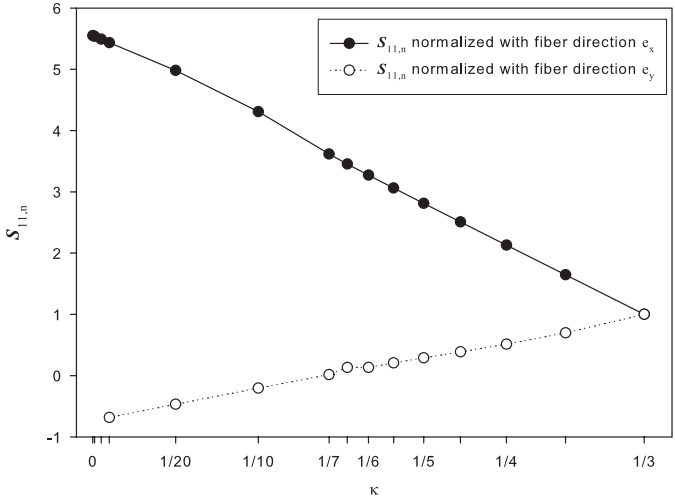

Figure 3.2: Dimensionless stress $S_{11,n}$ in respect to fiber direction $\boldsymbol{h}$ and κ .

The behavior of the Helmholtz Free energy density Ψ and the Cauchy stress $\boldsymbol{\sigma}$ is shown for the anisotropic part of equation (3.1c) in Figure 3.3 and in Figure 3.4. Gasser et al. [55] proved that the anisotropic dispersion part of equation 3.1c is convex for $J_4 \geq 1.0$. Because the equation will be used for compression to represent microtubules, the uniaxial case was investigated to better understand the non-convexity of the equation. Figure 3.3 shows Ψ for different κ. In the complete anisotropic and isotropic cases, the function shows a normal expected behavior. But for $\kappa = \frac{1}{6}$ the equation has a clear maximum ($J_4 \leq 1$), hence it is not convex anymore. Figure 3.4 presents the Cauchy stress σ and the Second Piola-Kirchhoff stress $\boldsymbol{S}$ for the anisotropic part of equation (3.4). Due to the issue with convexity and the anisotropic behavior of microtubules, $\kappa = 0$ has been chosen for the compression

case. This results in a non-smooth transition between compression and tension. Additionally, it can be observed that the stress changes its algebraic sign in case of $\kappa \neq 0$. This behavior is not compatible with the behavior of microtubules.

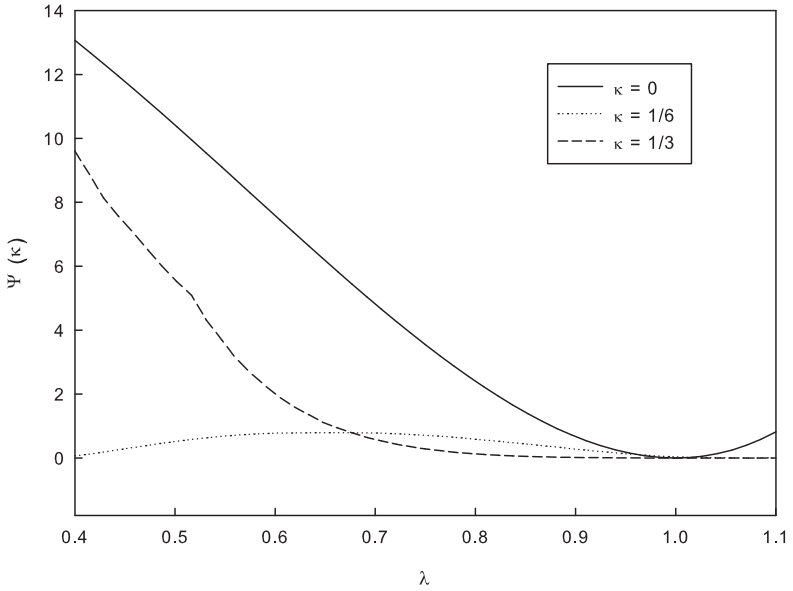

Figure 3.3: Strain energy density Ψ for uni-axial stretching at various κ-levels.

3.2.2 The cell contraction

The contraction of the cell was simulated using data from Butler et al. [22] for HASM cells. The cell was represented by a cube with fixed edges. Then, the contraction energy U was added in 10 steps following equation (3.6). The stress can be seen in Figure 3.5. It is mainly located at the edges where the cube is fixed. The maximum stress $\sigma_{vonMises}$ is in the range of 2.00 Pa. The stress is clearly decreasing from the edges

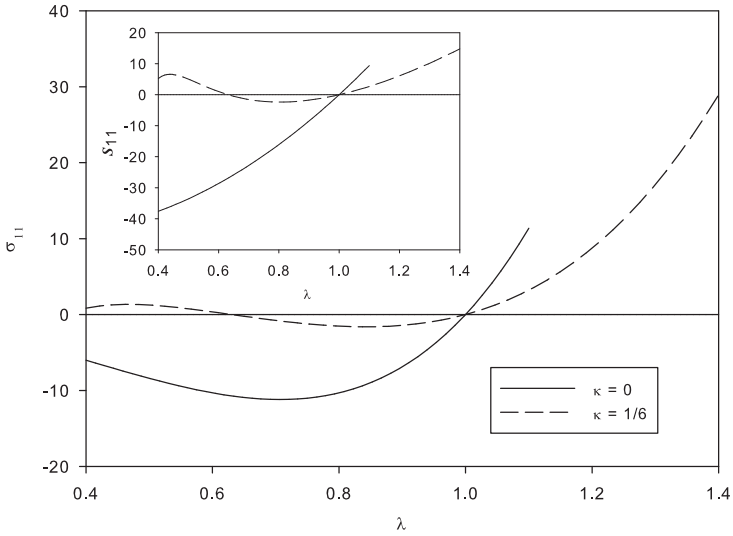

Figure 3.4: Stresses σ_{11} and S_{11} for two different κ.

towards the center. In the middle, the stress is significantly smaller, with values around 0.32 Pa. The stress distribution is, as expected, higher at the fixation of the body and lower in areas where elements can contract. This behavior is in generally consistent with cell traction microscopy, where high deformation and stresses are localized around focal adhesions.

Figure 3.6 shows the corresponding fiber distribution resulting of the contraction. The initial reference fiber distribution was in $\boldsymbol{e}_x$ direction. Fibers are aligned towards the edges of the cube and crossed each other in the middle. It should be noted that, in general, the fiber distribution is three-dimensional, though here the problem is mainly two-dimensional due to the applied boundary conditions. During the simulations it was observed that at the corners, some of the directions tended to point heavily towards the through-thickness direction of the cube, which produced large stresses in that direction. Hence the top

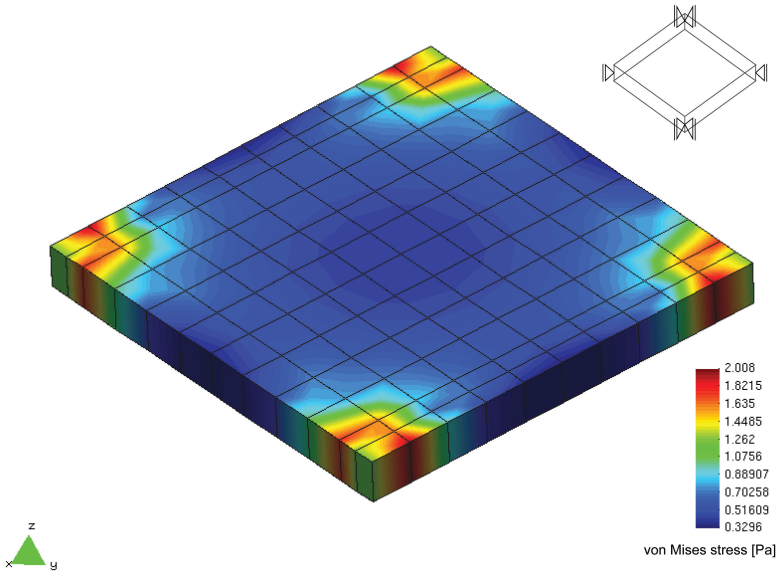

Figure 3.5: Von Mises stress for the contraction of a simplified cell model.

and the bottom of the cube have been fixed in $\boldsymbol{z}$-direction, assuming a plane-strain condition, as these stresses are a product of the fixed corners of the cube.

The fiber distribution in Figure 3.6 is in accordance with expectations. Due to the fixation of the corner, the principal stress direction is between the edges. The fiber direction is in accordance with expected results from stress fibers in cells. Here, they connect different focal adhesions with each other and with the cell nucleus. This behavior is mimicked here by the proposed cell model.

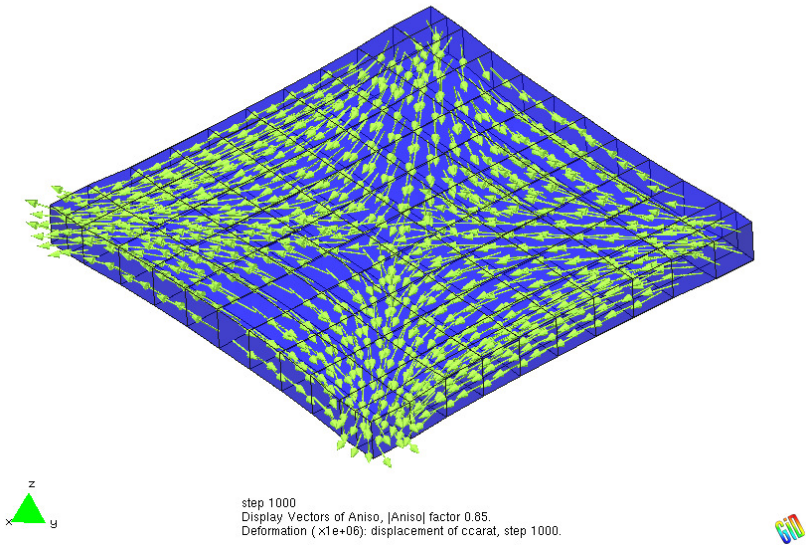

Figure 3.6: Fiber direction of the anisotropic cell formulation after contraction.

3.3 Properties of the cell material model

In the literature several cell material models exist. Depending on the cell type (e.g. adherent or free), the topic of interest (e.g. calcium flow or force transfer), constituents of the cell (e.g. lipid membrane or actin network), an appropriate model must be chosen. Here a cell model was proposed and investigated which is formulated within the finite deformation framework. It is based on a continuum description of the mechanical behavior of cell constituents. There are several advantages for the formulation of a cell model within this framework. First, the constitutive models can be easily integrated in FE simulations, which is a versatile method to simulate cell behavior. Second, the model can be easily combined with other formulated models, e.g. viscoelastic models and/or convection-diffusion models for biochemical signals. Third, the finite deformation framework and FE provide an excellent framework for large deformation and large system simulations, as is the case for cells. Hence, the proposed elastic, anisotropic model shall be discussed here in detail, especially in terms of convexity and stress-free reference configuration. As forces and stresses are small in cells, models should satisfy the latter property.

3.3.1 Stress-free reference configuration

The isotropic part in equation (3.1b) is straightforward a linear formulation following the Neo-Hookean material law, combined with a penalty term to enforce incompressibility. As a side note, it should be mentioned that cells are, depending on the timescale, not generally incompressible. Mass transport over the cell membrane can be observed, especially over longer timescales. For small strains, the parameter β can be related to the Poisson ratio ν, and c_i to the Young modulus. For large strains, one should be careful how the penalty function enforces the desired volume change. The elastic part and the penalty function for the isotropic part are convex and stress-free in the reference configuration. However, it should be mentioned that the stress-free reference configuration is only given when both terms, the elastic and the penalty part, are used. Hence, both parts are not easy to separate and, in case of a different formulation of the penalty function, it should be

done in a way that preserves the stress-free reference configuration. Another possibility to achieve a stress-free reference configuration is to use the decoupled version of the Neo-Hookean formulation, as shown in equation (3.10). Here, the formulation of the penalty function Ψ_p is arbitrary, but should then fulfill the stress-free reference configuration by itself.

$$\Psi = c\left(\frac{I_1}{I_3^{\frac{1}{3}}} - 1\right) + \Psi_p \tag{3.10}$$

The Neo Hookean formulation, as in equation (3.2), is a combination of an elastic and a penalty part, which compensate each other in the reference configuration where $\boldsymbol{C}^{-1} = \boldsymbol{I}$. This property allows a very simple and stable formulation of a material law for large strains.

This property of the Neo-Hookean formulation is exactly the reason why a simpler formulation of the anisotropic part in equation (3.1c) is not in accordance with the desired conditions. The following anisotropic formulation would be actually preferable to be used:

$$\Psi = c\left(\frac{J_4}{I_3^{\frac{1}{3}}} - 1\right), \text{ with} \tag{3.11}$$

$$\boldsymbol{S} = 2\partial_{\boldsymbol{C}}\Psi = 2cI_3^{-\frac{1}{3}}\left(\boldsymbol{H}^T - \frac{1}{3}J_4\boldsymbol{C}^{-1}\right) \tag{3.12}$$

The formulation in equation (3.11) would not only be mathematically beautiful but biologically as well. As long as no stress fibers exist, the low contribution (Figure 3.1) to the stress answer would represent a more fluid-like state of the cell, where actin monomers build no fibers. With the change of κ, the mechanical answer of the equation would increase and would represent an increased actin polymerization within the cell.

To satisfy the stress-free reference condition, the term in parentheses in equation (3.12) must vanish. The inverse right Cauchy-Green tensor $\boldsymbol{C}^{-1}$ is equal to the identity tensor in the reference configuration. So it is necessary to have closer look at $\boldsymbol{H}^T$. Recall from equation (1.11) that

tensor $\boldsymbol{H}$ is a mixture between the identity tensor $\boldsymbol{I}$ and the structural tensor $\boldsymbol{M} = \boldsymbol{h} \otimes \boldsymbol{h}$, with $\boldsymbol{h} = \boldsymbol{e}_x$ as an exemplary direction. Looking at three particular κ, $\boldsymbol{H}$ takes the following form:

$$\begin{aligned}
[\boldsymbol{H}|_{\kappa=0}] &= \begin{bmatrix} 1 & 0 & 0 \\ 0 & 0 & 0 \\ 0 & 0 & 0 \end{bmatrix} \\
\left[\boldsymbol{H}|_{\kappa=\frac{1}{5}}\right] &= \begin{bmatrix} \frac{3}{5} & 0 & 0 \\ 0 & \frac{1}{5} & 0 \\ 0 & 0 & \frac{1}{5} \end{bmatrix} \\
\left[\boldsymbol{H}|_{\kappa=\frac{1}{3}}\right] &= \begin{bmatrix} \frac{1}{3} & 0 & 0 \\ 0 & \frac{1}{3} & 0 \\ 0 & 0 & \frac{1}{3} \end{bmatrix}
\end{aligned} \tag{3.13}$$

In order to compensate $\boldsymbol{C}^{-1}$, κ must be $\frac{1}{3}$. In this case it would be possible to modify equation (1.11) in a way that $\boldsymbol{H} = \boldsymbol{I}$. For all $\kappa \neq \frac{1}{3}$ the stress-free reference condition is not given. In that case, one could simply use an isotropic formulation. It should be mentioned that, in general, especially if the anisotropic direction is following principal strains or stresses, the dyadic product will produce a non-sparse tensor $\boldsymbol{M}$, which thus will never fulfill the stress-free reference condition. For that reason, the simple formulation in equation (3.11) is not suitable for the formulation of a material law.

One possibility to achieve the stress-free reference configuration is to extend equation (3.11) with a power law formulation. This was done in the final implemented version for the cell model in equation (3.1c). The parameter n_{asf} and n_{mt} have the ability to not only reassemble the power law behavior of experimental data, but they also ensure the stress-free reference configuration as can be seen in equation (3.3). As the term in parentheses with the anisotropic invariant J_4 is preserved, the stress $\boldsymbol{S}_{aniso}$ is zero for the reference configuration ($J_4 = 1$). In conclusion, formulation (3.1c) is satisfying the stress-free reference configuration condition.

3.3.2 Convexity

Another important condition is convexity. Convexity means ensuring that the constitutive equation has only one minima. Fundamental work on convexity was done by Schröder and Neff [121, 122]. The complete strain energy equation can be additively built by single quasiconvex terms as introduced by Morrey [104]. The integral inequality of Morrey is difficult to handle, so the criteria of polyconvexity in the sense of Ball [8] seems more practical. Schröder and Neff [121] observed, Corollary B.7, that if a function $P : \mathbb{R}^n \rightarrow \mathbb{R}$ is convex and $P(Z) \geq 0$, then the function $Z \in \mathbb{R}^n \rightarrow [P(Z)]^p$, $p \geq 1$ is also convex. Since $(J_4/I_3^{\frac{1}{3}} - 1)$ is convex for $J_4 \geq 1$, equation (3.1c) is convex as well for $n_{asf} > 1$. It should be noted that the replacement of $J_4/I_3^{\frac{1}{3}}$ by J_4 does not violate the convexity criterion. More generally it was observed by Schröder and Neff, Lemma B.9, that a constructed function $\mathbb{R} \rightarrow \mathbb{R}$, $X \rightarrow m(P(X))$ is convex, if $P : \mathbb{R}^n \rightarrow \mathbb{R}$ is convex and $m : \mathbb{R} \rightarrow \mathbb{R}$ is convex and monotone increasing. Applied to the polynomial formulation with $(...)^p$, the convexity is ensured if $p > 0$. Then the function is convex and monoton increasing. But Corollary B.7 does not allow values for $(J_4/I_3^{\frac{1}{3}} - 1) < 0$. This results in the condition that $J_4 \geq 1$. Mechanically spoken: The equation is not convex for compression. Following Lemma C.3 in [121] it would be possible to construct a convex function in such a way that only J_4 or I_3 is used and not e.g. $(J_4 - 1)$. But as a result, the stress-free reference configuration would be lost, as the "-1" would be missing from the inner parentheses part of equation (3.1c). In conclusion, it can be observed that, using anisotropic invariants for the formulation of an energy strain density function, the formulations are non-convex on compression, but concurrently fulfill the stress-free reference configuration condition.

3.3.3 Connecting the anisotropic parameter κ to polymerization and depolymerization

Recall equation (1.11), which assembles the structural tensor $\boldsymbol{H}$ from the identity tensor and the anisotropic direction. The important parameter is κ, which controls the degree of anisotropy. From a modeling

point of view, κ represents the level of stress fibers within the element. Consequently, the question arises whether κ can be connected to a biological parameter. As a thought experiment, we assume for the moment that the concentration of actin monomers, regardless if bound as actin fiber or not, is constant within the volume of interest. The rate constants k_{on} and k_{off} for polymerization and depolymerization are given by Pollard [109]. The effective radius of one actin filament was found to be $d = 4\ nm$ [17]. The cross section of actin stress fibers is estimated to be a circle with a diameter of $d_{asf} = 100\ nm$ [42]. From these values we estimate that around 157 actin filaments are building one actin stress fiber. In other words, 157 actin monomers are necessary to elongate the stress fiber for $\delta \approx 2.7\ nm$ [102], which leads to a line density of $\rho_{asf} \approx \frac{157}{2.7}\ nm^{-1} = 58.15\ nm^{-1}$. Here the assumption is made that the stress fiber is built by polymerization of single monomers rather than the assembly of actin filaments. This assumption is probably an oversimplification, but it keeps the thought experiment simple to concentrate on how κ can be connected to cellular stress fibers. Let us further assume that all monomers are used to build stress fibers. The parameter κ is defined between 0 and $\frac{1}{3}$. Let us define κ as a product of $\frac{1}{3}$ and χ as written in equation (3.14), with χ representing the level of polymerization.

$$\kappa := \frac{1}{3}\chi, \text{ with } \chi \in [0, 1] \tag{3.14}$$

The level of polymerization is defined by the fraction of bound actin monomers N_{am} to necessary monomers N_{asf} for one filament. The level of polymerization is $\chi = 1$ when all monomers necessary to build a stress fiber are bound and is $\chi = 0$ in case no stress fiber is assembled.

$$\chi = \frac{N_{am}}{N_{asf}}, \text{ with} \tag{3.15a}$$

$$N_{am} = \rho_{asf}\delta\left(Mk_{on} - k_{off}\right)\Delta t \tag{3.15b}$$

$$N_{asf} = \rho_{asf} l \tag{3.15c}$$

Here, M is the concentration of available monomers, Δt the time period in which the volume of interest is observed, and l the length of

the volume of interest in the anisotropic direction or the persistence length of actin stress fibers. Putting it all together, κ can be written as

$$\kappa = \begin{cases} 0 & \chi < 0 \\ \frac{1}{3}\frac{\delta}{l}\left(Mk_{on} - k_{off}\right)\Delta t & 0 \leq \chi \leq 1 \\ \frac{1}{3} & \chi > 1. \end{cases} \tag{3.16}$$

Let us finish the thought experiment with the conclusion that with this simplified model it is possible to connect the parameter κ with the actin filament polymerization. The model can be extended to several areas. For instance, the concentration M can be a parameter itself and modeled by one dimensional convection-diffusion models for the cell. With such a model our first assumption, a constant number of monomers in a volume in our thought experiment, can be discarded.

3.3.4 Cell contraction

The stresses caused by contraction have been imaged by Butler et al. [22] in two dimensions and Koch et al. [77] in three dimensions. They calculated the stresses and strain energy which was caused by cell contraction. Here a simple model was developed which takes advantage of these experimental results and adds the contraction in an additive and straightforward way to existing strain energy formulations. The stress found by Butler et al. [22], where the strain energy $U = 12\ pJ$ was used, were up to 400 Pa at one localized spot (focal adhesion) and 100 - 150 Pa at two other stress spots. Comparing these stress results with the simulation, it becomes clear that computed stresses are much lower (Figure 3.5). Depending on the evaluation point, computed values are 100- to 200-fold smaller than measured stresses. The origin of this discrepancy might be found in the distribution function $\mathcal{F}$. A homogeneous distribution is not advanced enough to produce high enough stresses, because the local deposited contraction energy is too small. Another factor is the geometric situation between the measured cells and the simulated simplified model. This difference accounts for some stress discrepancy as well. However, overall stress distribution is comparable with the results from Butler et al. [22]. Stresses are localized to spots where the domain is fixed. The good agreement of

the localized stress applies as well to the stress fiber directions (Figure 3.6). The preferred direction between fixed spots can be observed in experiments. In comparison to the similar geometric model of Deshpande et al. [43], it can be observed that the anisotropic direction in the model proposed here is equal to the biochemical motivated model of Deshpande et al. The comparison with published results shows that the model is suitable to compute fiber directions of cellular actin stress fibers for the reference configuration.

Chapter 4

Integrin modeling

Integrins are, from a mechanical point of view, force transducers from the extracellular matrix (ECM) to intracellular proteins like actin, FAK, vinculin etc. [75]. For a better understanding of signaling cascades, it would be of great interest to know the magnitude of forces, which are transferred from the ECM to the intracellular lumen. Though a lot is known about the activation of integrins, observing experimentally the mechanical properties of bonds is difficult. A standard experiment is to pull cells from substrates with AFM. With this method, binding forces and binding mechanics can be observed indirectly only because the mechanical properties of the cell are measured as well. Li et al. [85] found measurements of around 60 pN for the integrin-fibronectin bond rupture force. For cancerous cells, rupture forces have been reported as low as 20 pN (Fabry et al.; personal communication). Though AFM is able to measure rupture forces of single integrin-ECM contacts, it is not able to resolve the mechanics on a molecular scale. Here the use of molecular dynamics simulations can be advantageous because the exact molecular behavior can be investigated. However, considering the simulation of complete alveolar cells, molecular dynamics must be somehow connected to continuum models or Finite Elements (FE) as the atomistic simulation of complete cells is not possible.

Methods to bring FE and MD together In recent years several approaches have been published which bring together molecular dynamics and finite elements. Here we attempt to classify the approaches in two different categories, namely the cases where FE represents the molecular structure and where molecular results are used in a homogenized way in FE.

FE representation of molecular structures Recently, a complete description of the governing equations for different molecular potentials was published by Wackerfuss [145]. Every FE node represents here one atom. The interactions between these "atoms" are described by an interaction potential. The work of Wackerfuss describes bonded and non-bonded interactions and is complete in the sense of available potentials. The reader is referred to this work for a more detailed description. The method allows the simulation of molecular structures with Finite Elements, but necessarily discretizes small structures as well. Looking at proteins, the computational cost is expected to be the same as with molecular dynamics. For graphene sheets or carbon tubes, used as an example in this work, the computational costs are not so high because the thermodynamic energy can be neglected. As a consequence, long dynamic simulations are not necessary.

Homogenization of molecular structures Another way to include molecular information in FE was shown by Belytschko et Xiao [11, 152]. They used a bridging domain method to couple graphene sheets with Finite Elements. The interaction between the α-carbons is also described by potentials and handled as elastic energy. They show two different coupling methods, either directly attached systems (FE and molecular), or with a bridging domain in the middle where the energy of every system is weighted depending on distance between both systems. In order to solve the equations, the system is minimized, which is feasible in cases where thermal energy plays no significant role. The work of Belytschko et al. was recently formulated in a more mathematically stringent way by Badia et al. [7], who addresses the problem with "ghost stresses" and the non-local nature of atomistic problems. The currently mentioned methods are all based on energy, but in general it is also possible to couple the two systems by force. One example

is given by Badia et al. [6]. Different bridging domain approaches are compared in an overview of Miller et al. [99] and the reader is referred to this work for a more detailed description.

The previously mentioned works generally apply carbon based materials, where thermal energy can be neglected. In terms of homogenization, there was work done by Tang et al. [136, 137], who used a comic representation of the MscL channel in escherichia coli for continuum simulations. Enhanced by the work of Chen et al. [28] they used different methods to derive the mechanical properties of their structures, e.g., normal mode analysis and energy transfer of molecular simulations. Some of the methods used were based on dynamic simulations and included thermal energy. Nevertheless, they show that their model nicely represents the mechanical behavior of the channel, but with the drawback that the comic representation is a sole representation of tertiary protein structures and has no physical meaning.

Here the approach was made to use a slightly different interpretation of energy transfer based models to describe the mechanical behavior of the integrin-ECM bond. The approach extends current work in this field by including thermal energy but still preserves flexibility to use a wide range of molecules and methods on the molecular and the continuum side. The energy which is exchanged is the Helmholtz-Free energy.

The mechanical behavior of the integrin-ECM bond was investigated using the molecular structure 1DZI [50] from the Protein Data Bank. The structure consists of the I domain of the $\alpha_2\beta_1$ integrin bound to tropocollagen. The I domain is especially suitable to use as a model molecule because it is found in several α subunits of integrins, namely α_1, α_2, α_L, α_X, α_d and α_M [33]. Its three dimensional structure is hereby the same in all integrins.

4.1 Enhancing a continuum model with MD

Here, an idea was tested, which works by energy transfer between the molecular model and the continuum model. Simulating complete focal adhesion or even complete integrins by molecular dynamics is not yet possible due to a lack of three dimensional structures as well as computational resources. Hence, only the mechanical behavior of the $\alpha_2\beta_1$ I domain bound to tropocollagen and the bond between these two molecules is investigated.

4.1.1 The idea of the enhancement

To come back to the original idea of simulating the force transfer from tissue to cell, the connection between the tissue and the cell must be modeled. The tissue and cell are hereby described as continuum materials with appropriate material models, e.g. as described in the previous chapter for the cell. The connection between the cell and the tissue shall be modeled as a layer of finite elements, whereby some of these elements represent focal adhesions and other don't contribute to the connection. Elements, representing focal adhesions, should hereby have the same mechanical behavior as focal adhesions. In order to exhibit the same mechanical behavior the material model and material parameters for the model must be correct. To determine the correct material parameter for these elements, a molecular model of an I domain bound to tropocollagen is utilized as a first building block to describe mechanically a single integrin-ECM connection. As focal adhesions consist of many integrin-ECM connections, another step with multiplication of the properties of the single connection is necessary. Figure 1.1 visualizes the idea of this enhancement (right hand side of middle section of the figure).

To derive the continuum material description the basic idea is shown in Figure 4.1. The first step is that the element in the finite element is deformed. The deformation at the origin, given by the deformation gradient $\boldsymbol{F}_0$, is then applied to the molecule. The deformation of the element is in a fixed set of units chosen by the user, but the molecular system uses AKMA units. In order to transfer the continuum

deformation to real displacements, it is necessary to define characteristic directions, which are used to measure the length into this direction within the molecule. For the molecular structure 1DZI [50] from the Protein Data Bank [13] exist two meaningful directions. The direction along the main axis of the I domain, which represents the important bound between the I domain and the collagen, is the first characteristic direction (FCD). The direction along the collagen is the second characteristic direction (SCD). Measuring the length along these directions enables the computation of a displacement vector to deform the molecule. Before the deformation and after the deformation, the energy of the system is calculated and the difference is given back to the continuum model. The energy is then used to compute the material properties with the following assumption

$$\Delta \mathscr{U}^{\mathrm{M}} = \langle \mathscr{U} \rangle_n^{\mathrm{M}} - \langle \mathscr{U} \rangle_{n-1}^{\mathrm{M}} =: \Psi^{\mathrm{C}} \tag{4.1}$$

with $\langle \mathscr{U} \rangle_n^{\mathrm{M}}$ being the time average of the potential energy in the deformed state, and $n-1$ in the undeformed state and Ψ^{C} the Helmholtz Free energy of the material law of the Finite Element simulation. The superscript M and C represent the molecular model and the continuum model respectively.

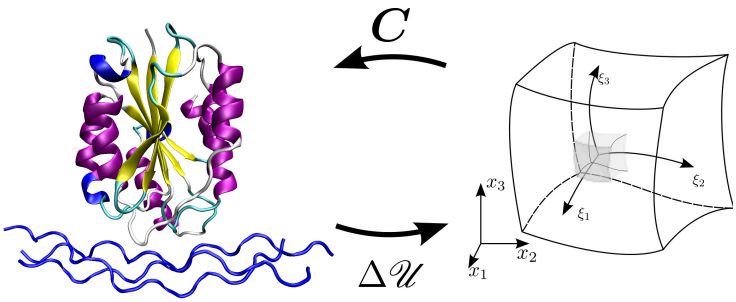

Figure 4.1: The basic idea to enhance a continuum model with molecular information. The deformation of the continuum element is applied to a molecular structure and the energy difference of the change is given back to the continuum model.

The basic assumption is that the energy which is released on the molecular side through a deformation impressed by the continuum equals

the same elastic energy consumed on the continuum side.

In general it would be sufficient to compute this energy only once and then use it as an input parameter for a material description. But there are some concerns regarding this. First, it will not only be a single energy value, which is computed. In case only the free energy of the bond is computed, it would be possible to get a spring constant of the bond, not the detailed stiffness in dependency of the distance between the binding partners. For that reason it makes sense to compute an energy change between the binding partners for different distances. This energy landscape is not the same for different unbinding paths. Figure 4.2 shall help to demonstrate this, showing the tropocollagen in red and the I domain in blue. Let's assume the tropocollagen is fixed with $\varphi_C = \theta_C = 0°$. Depending on the position of the integrin and the external stimulus, the vector $\boldsymbol{r}_I$ can be orientated in different directions with $\varphi_I \in [0°, 360°]$ and $\theta_I \in [0°, 180°]$. Once the I domain is pulled away, $|\boldsymbol{r}_I|$ increases. The absolute value of the vector $|\boldsymbol{r}_I|$ is defined as zero in the equilibrium position. Depending now on the orientation of $\boldsymbol{r}_I$, the energy landscape would look different as the connection between the I domain and the tropocollagen does not take place only in one bond. For different directions, different bonds would be released in different orders.

Besides the different orientations of the I domain, the tropocollagen can be differently orientated as well. By definition, the center of the coordinate system shall be placed in the α-carbon of the residuum, which is involved in the dominant bond to the I domain. The domain of definitions for the angles is then $\varphi_C \in [0°, 360°]$ and θ_C will be between $0°$ and approximately $30°$.

Due to the dependency of the energy landscape on the direction in which the I domain is pulled away from the tropocollagen, the deformation of the element is provided to the molecular model in every deformation step, which allows a tight connection between the deformation on the continuum part and the direction of pulling on the molecular part.

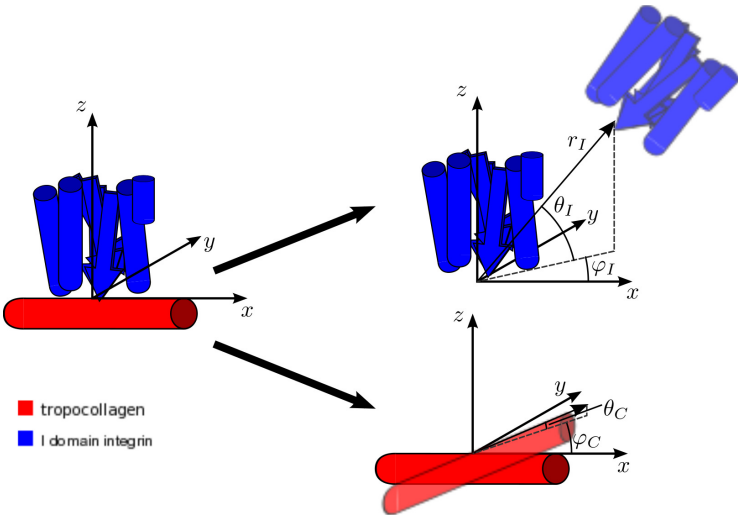

Figure 4.2: Possible orientations of tropocollagen (blue) and I domain (red) for the unbinding path.

FE	Calculation of the right Cauchy-Green tensor $\boldsymbol{C}$ at the origin of the element
	Calculation of stretches λ in the first (second) characteristic direction
	Calculation of displacement $\boldsymbol{u}^{\mathrm{M}}$ in the first (second) characteristic direction with the corresponding length of the protein
MD	Equilibration at undeformed configuration and calculation of the potential energy $\langle \mathscr{U} \rangle_{n-1}$
	Changing configuration based on deformations from FE by pulling on the protein
	Equilibration at deformed configuration and calculation of the potential energy $\langle \mathscr{U} \rangle_{n}$
	Calculation of energy difference $\Delta \mathscr{U} = \langle \mathscr{U} \rangle_{n} - \langle \mathscr{U} \rangle_{n-1}$

FE	Calculation of the material parameter c_1 based on the potential energy difference $\Delta\mathscr{U}$

Table 4.1: Computational steps on the FE and MD side

A brief overview of the computational steps is given in Table 4.1. In the following sections, these necessary steps taken on the continuum model and the molecular model are explained more in detail.

4.1.2 Computational steps on the continuum side

Starting from equation (1.24), the right Cauchy-Green deformation tensor $\boldsymbol{C}$ is provided to the molecular side and, based on the given energy, the second Piola-Kirchhoff stress $\boldsymbol{S}$ is computed in equation(4.2).

$$\int_{\omega} \boldsymbol{\sigma} : \delta\boldsymbol{e}\, d\omega = \frac{1}{2} \int_{\Omega} \underset{\boxed{\text{Molecular}}}{\overset{\longleftarrow}{\boldsymbol{S}}} : \delta\boldsymbol{C}\, d\Omega \tag{4.2}$$

The domain in the material space is denoted by Ω. The second Piola-Kirchhoff stress tensor $\boldsymbol{S}$ is the unknown in equation (1.24). The second Piola-Kirchhoff stress tensor $\boldsymbol{S}$ is hereby dependent on the molecular energy difference $\Delta\mathscr{U}^{\mathrm{M}}$, which is again dependent on the right Cauchy-Green deformation tensor $\boldsymbol{C}$:

$$\boldsymbol{S} = \boldsymbol{S}(\Delta\mathscr{U}^{\mathrm{M}}(\boldsymbol{C})) \tag{4.3}$$

As presented in Figure 4.1 the deformation is given to MD and the energy difference is used to compute the mechanical properties in FE. Because FE is in a fixed set of units chosen by the user and MD is in AKMA units, there is a transformation process needed to get everything together. The following paragraphs describe first the necessary steps to derive the appropriate deformation for MD, and then the retrieval of the energy difference and equations to calculate the mechanical properties.

Continuum computation before calling MD Using the deformation gradient $\boldsymbol{F}$ which is computed at the origin of the element, the

right Cauchy-Green tensor $\boldsymbol{C}$ can be computed following equation (1.6). The right Cauchy-Green tensor can be used for an eigenvalue computation with stretches $\tilde{\lambda}$ as the eigenvalues of the positive definite tensor as shown in equation (1.9). The first eigenvector will be the direction of $\boldsymbol{r}_I$ in Figure 4.2. Deriving the eigenvalues and eigenvectors of $\boldsymbol{C}$ is one possibility to achieve displacements which overlay with the characteristic directions in the molecule. Another possibility is to define a certain vector $\boldsymbol{a}$ from the beginning and compute with the help of $\boldsymbol{M} = \boldsymbol{C} \cdot (\boldsymbol{a} \otimes \boldsymbol{a})$ the corresponding strain λ_a for use in the molecular simulation. Depending on the molecular system, using one of these two possibilities or combinations of both might be appropriate.

Once the stretch λ is computed, the characteristic length l_{CD} of the protein in that direction is used to calculate the deformation of the protein.

$$\boldsymbol{u}^{\mathrm{M}} = l_{CD} \cdot (\lambda - 1) \cdot \hat{\boldsymbol{n}} \tag{4.4}$$

The molecular displacement $\boldsymbol{u}^{\mathrm{M}}$ is transferred to MD. The characteristic length l_{CD} can be the length in the direction of the first characteristic direction (FCD) or the second characteristic direction (SCD) and $\hat{\boldsymbol{n}}$ is the appropriate direction vector.

Continuum computation after MD finished Once the energy difference is computed in MD, the mechanical properties, specifically the second Piola-Kirchhof stress tensor $\boldsymbol{S}$ and the constitutive tensor $\mathbb{C}$, must be assigned. The constitutive tensor $\mathbb{C}$ itself, or the second Piola-Kirchhoff stresses $\boldsymbol{S}$, is computed with help of the strain energy or Helmholtz Free energy function Ψ [60], as given here

$$\boldsymbol{S} = 2\frac{\partial \Psi}{\partial \boldsymbol{C}} \tag{4.5}$$

$$\mathbb{C} = 4\frac{\partial^2 \Psi}{\partial \boldsymbol{C}^2} \tag{4.6}$$

with $\boldsymbol{C}$ the right Cauchy Green tensor and $\mathbb{C}$ the elastic stiffness tensor.

For the Helmholtz Free energy function the Neo-Hookean model with a linear relation between energy and deformation invariants has been chosen.

$$\Psi = c_1(\frac{I_1}{I_3^{-\frac{1}{3}}} - 1) \tag{4.7}$$

Here $I_1 = \mathrm{tr}(\boldsymbol{C})$ denotes the first invariant and $I_3 = \det(\boldsymbol{C})$ the third invariant. Following equation (4.1), the computed energy from the molecular model is equal to the Helmholtz Free energy. With this relation, the material parameter c_1 of equation (4.7) can be computed in the following way:

$$c_1 = s \cdot \frac{4.184}{N_A} \cdot \frac{1}{V} \cdot \frac{1}{\frac{I_1}{I_3^{-\frac{1}{3}}} - 1} \cdot \Delta U \tag{4.8}$$

with s being a scaling factor to achieve the appropriate units in FE, N_A the Avogadro constant, V the volume of the element, I_1 and I_3 the first and third invariants, and ΔU the energy difference. The scaling factors are necessary because MD uses the AKMA unit system, i.e. Angstroms, Kilocalories/Mole, Atomic mass units, while FE has its user chosen units.

4.1.3 Computational steps on the molecular side

In equation (4.1), the potential energy $\mathscr{U}$ of the present and past molecular configuration is needed. To compute the energies, atomistic simulations of the protein are carried out and the time average of the potential energies is computed at different configurations.

When the molecular part receives the deformation information of the continuum part, the displacement of certain atoms is realized with a harmonic potential u_{harm} as defined and available in CHARMM [19]. The selection of the atoms, on which the potential is applied, and the force constant k depends on the problem.

$$u_{harm} = \sum_i k_i * (\boldsymbol{x}_i^{\mathrm{M}} - \boldsymbol{x}_{ref}^{\mathrm{M}})^n \tag{4.9}$$

The harmonic potential u_{harm} is defined by the force constant k_i, the current coordinates $\boldsymbol{x}_i^{\mathrm{M}}$ and the reference coordinates $\boldsymbol{x}_{ref}^{\mathrm{M}}$, and exponent n which is generally chosen as $n = 2$.

The computation of the energy in the original and the deformed configuration is performed by subsequently computing the interaction energy E_{int} or the potential energy $\mathscr{U}$ for every stored configuration. The average potential energy over all energies for every configuration is returned to the continuum part. Kinetic energy is neglected.

Using the Lennard-Jones potential as a simplified example of an energy-distance relation of the interaction of two atoms, the derivation of the energy difference shall be explained.

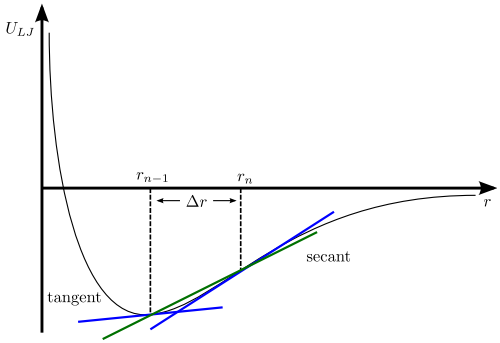

Figure 4.3: Schematic, one dimensional Lennard-Jones potential U_{LJ} (black) with blue lines as the tangents at r_{n-1} and r_n and the green line the secant between r_{n-1} and r_n

.

The computation of force within MD is usually performed by differentiating potential U with respect to the distance vector $\boldsymbol{r}$. In Figure 4.3 the derivative is shown by the tangent at two evaluation points r_{n-1} and r_n. In the case of coupling, the secant between these two evaluated points is used (green line between r_{n-1} and r_n in Figure 4.3). In case of $\Delta r \rightarrow 0$, both results coincide. Equation (4.10) gives the mathematical description:

$$\lim_{\Delta \boldsymbol{r} \to 0} \frac{\Delta U_{LJ}}{\Delta \boldsymbol{r}} = \lim_{\boldsymbol{r}_n \to \boldsymbol{r}_{n-1}} \frac{U_{LJ}(\boldsymbol{r}_n) - U_{LJ}(\boldsymbol{r}_{n-1})}{\boldsymbol{r}_n - \boldsymbol{r}_{n-1}} = \nabla U(\boldsymbol{r}) \tag{4.10}$$

with U_{LJ} being the Lennard-Jones potential and $\boldsymbol{r}$ the vector between two atoms.

Energy difference: current difference method The example in Figure 4.3 shows the computation of the energy between r_{n+1} and r_n. In the current difference method, the positions r_{n+1} and r_n of the earlier given example are related to the continuum timestep t^{C} in the following way:

$$\begin{aligned} \boldsymbol{r}^{\mathrm{M}}(t^{\mathrm{C}}) &= \boldsymbol{x}_j^{\mathrm{M}}(t^{\mathrm{C}}) - \boldsymbol{x}_i^{\mathrm{M}}(t^{\mathrm{C}}) && \text{(4.11a)} \\ \boldsymbol{r}_n &= \boldsymbol{r}^{\mathrm{M}}(t_n^{\mathrm{C}}) && \text{(4.11b)} \\ \boldsymbol{r}_{n-1} &= \boldsymbol{r}^{\mathrm{M}}(t_{n-1}^{\mathrm{C}}) && \text{(4.11c)} \end{aligned}$$

The molecular energy difference ΔU^M is computed between the molecular configuration at continuum timestep t_n^C and t_{n-1}^C. The secant of these two timesteps is very close to the tangent. Consequently, forces computed by FE should be in the same magnitude as internal molecular forces.

Energy difference: storage method Another interpretation of the energy difference is to define a molecular reference configuration $\boldsymbol{x}_{ref}^{\mathrm{M}}$. This reference configuration can be either the configuration at the continuum timestep $t_0 = 0$ or at the timestep $t_0 = t_{U_{min}}$, where the potential energy U is minimal. Looking back at the before mentioned example with the Lennard-Jones potential, the positions r_{n+1} and r_n relate to the following continuum timesteps t^{C}:

$$\begin{aligned} \boldsymbol{r}^{\mathrm{M}}(t^{\mathrm{C}}) &= \boldsymbol{x}_j^{\mathrm{M}}(t^{\mathrm{C}}) - \boldsymbol{x}_i^{\mathrm{M}}(t^{\mathrm{C}}) && \text{(4.12a)} \\ \boldsymbol{r}_n &= \boldsymbol{r}^{\mathrm{M}}(t_n^{\mathrm{C}}) && \text{(4.12b)} \\ \boldsymbol{r}_{n-1} &= \boldsymbol{r}^{\mathrm{M}}(t_0^{\mathrm{C}}) && \text{(4.12c)} \end{aligned}$$

The storage method allows the element to store the complete energy from the beginning of the simulation to the current continuum timestep t_n^{C}, unlike the current difference method. The molecular energy difference ΔU^{M} is consequently computed from:

$$\Delta U^{\mathrm{M}} = \langle U \rangle_n^{\mathrm{M}} - \langle U \rangle_{n_0}^{\mathrm{M}} =: \Psi^{\mathrm{C}} \tag{4.13}$$

with $\langle U \rangle_{n_0}^{\mathrm{M}}$ being the molecular energy at the reference configuration or the minimum energy.

4.2 The water dimer – a well-documented validation example

A simple model is used to study the idea to enhance the FE material description with molecular information. The criteria for selecting this model has been such that the computational time is in an acceptable range, the thermal energy cannot be neglected, and the results can be compared to published results. The water dimer (Fig. 4.4) fulfills all these requirements. It consists of two H_2O molecules. The model also allows to study the influence of implicit water models compared to explicit models or vacuum.

Figure 4.4: Water dimer. Oxygen is red and hydrogen is white.

The water dimer is a common problem for testing and comparing quantum-mechanical theories. The literature therefore offers several solutions regarding energy levels of the system [20, 73]. Though the quantum-mechanical treatment will be more accurate than the point-wise treatment of the electrical charge used here, the results should be of the same magnitude. Additionally, the water-dimer problem is studied in terms of hydrogen bonding [118]. So, structural configurations and hydrogen bonding in the equilibrium configuration can be compared to published results. The equilibrium configuration will give additional insight in possible binding energies and forces between the water molecules. As an interesting side-comment, the water dimer was once called “a theoretical guinea pig” [73].

4.2.1 Model setup

The first principal direction of the system is the vector between the oxygen atoms. The deformation of the element is translated in an increasing distance between the oxygen atoms. The distance between the two oxygen atoms is only about 3 Å. Even small differences in the placement of the oxygen atoms play a vital role.

Oxygen positioning The positioning of the moving atom plays an important role as the distance between the two oxygen atoms is mainly responsible for the energy and forces between the two water molecules. Therefore, the distance between the oxygen atoms should follow the FE strain as closely as possible to yield an accurate result. For the water dimer, the system has been divided into one static water molecule and one moving water molecule. The distance change between the two molecules takes place in the following steps:

I. Pre-configuration:	
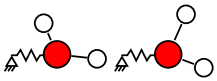	Restraining the static (left) and the moving (right) molecule with harmonic potentials. The boundary condition of the static one remains during the complete simulation. Equilibration of the system.
II. Configurational perturbation:	
	Computing the new reference position $\boldsymbol{x}^{\mathrm{M}}_{ref}$, applying boundary conditions to force the moving molecule into the reference position $\boldsymbol{x}^{\mathrm{M}}_{ref}$ with a dynamic simulation.
III. Post-configuration:	
	Equilibrating the molecule in the new position and computing the time average of the potential energy. Moving on to step II and consequently repeating step II and step III for every deformation of the finite element.

Table 4.2: Steps to compute the energy difference between two configurations.

In general, one water molecule is restrained while the other molecule is translated in $\boldsymbol{x}$-direction. The fixation of the water molecules was enabled by applying harmonic constraints following equation (4.9). The main parameter of the harmonic potential is the force constant k, which is comparable with a spring constant. The overall approach can be considered a displacement-controlled elongation in terms of structural analysis. The current interaction force is hereby deduced.

Pre-configuration There is another important consideration before moving the atom: Which coordinates should be used as the current coordinates? In general, the last configuration after the equilibration is readily available and can be used as a starting configuration to compute the displacement. However, the position might be too far from the reference position in this particular timestep. This can be remedied by implementing the computation of the average position $\langle \boldsymbol{x}^{\mathrm{M}} \rangle$ of selected atoms for the length of the last simulation. To achieve the averaging, the current coordinates of the system are preserved for the next dynamics run, while a comparison coordinate set is overwritten with the average positions. All subsequent calculations for the new position are done using the comparison coordinate set.

Configurational change One water molecule is moved while the other is kept fixed. The movement of the water molecule can be done in different ways. Here, two solutions have been implemented: First, the straightforward approach translates the water molecule along the displacement vector $\boldsymbol{u}^{\mathrm{C}}$ provided by the FE model. The second approach uses the center of mass of selected atoms and binds this center of mass to a reference position $\boldsymbol{x}^{\mathrm{M}}_{ref}$ with a harmonic potential.

Equilibration and analysis The water dimer was equilibrated at the pre-configuration and post-configuration (Table 4.2) for $t^{\mathrm{M}}_{equ} =$

100, 200, 400 and 800 ps. Three different cases for the water treatment were simulated: vacuum, implicit, and explicit water. For the equilibration the explicit Leapfrog-Verlet time integrator with a timestep of $\Delta t^{\mathrm{M}} = 0.1\ fs$ was used. The temperature of the simulation was set to $T = 298.0\ K$ and controlled by a thermostat with upper and lower boundaries of $\pm\ 10\ K$.

The configurational change (step II in Table 4.2) was simulated for the same time span as for the equilibration. Parameters for the simulations were the same as for equilibration.

Forces In order to compare the interaction forces F_{int} between the two water molecules on the molecular model and the Finite Element model, a finite difference scheme is used to compute the forces with the help of the interaction energy E_{int} between the two water molecules.

$$F_{diff} = \frac{\langle E \rangle_{int}^{n} - \langle E \rangle_{int}^{n-1}}{|\boldsymbol{x}^{\mathrm{M},n} - \boldsymbol{x}^{\mathrm{M},n-1}|} \tag{4.14}$$

Hereby, $\langle E \rangle_{int}^{n-1}$ denotes the time average of the interaction energy of the pre-configuration, $\langle E \rangle_{int}^{n}$ the time average of the interaction energy of the post-configuration, $\boldsymbol{x}^{\mathrm{M},n-1}$ the position of the moving oxygen at the pre-configuration and $\boldsymbol{x}^{\mathrm{M},n}$ at the post-configuration.

Finite Element model The Finite Element part of the model consists of a hexahedral element with linear basis functions. In order to avoid volumetric locking, Enhanced Assumed Strains are used. The directional vector between the oxygen atoms is aligned with the $\boldsymbol{x}^{\mathrm{C}}$-direction of the element. The element is stretched into $\boldsymbol{x}^{\mathrm{C}}$-direction by Dirichlet boundary conditions. The simulation is a unidirectional pull. The material model is the Neo-Hookean material model presented in equation (4.7).

Molecular Dynamics model - Water dimer preparation The water dimer was built from scratch with coordinates reflecting the most stable configuration. The force field is CHARMM 22 [89], and the residuum for the water molecules is the standard *TIP3* water model. Energy potential parameters are 8.0 Å for the non-bonded cut-off and

7.0 Å for the switch to the smoothing function. All other non-bonded parameters are standard values. The checking frequency for hydrogen bonds is 50, and 4.5 Å was chosen for the cut-off distance.

Unlike standard molecular dynamics simulations, which generally restrict the fluctuations of hydrogen atoms, the "artificial" bond between the two hydrogen atoms (Figure 4.4) was not restricted in our work. As a direct consequence, the standard molecular timestep of $\Delta t^{\mathrm{M}} = 1\ fs$ must be reduced to cover hydrogen vibrations. The general timescale for this vibration is in the range of half a femtosecond. During preparation the used timestep was $\Delta t^{\mathrm{M}} = 0.5\ fs$, while for analysis runs the timestep was further decreased to $\Delta t^{\mathrm{M}} = 0.1\ fs$ in order to properly resolve hydrogen vibrations.

After reading the coordinates and the force field into CHARMM [19], the water dimer is minimized. First, minimization is done by a steepest descent (SD) strategy for 100 steps. Further minimization is carried out by the Adopted Basis Newton-Raphson method, a mixture between SD and Newton-Raphson [30].

Following the minimization, the structure was slowly heated to 298.0 Kelvin during 1.0×10^5 timesteps. Equilibration lasted for 1.1×10^6 timesteps at 298.0 K. Due to the reduced timestep, heating time t_{heat} was 20 ps and equilibration time t_{equi} was 100 ps respectively.

The implicit solvent model ACE2 [23, 117] was chosen for the water dimer. The internal and solvent dielectric constants were both 80.0 $F\ m^{-1}$. The width parameter for the Gaussian density function was 1.3, and the hydrophobic contribution to the potential was zero as both the internal structure and the solvent consist of water.

The explicit water dimer model consists of a water box with 25 Å in $\boldsymbol{x}^{\mathrm{M}}$-direction and 20 Å in $\boldsymbol{y}^{\mathrm{M}}$- and $\boldsymbol{z}^{\mathrm{M}}$-direction. The water molecule for the explicit solvent was TIP3 with restraint hydrogen fluctuations. Periodic boundary conditions have been used at the edges of the water box. A total of 1080 water atoms are inside the box. Movement of the water molecules of interest was restricted in $\boldsymbol{y}^{\mathrm{M}}$- and $\boldsymbol{z}^{\mathrm{M}}$-direction to ensure a bond between them during equilibration.

4.2.2 Computational results

The water dimer was simulated using three different treatments of surrounding water:

1. vacuum
2. implicitly with analytical continuum solvent
3. explicitly

The following sections show and discuss the different results for preparation, coupling, and the comparison of FE and MD.

Preparation To validate the model, geometric configurations and interaction energy data after equilibration are compared to published data [106, 41, 124, 36]. The results are listed in Table 4.3. The important geometric value is the oxygen distance R_{OO}. The results in vacuum and with explicit water are slightly lower than published results. The recommended experimental result is $R_{OO} = 2.95$ Å (experimentally $R_{OO} = 2.976$ Å; corrected due to effects of anharmonicity). *Ab initio* calculations with a quantum-mechanical treatment of the electrostatic interactions found $R_{OO} = 2.90 - 2.92$ Å. In our study, the closest result was that in a vacuum. Here the O-O distance was found to be $R_{OO} = 2.85$ Å. The result was slightly lower for explicit treatment of water, with $R_{OO} = 2.82$ Å. The smaller values arise from the classical treatment of electrostatic charges. The implicit treatment of water resulted in an increased distance between the oxygen atoms. R_{OO} was found to be $R_{OO} = 3.72$. The additional energy terms of the implicit water model caused the two oxygen atoms to further separate from each other. It should be noted that the implicit and explicit results cannot be easily compared to the published data as *ab initio* simulations are generally carried out in vacuum.

Another suitable result for comparison is the interaction energy E_{int}. Here, the published data ranges from $E_{int} = -3.64\ kcal\ mol^{-1}$ to $E_{int} = -4.90\ kcal\ mol^{-1}$ [124]. In general, it can be observed that, without correction terms to account for quantum-mechanical effects,

the experimentally suggested value of $E_{int} = -5.4 \pm 0.7\ kcal\ mol^{-1}$ [36] cannot be achieved. The energy results (Table 4.3) from our model are for the vacuum case, $E_{int} = -5.19\ kcal\ mol^{-1}$, and $E_{int} = -4.62\ kcal\ mol^{-1}$ for the explicit treatment. The values are thus in the range of the published results, though they are not as exact as *ab initio* results. The result from the explicit water is interesting because the lower energy cannot be caused by the geometry. The O-O distance R_{OO} of the explicit result is lower as compared to the vacuum.

The interaction energy E_{int} of the implicit results is substantially lower than the other results, with a value of $E_{int} = -1.68\ kcal\ mol^{-1}$. This is linked to the increased distance between the water molecules as well as to the screening effect of the ACE2 implicit water model.

	R_{OO} [Å]	E_{int} [$kcal\ mol^{-1}$]
vacuum	2.85	−5.19010
implicit	3.72	−1.67983
explicit	2.82	−4.61679
Literature	2.95 [106, 41], 2.925 [124], 2.913 [151]	-5.4 ± 0.7 [36], -4.90 ± 0.02 [124]

Table 4.3: Geometric and interaction energy results.

Different structural configurations which were observed between the two water molecules were compared to published results by Diercksen [45] and Scheiner [118] as another validation of the model. Figure 4.5 shows the results for all three cases: vacuum, implicit and explicit treatment. The configurations are drawn above the result bars in Figure 4.3. As found by Diercksen [45], the most prominent configuration is the linear configuration, either in the *trans* state or in the *cis* state. The findings of Diercksen are in accordance with our results, especially for the vacuum case. The second most likely configuration is the cyclic configuration with two H-bonds, which is occasionally achieved for the vacuum case and more favorable for the implicit case. The bifurcated

configuration was rarely observed. The upper right graphs of Figure 4.5 show the timeline of the configurations during equilibration. For the vacuum, the water dimer remains very stable in the linear configuration and nearly constantly retains an H-bond. That is in contrast to the implicit case, where the configuration switches frequently between linear and cyclic configuration. The published data allows no evaluation of the stability, only of the frequency of occurrence. Here our results are in good agreement with published results.

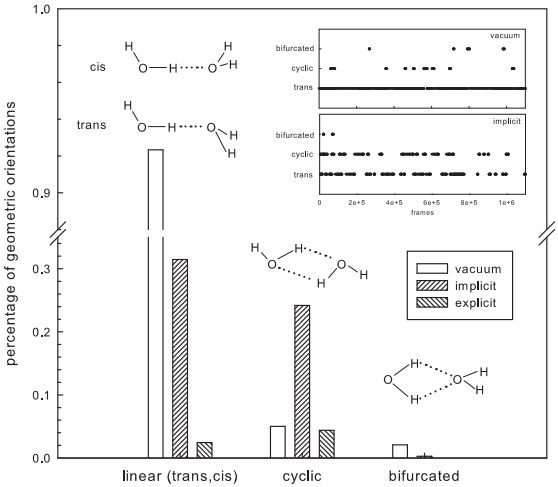

Figure 4.5: Analyzed equilibration configurations [118] of the water dimer for vacuum, implicit (ACE2) and explicit water. The upper right quadrant shows the timeline of these configurations.

For the explicit treatment, the occurrence of H-bonds was much lower than for the other two cases. During equilibration there is hardly an H-bond at all. In general, it was difficult to ensure a stable bond between the two water molecules. Though the complete water box was equilibrated, the energy of the two water molecules of interest was

not. Because the surrounding water has the same mass as the observed water, the two molecules were constantly pushed away from each other. As expected from published results [158] they frequently developed H-bonds to their surrounding counterparts but no stable bond to the opposed binding partner. This resulted in the much lower number of H-bonds.

Configurational changes - distance between $(H_2O)_2$ Table 4.2 shows the different steps on the molecular scale for every FE configuration. The distance between both molecules plays the most important part for the energy calculation. This is especially important for the water dimer problem, because, due to the limited number of atoms, the interaction energy E_{int} is dominated by the O-O distance R_{OO}. In order to achieve a correct Finite Element result, the Finite Element stretch λ must be in perfect sync with the molecular distance R_{OO}.

Figure 4.6 shows the oxygen distance R_{OO}, starting at the reference configuration and ending at the final position after 10 continuum displacement steps for different force constants k (equation (4.9)). The distance is stepwise increased hereby for every step by 0.6 Å. The theoretical average shows the expected distance. In general, it can be observed that, for larger force constants k, the result is closer to the expected distance. For forces smaller than $k = 6pN$, no sufficient restriction to the new position was achieved. This was found for both methods: by translating the water molecule along $\boldsymbol{u}^{\mathrm{C}}$ and by restricting the center of gravity to the new position $\boldsymbol{x}^{\mathrm{M}}_{ref}$. The small deviation from the theoretical value observed by the latter method can be explained by the fact that the center of gravity was restricted to x^{M}_{ref} and not the oxygen atom. But the distance R_{OO} was measured between the two oxygen atoms. Though the oxygen atom is heavy compared to the hydrogen atoms, the center of gravity will be slightly different than the position of the oxygen atom itself.

The variance can be divided into two errors which accumulate:

- error while updating from $\boldsymbol{x}^{\mathrm{M},n-1}$ to $\boldsymbol{x}^{\mathrm{M},n}$
- high fluctuations

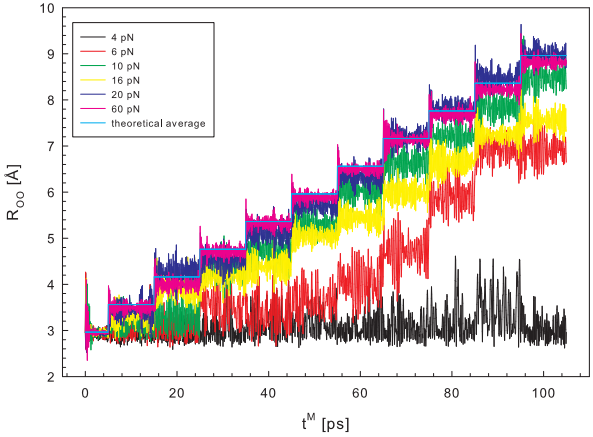

(a) translation

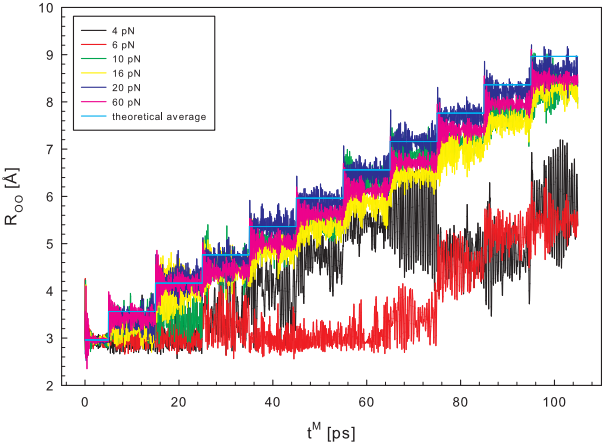

(b) displacement vector

Figure 4.6: Time - oxygen distance results for using the last oxygen position before translating the atom in $\boldsymbol{x}$-direction (a) or to restrict the center of gravity of the moving molecule to the new position (b) depending on k.

The first error is critical because if the distance change R_{OO} is not properly achieved for every displacement step, the error grows eventually over time. The second error depends on the harmonic potential and will eventually improve for longer equilibration times due to improved statistics.

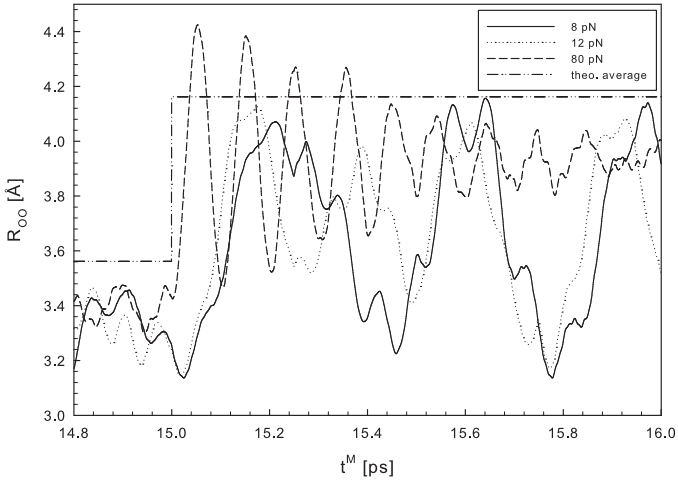

Figure 4.7: Close-up of a distance change R_{OO}^{n-1} to R_{OO}^{n}.

To understand the first error better, the distance jump from R_{OO}^{n-1} to R_{OO}^{n}, with n being the post-configuration step and $n-1$ the pre-configuration step, was investigated more closely. Figure 4.6 shows the results for different force constants k of the harmonic potential U (equation (4.9)). It can be observed that for a higher force constant k the distance change happens more rapidly. Even for a small force constant the distance increase is reasonably fast. However, the results also make clear that the theoretical value was never fully achieved. There is a constant error between the measured and theoretical average. One of the reasons is the calculation of the current position. The current position $\boldsymbol{x}^{\mathrm{M}}$ of the oxygen atom will have in most cases an offset to the average position $\langle \boldsymbol{x} \rangle^{\mathrm{M}}$. To start the translation at the current position

leads to a new position which does not equal the computed position from the Finite Element model. In order to achieve the theoretical value, it would be necessary to compute a correction term. The new position can be then computed by the following form:

$$\boldsymbol{x}^{\mathrm{M},n} = \boldsymbol{x}^{\mathrm{M},n-1} + \underbrace{\left(\langle \boldsymbol{x} \rangle^{\mathrm{M},n-1} - \boldsymbol{x}^{\mathrm{M},n-1}\right)}_{\text{correction term}} + \boldsymbol{u}^{\mathrm{C},n} \tag{4.15}$$

Here, $\boldsymbol{x}^{\mathrm{M}}$ denotes the position of the moving oxygen atom and $\boldsymbol{u}^{\mathrm{C}}$ the computed displacement vector from the FE model. Figure 4.8 shows the results for using the average position as a basis for computing the new position. The oxygen distance R_{OO} is now closer to the theoretical value, and there is a clear improvement of the solution for higher force constants k.

The second problem is high fluctuations of the oxygen atom around the theoretical value. The reason for the fluctuations was partly the formulation of the harmonic potential U in equation (4.9). The change of R_{OO} is smaller than 1 Å, the harmonic potential is not the optimal formulation. The small graph in Figure 4.9 shows a plot of U for different exponents n. For higher exponents n, the inclination of the curve and therefore the resulting force, is shifted to the right. The oxygen atom thus feels less force at small deviations from the theoretical value. The force is substantially increased only at larger deviations. But using an exponent of $n = 1$ results in a constant force independent of the variation $\boldsymbol{x} - \boldsymbol{x}_0$. The curves for R_{OO} against time in Figure 4.9 support this conclusion. Decreasing exponent n, the fluctuation around the theoretical value decreases.

Finally, the quality of the positioning of the moving oxygen was quantified for all previously tested measures. Figure 4.10 shows the deviation of the time-average distance $\langle R_{OO} \rangle$ from the theoretical value, determined from FE. The simulation uses the average position $\langle \boldsymbol{x}^{\mathrm{M}} \rangle$ as a basis for computing the new position, and the exponent $n = 1$ for U (equation (4.9)) was used. The deviation is almost zero for most distances. At the beginning, when intermolecular forces are still high, the position deviation is at most 8×10^{-3} Å, which is less than 1 % deviation from the theoretical position. At the end, it can be observed

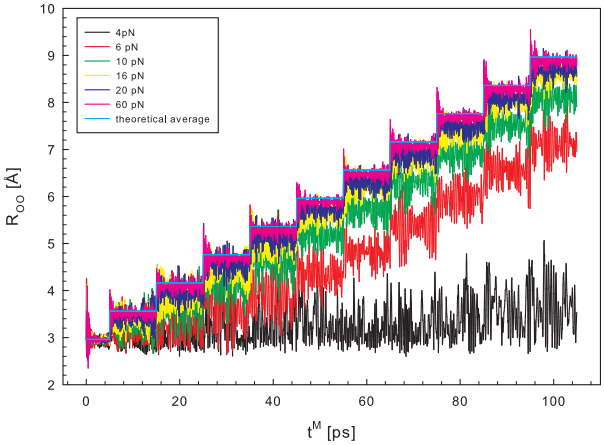

(a) translation

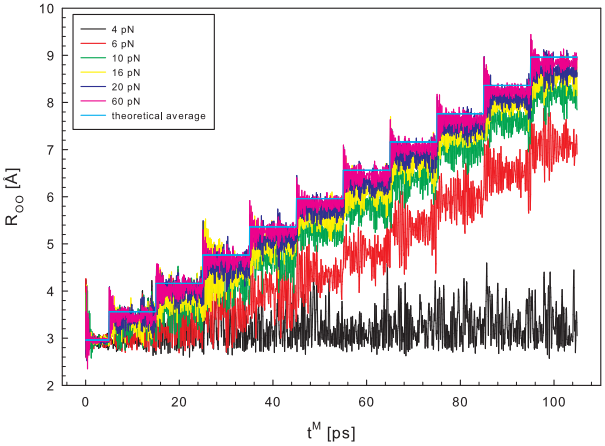

(b) displacement vector

Figure 4.8: Time - oxygen distance results for using the average oxygen position before translating the atom in $\boldsymbol{x}$-direction (a) or to restrict the center of gravity of the moving molecule to the new position (b) depending on k.

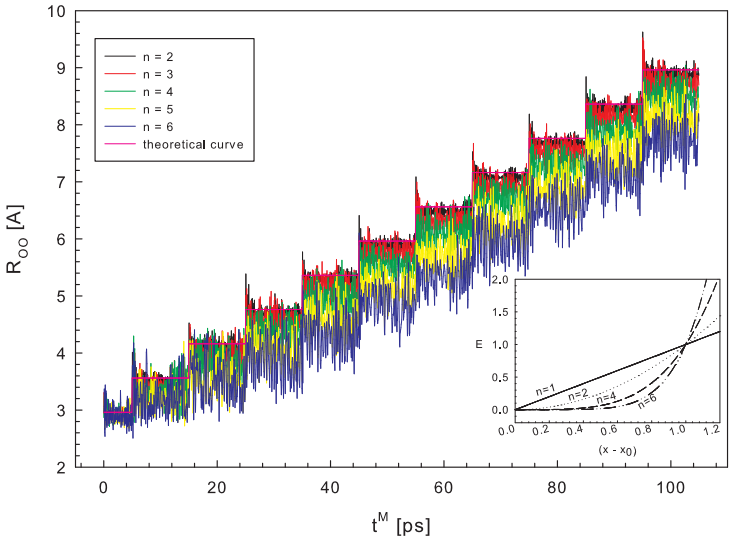

Figure 4.9: R_{OO} for different exponents n in equation (4.9). Small graph shows a plot of equation (4.9) for different exponents n.

that the oxygen is not attracted, but rejected. Because these simulations have been done in vacuum, there is a small repulsion force before the bond is finally dissolved. Therefore, the moving oxygen atom is pushed in the opposite direction.

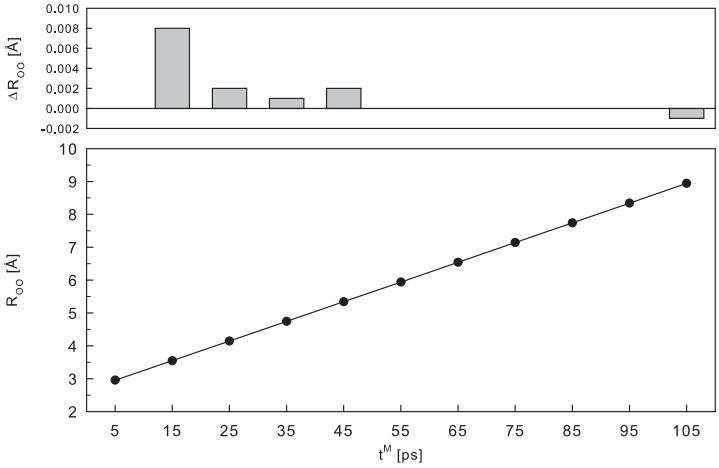

Figure 4.10: Average R_{OO} over time (lower graph) and deviation from the theoretical value (upper graph).

At the end, differences between the translation of atoms directly and of their center of gravity are discussed. The difference for the water dimer is insignificant because of the low number of atoms in the system, but it has implications for the integrin. The advantage of the first method is that it is straightforward, using the FE data and applying it to the molecular system. Depending on the system, it can impose inacceptable boundary conditions on the molecular system. This is especially true for systems, where not a single atom but groups of atoms are translated. Defining several atoms as moving atoms will result in the chosen atoms essentially keeping their original equilibrated

configuration over time. This might not be appropriate. In order to avoid this behavior, there are two possibilities. One is to use a "ghost" atom and pull on that atom. Here, all non-bonded interactions with nearby atoms are taken into account. This is a similar strategy as used in Steered Molecular Dyamics. Another possibility is to transpose the center of gravity of these atoms. This allows the configuration of the selected atoms to change over time and to contribute to the energy difference. The second approach was used for the water and the integrin system.

Forces and stresses The molecular forces between two water molecules were analyzed and compared with the FE generated forces to verify the molecular enhancement. To acquire more knowledge about necessary equilibration times, the most efficient computational system was computed for different equilibration times (Table 4.4). The molecular timestep size of $\Delta t^{\mathrm{M}} = 0.1\ fs$ causes smaller equilibration times, but does not affect the number of analyzed configurations; e.g., for a equilibration time of $t^{\mathrm{M}}_{equi} = 0.1\ ns$, 10^6 configurations are analyzed. Only every second configuration is analyzed to save computational time. Hence, the number of configurations, used for computing intramolecular forces as well as energies was 5×10^5 for $t^{\mathrm{M}}_{equi} = 0.1\ ns$, 1×10^6 for $t^{\mathrm{M}}_{equi} = 0.2\ ns$, 2×10^6 for $t^{\mathrm{M}}_{equi} = 0.4\ ns$ and 4×10^6 for $t^{\mathrm{M}}_{equi} = 0.8\ ns$. This would correspond to equilibration times of $t^{\mathrm{M}}_{equi} = 1.0$ to $8.0\ ns$ with the standard molecular timestep size of $\Delta t = 1\ fs$.

Table 4.4 shows different interaction energies E_{int} for the equilibrated oxygen distance R_{OO}. The energy values decrease for longer equilibration times, but there is no convergence noticeable. There might be two reasons for that behavior. The first reason might be the problem to keep the system equilibrated over a picosecond time span. There will always be sudden energy jumps in the range of $E_{HB} \approx 18 kcal\ mol^{-1}$ [158] due to the nature of the hydrogen bond. In the process of keeping the total energy E of the system constant, the velocity is increased or decreased accordingly. Afterwards the system requires some time to relax itself and to become stable before the next change of hydrogen bonding causes another temperature change and so on. The second reason might be in the time integration. Through the Leapfrog al-

gorithm a linear energy increase is introduced to the system over time. In general, the system of a simple water dimer is statistically difficult to treat. On the other hand, equilibration was achieved easily for the explicit water system, taking the waterbox into account, as expected.

t_{equi}^{M} $[ns]$	E_{int} [kcal/mol]
0.1	-4.71401
0.2	-4.80179
0.4	-4.87136
0.8	-5.19010

Table 4.4: Interaction energies E_{int} in dependency of the equilibration time t_{equi}^{M}.

But for the purpose of validating the coupling algorithm, the equilibration is not the dominant factor, but should be kept in mind when interpreting the results. The reason is that the same trajectories are analyzed for the interaction energy E_{int} and the interaction force F_{int}. Consequently, both must be in the same range independent of the simulation. The results for the three different treatments of water (vacuum, implicit and explicit) are shown in Figure 4.11, Figure 4.12, and Figure 4.13, respectively.

The graph in Figure 4.11 shows different results, which are combined to give an overview of important result data. First of all, the left axis shows the interaction energy E_{int} in dependency of the distance change ΔR_{OO} of the two oxygen atoms following equilibration. The interaction energy decreases for increasing distance, as expected, because the energy is mainly driven by the distance and hydrogen bonds, which are also dependent on the distance. It shall be mentioned that due to the statistically insufficient number of atoms, the enthalpy H of the water dimer system is not constant. For this reason, the interaction energy E_{int} does not equal the free energy of the bond. Even

for bulk water the discussion is ongoing if the enthalpy is conserved or not. From computational studies it was found that it is justifiable to speak from an "intact" and "broken" state of an H-bond and that the difference in enthalpy for an H-bond is $\Delta H = 1.9\ kcal/mol$ [126]. Due to the strong decrease in energy (Figure 4.11) at the beginning, it appears that the starting distance R_{OO} was slightly off the optimal equilibration distance, or the distance steps were too wide to catch the small energy change at the beginning.

The force results are shown in Figure 4.11 as blue lines. The right axis shows forces in pN. Negative results are molecular and positive forces are continuum based due to definition. MD forces are obtained directly by analyzing trajectories. The very same trajectories, used for the energy computation, are analyzed to compute the mean interaction force over time. All computations are based on the same force field. The force decreases with a maximum of $F_{int} = -4.87\ pN$ to $F_{int} = -5.0 \times 10^{-2}\ pN$. In general, the decline in force follows the decline in energy. As a comparison to the direct approach of obtaining intermolecular forces, equation (4.14) is used to compute the force F_{diff}. In comparison to F_{int}, F_{diff} is slightly lower at the beginning, but in the same force range. The small difference at the beginning is because F_{int} represents the tangent on the energy curve while F_{diff} represents the secant between two distances ΔR_{OO} of the same energy curve. Therefore, results won't be exactly the same. In addition, F_{diff} reacts more sensitively to energy changes than the mean force F_{int}. The continuum force F^{C} from FE is absolutely identical with F_{diff}, which should be the case as the computation of the material properties in FE is essentially a finite difference approach. Figure 4.11 shows that the coupling algorithm is producing the same results as molecular dynamics simulations.

For a comparison of different water models with the vacuum solution, the same system was simulated with ACE2 [23, 116]. Figure 4.12 shows the results for the water dimer. The energies E_{int} are substantially lower than the energies of the water dimer in a vacuum. Reasons for the reduced energy are the increased oxygen distance R_{OO} for the implicit model (Table 4.3) and the additional screening of electrostatic forces. Beside lower energies E_{int}, the energy gradient is larger. In the vacuum case, a distance of up to $\Delta R_{OO} = 2.85$ Å was simulated

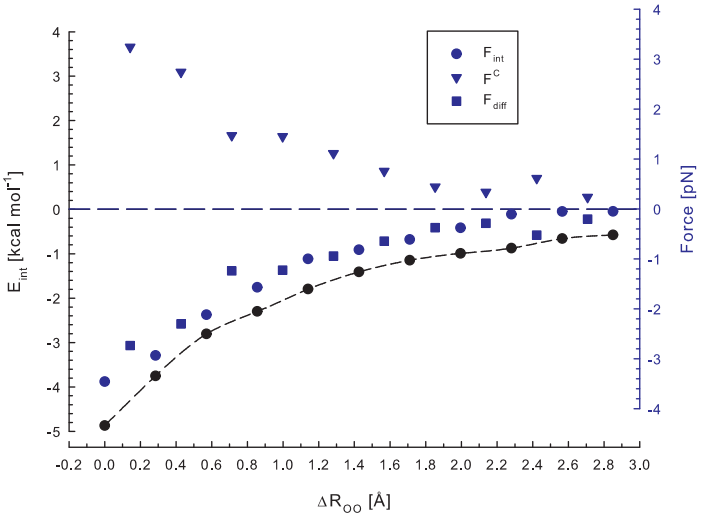

Figure 4.11: Interaction energy E_{int}, intermolecular forces F_{int}, computed forces F_{diff} and forces from Finite Element F^c for the water dimer in vacuum in dependency of the distant change ΔR_{OO}.

to achieve unbinding. Here, only half of the distance was necessary ($\Delta R_{OO} = 1.48$ Å). Unlike in the vacuum case, the energy is positive. This is because of the implicit water model. The ACE2 model includes a hydrophobic contribution, which depends on the surface. For the proposed standard value of $\sigma = 3.0$, the hydrophobic contribution of the model equals roughly the solvent accessible surface multiplied by 8 $cal/(mol$ Å$^2)$ for peptides of 10-12 residues. But in terms of the water dimer, it can be expected that there is a hydrophilic rather than a hydrophobic contribution as compared to bulk water [125]. Because no value for σ is available from the literature for this kind of problem, $\sigma = 0.0$ was chosen. The contribution of sigma to the total energy is constant and independent from the oxygen distance R_{OO}. Therefore, the difference in energy ΔE_{int} is not dependent on σ. The energy difference with the implicit water model was $\Delta E_{int} = 0.143\ kcal/mol$. This is smaller than results found by Silverstein et al. [126] in a simplified two-dimensional model. They found a free energy value of $\Delta G = 0.480\ kcal/mol$ using Monte-Carlo simulations.

Lower forces are linked to lower energy differences. The maximum interaction force was $F_{int} = -0.13\ pN$ and was achieved at $\Delta R_{OO} = 0.37$ Å. Looking at the energy curve together with the force result, it becomes clear that the two water molecules are very near their ideal equilibration point. The energy curve increases slightly at the beginning, steeper in the middle, and smaller at the end again. The force curve follows the course of the energy, with small forces at the beginning and larger forces in the middle. The directly computed force F_{diff} was again slightly lower than the direct interaction force F_{diff}, which is due to the differences between tangent and secant as explained earlier. The continuum force F^{C} is equal to F_{diff}. The opposite sign is due to definition. In conclusion, the coupling algorithm produced the same results as pure molecular evaluation in the case of implicit water.

A third option of water treatment is the explicit case. The results are summarized in Figure 4.13. In addition to the interaction energy E_{int}, the total energy E of the system is presented as well. The interaction energy E_{int} increases for larger distances, similar to the cases

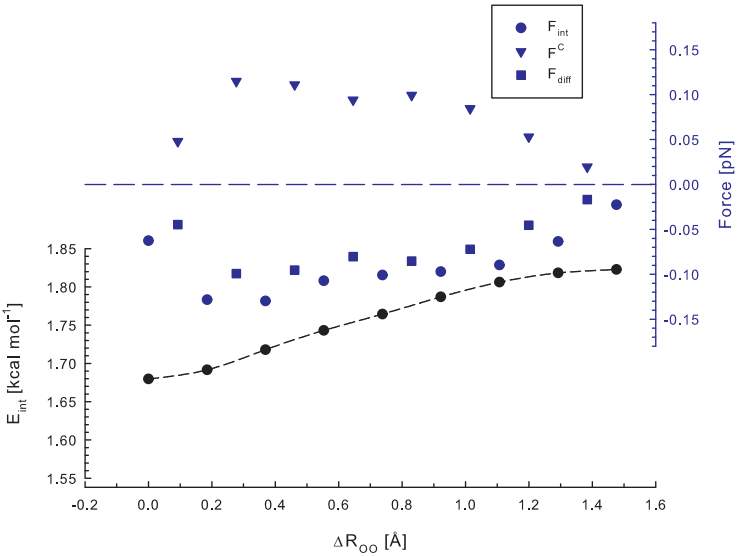

Figure 4.12: Interaction energy E_{int}, intermolecular forces F_{int}, computed forces F_{diff} and forces from Finite Element F^c for the water dimer with implicit water model ACE2 in dependency of the distant change ΔR_{OO} between both oxygen atoms.

before, but is not as smooth. However, the interaction energy of the water molecules is difficult to utilize. The water dimer of interest is in constant contact with the surrounding water and builds hydrogen bonds. This additional contribution is neglected by the interaction energy E_{int}. Hence, the energy magnitude is in the range of the vacuum case. Contrary to the vacuum case, the distance, in which the unbinding takes place, is decreased and comparable to the implicit water case. Because the interaction energy E_{int} does not represent the system correctly, the total energy E of the system has been considered as well. The total energy E substantially decreases from the equilibration configuration to the first distance change. Afterwards, energy changes are small and do not follow a particular order. The averaged forces from the trajectories are in the range of the implicit forces with a maximum

force of $F_{int} = 0.14\ pN$. The forces F_{diff} computed by equation (4.14), using the interaction energy E_{int}, are substantially larger, and so are the forces F^{C} from the coupling algorithm. The problem with the explicit treatment of the water is not the coupling itself but the choice of the right energy on the molecular side. On the other hand, using the total energy E to compute F_{diff} leads to irregular jumping of positive and negative forces.

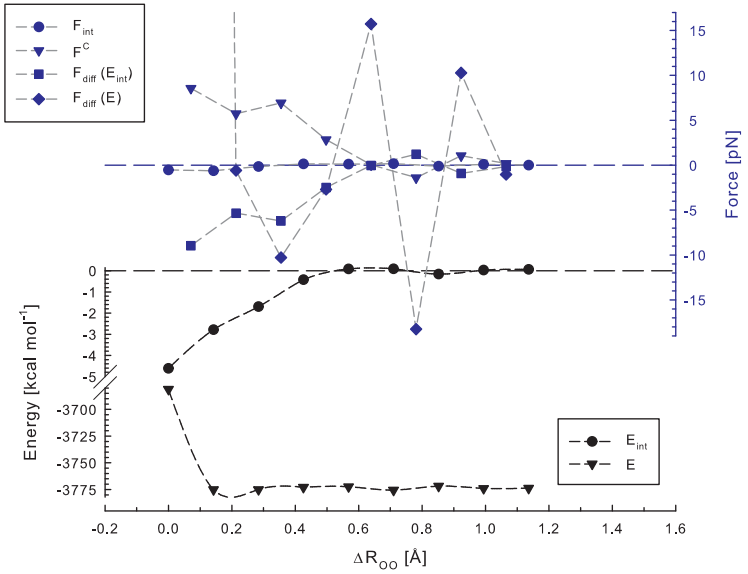

Figure 4.13: Interaction energy E_{int}, total energy E, intermolecular forces F_{int}, computed forces F_{diff} (based on E_{int} and E) and forces from Finite Element F^{C} for the water dimer with explicit water in dependency of the distant change ΔR_{OO} between both oxygen atoms.

The difficulty to achieve comparable results for the explicit case rests in the fact that the bond of interest is formed by the very same molecules which are around these molecules of interest. The constant forming of hydrogen bonds of the central water dimer with its surrounding water molecules leads to an over-estimated interaction energy

in Figure 4.13. The contribution of one or two hydrogen bonds (Figure 4.5) to the complete energy is small and difficult to filter out of the thermal noise in the background. Using the Maxwell-Boltzmann equation

$$E_{kin} = \frac{3}{2}(N-1)k_B T \tag{4.16}$$

with N being the number of atoms, k_B being the Boltzmann constant and T being the temperature, and applying it to the water dimer with the allowed temperature band of 10 K for the thermostat, the kinetic energy is $E_{kin} = 21.4\ kcal\ mol^{-1}$. Energies of single hydrogen bonds are around $E_{HB} \approx 18\ kcal\ mol^{-1}$. The maximum energy difference after the first decrease is $\Delta E = 3.73\ kcal\ mol^{-1}$ and is probably caused by a change in kinetic energy. In order to filter out the water dimer bond (thus detecting the energy change), it is necessary to increase the equilibration time. For the time being it was only possible to analyze 4×10^6 timesteps. The need of detecting a small energy change by long equilibration times makes the total energy E unsuitable.

4.3 Mechanics of the integrin I domain bond to tropocollagen

The water dimer is a versatile model to test the idea for enhancing FE with MD and to compare it to published data. Following this validation the algorithm shall be used now for a larger molecule where experimental data is difficult to obtain.

4.3.1 The molecular structure of the $\alpha_2\beta_1$ integrin I domain and the tropocollagen

The coupling of cells to the tissue is a new and important research area. The distinctive connections between the cell cytoskeleton and the extra cellular matrix (ECM) are important to understand if one wants to comment on force transmission from connective tissue to the cell. Here, the detailed molecular structure of the intra-cellular focal adhesion sites, such as FAK, Talin or Paxillin, shall be neglected and replaced by constitutive modeling of the cell. But the question remains how integrins, which are the primary connectors between the cytoskeleton and the ECM, play their mechanical role in the context of force transmission.

The structure for an integrin is taken from the Protein Database [13]. The identification code of the structure is 1DZI. The structure includes the I domain of the $\alpha_2\beta_1$ integrin bound to a synthetic collagen I triple helix with the amino acid structure *GLY-PRO-HYP* [50]. The complete structure can be seen in Table 4.5.

The three dimensional structure of the protein bound to the triple helix is depicted in Figure 4.14a. This is the original structure from the Protein Database without any modification, visualized by VMD [65]. Water molecules are not shown. The integrin and the collagen peptide are available on the protein database as sole structures, identified as 1AOX and 1Q7D, respectively.

The integrin is built up mostly from α-helices and β-sheets. This is shown in the Ramachandran plot (Figure 4.14b). The main structures are found predominantly in the two tertiary structured regions. At

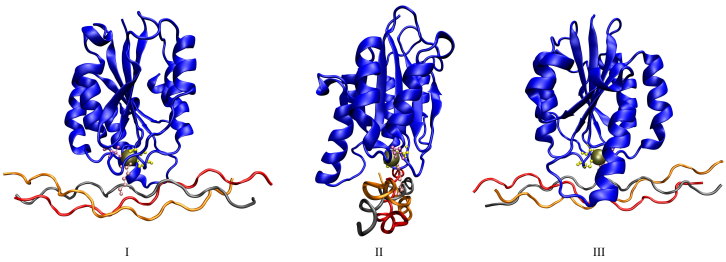

(a) 3D structure

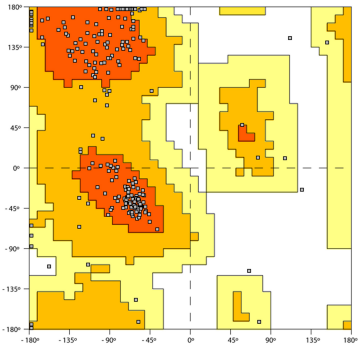

(b) Ramachandran Plot

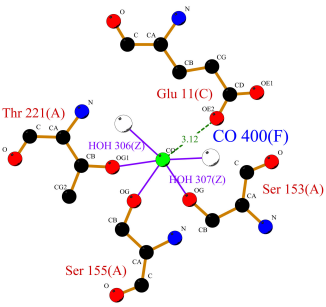

(c) Protein-Ligand plot of interactions involving metal

Figure 4.14: (a) The structure of 1DZI from front (I), side (II) and back (III). The color represents the different chains (drawing method NewCartoon) and the metal ion is the brown sphere in the middle drawn by the VDW representation. (b) Ramachandran plot of the complete structure for tertiary structure. (c) Binding site of the metal ion.

Chain A (Integrin)
ALA LEU ILE ASP VAL VAL VAL VAL CYS ASP GLU SER ASN
SER ILE TYR PRO TRP ASP ALA VAL LYS ASN PHE LEU GLU
LYS PHE VAL GLN GLY LEU ASP ILE GLY PRO THR LYS THR
GLN VAL GLY LEU ILE GLN TYR ALA ASN ASN PRO ARG VAL
VAL PHE ASN LEU ASN THR TYR LYS THR LYS GLU GLU MET
ILE VAL ALA THR SER GLN THR SER GLN TYR GLY GLY ASP
LEU THR ASN THR PHE GLY ALA ILE GLN TYR ALA ARG LYS
TYR ALA TYR SER ALA ALA SER GLY GLY ARG ARG SER ALA
THR LYS VAL MET VAL VAL VAL THR ASP GLY GLU SER HIS
ASP GLY SER MET LEU LYS ALA VAL ILE ASP GLN CYS ASN
HIS ASP ASN ILE LEU ARG PHE GLY ILE ALA VAL LEU GLY
TYR LEU ASN ARG ASN ALA LEU ASP THR LYS ASN LEU ILE
LYS GLU ILE LYS ALA ILE ALA SER ILE PRO THR GLU ARG
TYR PHE PHE ASN VAL SER ASP GLU ALA ALA LEU LEU GLU
LYS ALA GLY
Chain B (Collagen)
GLY PRO HYP GLY PRO HYP GLY PHE HYP GLY GLU ARG GLY
PRO HYP GLY PRO HYP GLY PRO HYP
Chain C (Collagen)
GLY PRO HYP GLY PRO HYP GLY PHE HYP GLY GLU ARG GLY
PRO HYP GLY PRO HYP GLY PRO HYP
Chain D (Collagen)
GLY PRO HYP GLY PRO HYP GLY PHE HYP GLY GLU ARG GLY
PRO HYP GLY PRO HYP GLY PRO HYP

Table 4.5: Residuum and secondary structure of 1DZI. α-helices are marked by blue, β-sheets by red and the binding partner to the metal ion by orange.

first, the protein might look like the typical setup for transmembrane proteins: β-sheets in the middle surrounded by a circle of α-helices. But this is not completely true for this structure. It is more like a parkway with 3 α-helices on each side and 6 β-sheets in the middle. It is interesting to note that the first β-sheet from the front view is directed towards the positive $\boldsymbol{z}$-direction, and all others in the negative $\boldsymbol{z}$-direction. The α-helices are all right hand shaped (Figure 4.14b).

Of special interest is the Co^{2+} metal ion. This ion has six binding sites, whereby two sides are saturated by water, three sides by the integrin itself and one side by the collagen complex. That makes it important for the integrin-collagen bond. Associated binding partners of the integrin are not part of any tertiary structure. That leads to the assumption that when force is applied to the integrin, the first mechanical answer will arise from the orientation of the bound chains at the

metal ion. Saturation of two binding sides of the metal ion with water might also be interesting. As the water is free and not bound to any further higher order structure, it does not look very important from a mechanical point of view. But the question that arises here is what happens when the water is not present. These are important considerations not only for using implicit water models but also for the behavior of the binding itself.

The important atoms involved in the bond are:

- HOH - two H_2O molecules
- OE2 - second oxygen on α-carbon (glutamic acid, res id 11, chain C)
- OG1 - first γ-oxygen on β-carbon (threomine, res id 221, chain A)
- OG - γ-oxygen on β-carbon (serine, res id 155, chain A)
- OG - γ-oxygen on β-carbon (serine, res id 153, chain A)

Once the binding residues for the metal ion are visualized (Figure 4.15a), it looks like a docking station. The trunk from the glutamic acid (GLU) residuum of the collagen dips into the binding pocket of the lower part of the integrin until it is connected to the metal ion. The packing, shown schematically by the binding image in Figure 4.14c, can be seen in Figure 4.15b. The Co^{2+} atom keeps a closer connection to the residuum of the integrin than to the GLU residuum of the collagen triple helix. Figure 4.15b looks from the collagen towards the integrin. The grey area shows cut VDW spheres of the atoms, and the complete sphere is shown translucent.

4.3.2 Model Setup

The mechanical properties of the I domain-collagen bond are mainly determined by the distance between both binding partners. Hence the first characteristic direction (FCD) is chosen along the length of the I domain perpendicular to the tropocollagen. In addition to the importance of the FCD, the stretch of the tropocollagen also contributes. In

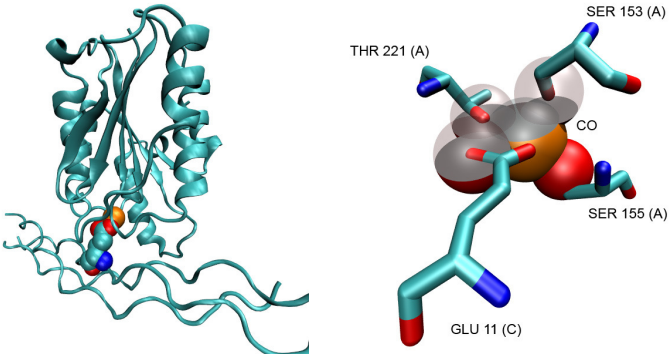

(a) Collagen residuum GLU (b) Packing around cobalt ion

Figure 4.15: (a) The trunk-like connection of the GLU residuum of the collagen triple helix to the metal ion of the integrin. (b) Packing of the metal ion binding atoms.

order to reflect this behavior, a second characteristic direction (SCD) has been chosen along the length of the tropocollagen. The characteristic length of FCD is $l_{FCD} =$ 44 Å; the characteristic length of SCD is $l_{SCD} =$ 56 Å.

The deformation of the molecules has been realized by harmonic potentials applied to the tropocollagen and selected atoms on top of the I domain. Selected atoms are α-carbons of residue 1 to 5, 102 to 103, 35 to 37 and 57 to 60. The location of the atoms is shown in Figure 4.16. The tropocollagen is also restricted using a harmonic potential.

Beside the interaction energy E_{int}, the total energy U is also recorded. The evaluation of the total energy U can be done much more efficiently than other energies as it can be sampled directly during simulations. Hence, no re-evaluation of trajectories is necessary.

Finite Element Method The Finite Element Model consists of one hexahedral element with linear basis functions. The $\boldsymbol{y}^{\mathrm{C}}$-direction of the element is aligned with the first characteristic direction of the molecule.

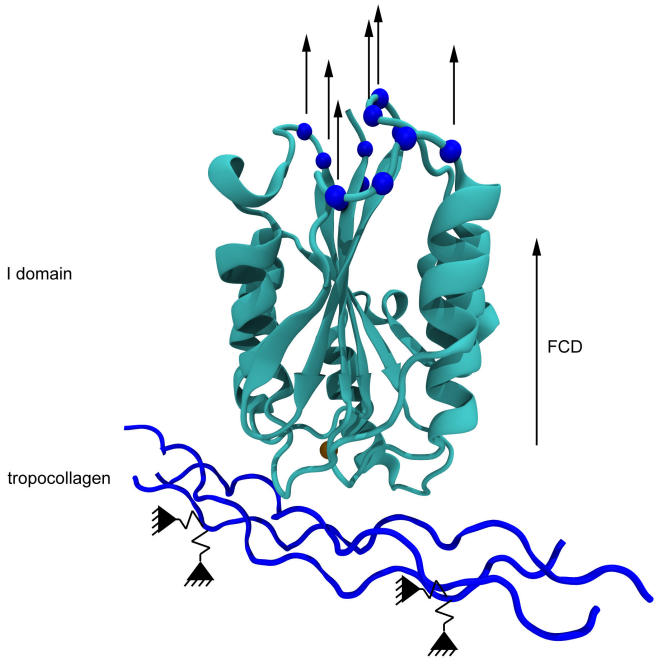

Figure 4.16: 1DZI atoms and chains, which carry boundary conditions (blue). Tropocollagen is restricted by a harmonic potential and α-carbons on top are restrained to the new position by harmonic potential.

Enhanced Assumed Strains are used to avoid volumetric locking. The applied Neo-Hookean material model is described previously in equation (4.7). The density used is the density of water.

FCD is computed as the first principal direction of the element by computing the eigenvectors of the right Cauchy-Green tensor $\boldsymbol{C}$. SCD is given by input and shows in the $\boldsymbol{x}^{\mathrm{C}}$-direction of the element coordinate system. Ten steps have been computed, and $\lambda = 1.5$ in $\boldsymbol{x}$-direction was applied as the Dirichlet boundary condition.

Molecular Dynamics The I domain of the $\alpha_2\beta_1$-integrin, together with the collagen, consists of special amino acids. Accordingly, the CHARMM 22 force field [89] does not include some of them, such as the hydroxyproline (HYP) amino acid of tropocollagen and the Co^{2+} ion.

Force field parameters Hydroxyproline (*HYP*) is a modification of the standard proline amino acid with an additional hydroxyl group (Figure 4.17a). The additional group is believed to form hydrogen bonds to other procollagens and stabilize the triple helix [2]. The origin of hydroproxyline is the lumen of the endoplasmic reticulum. There it is hydroxylated from selected prolines. Additionally, hydroxylysine is built as well. Some of the hydroxyprolines are glycosylated and form with other pro-α chains the procollagen.

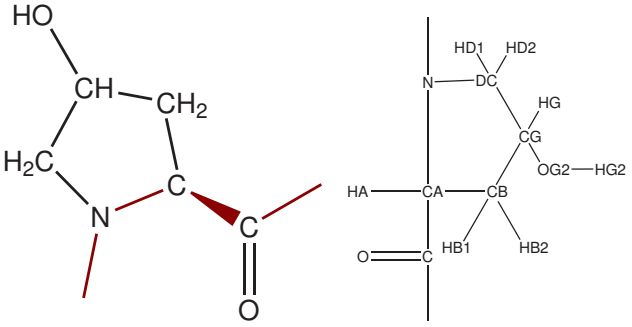

(a) 4-Hydroxyproline

(b) Hydroxyproline structure in CHARMM

Figure 4.17: (a) Chemical structure of 4-Hydroxyproline (backbone in red) (b) Topology structure of hydroxyproline in CHARMM.

The force field of *HYP* is taken from the Amber force field and appropriately modified for CHARMM (Figure 4.17b). The extension of the parameter and topology files can be found in Appendix A.1.

The force field parameters of Co^{2+} are more complicated because data is not directly available. This makes it necessary to take a closer look at the used potentials and possible parameters for the ion. The complete potential energy function for the CHARMM force field 22 is given by MacKerell et al. [89] and here repeated in equation (4.17). The interesting part for the cobalt ion is the non-bonded part, particularly the 6-12 van der Waals potential of the electrostatic interactions.

$$\begin{aligned} U &= \sum_{bonds} K_b(b-b_0)^2 + \sum_{Urey-Bradley} K_u(S-S_0)^2 + \\ &\quad \sum_{angle} K_\theta(\theta-\theta_0) + \sum_{dihedrals} K_\chi(1+cos(n\chi-\delta)) + \\ &\quad \sum_{impropers} K_{imp}(\varphi-\varphi_0)^2 + \\ &\quad \sum_{nonbond} \epsilon \left[\left(\frac{R_{min_{ij}}}{r_{ij}} \right)^{12} - \left(\frac{R_{min_{ij}}}{r_{ij}} \right)^{6} \right] + \frac{q_i q_j}{\epsilon_1 r_{ij}} \end{aligned} \tag{4.17}$$

The Lennard-Jones potential actually used in the parameter files for CHARMM [19] is slightly different and given in equation (4.18a). The equation in the original publication of MacKerell et al. [89] is unfortunately missing the number 2 at the second term of equation (4.18a).

$$\mathscr{V} = E_{ij} \left[\left(\frac{R_{min_{ij}}}{r_{ij}} \right)^{12} - 2 \left(\frac{R_{min_{ij}}}{r_{ij}} \right)^{6} \right] \tag{4.18a}$$

$$E_{ij} = \sqrt{\epsilon_i \epsilon_j} \tag{4.18b}$$

$$R_{min_{ij}} = \left(\frac{R_{min}}{2} \right)_i + \left(\frac{R_{min}}{2} \right)_j \tag{4.18c}$$

$\mathscr{V}$ is the van der Waals interaction potential, R_{min} denotes the finite distance at which the inter-particle potential is minimal and ϵ represents the depth of the potential well. It should be noted that the necessary parameters for the cobalt ion to describe the van der Waals potential are also ϵ and R_{min}. The charge q of the Co^{2+} ion in equation

(4.17) for the electrostatic interaction is given by definition.

The cobalt ion is a central binding partner for the collagen and, due to the mixed nature of the bond, special interest has been placed on the determination of force field parameters. For simulations and testing of parameters, a reduced system was chosen which includes only the main binding partners listed in Section 4.3.1.

The system was minimized, heated, and equilibrated as described next and every equilibration simulation was 10 ns with standard timestep in vacuum. Backbones of residua belonging to the I domain were restricted by a harmonic potential; the α-carbon of the glutamic acid belonging to collagen was pulled by a force. The results of the simulations and the finally used parameters are discussed in the results section (see Chapter 4.3.3).

Additionally, the complete I domain has been simulated with the chosen parameter set to verify the configuration for the complete system, not only for the reduced system. Preparation was done as described and the equilibration time was 150 ps.

Preparation The structure 1DZI was taken from the Protein Data Bank [13] and was stripped of all water molecules. The different parts were then loaded into CHARMM [19] and minimized by steepest descent for 200 steps and further on by the Adopted Newton-Raphson method for 2000 steps [30]. The CHARMM 22 force field [89] was used with modifications mentioned earlier. For the implicit treatment of water, the ACE2 model [23, 117] was chosen. The parameters for the Co^{2+} ion were determined following Schaefer et al. [116] and can be found in Appendix A.2.

The molecule was heated from 0 K to 310 K with a temperature increment of 1.55 K over 100 ps. Subsequently, the structure was equilibrated at 310 K for 150 ps. The temperature was controlled by a thermostat with 10 K temperature width. For time integration, explicit Leapfrog-Verlet was used.

Simulations For simulations, the molecule was restricted following Figure 4.16. Three different simulations with equilibration times of 250 ps, 500 ps and 1000 ps were carried out for 10 steps. The time to allow to move into the new configuration was 250 ps for the first run, and 500 ps for all following runs. Every second coordinate set was written to the trajectory file and analyzed for the interaction energy E_{int}.

4.3.3 Computational results

The intergin results are split in testing the force field parameters for the cobalt ion and the actual results to compute the mechanical properties of the I domain-collagen bond.

Co^{2+} ion

Data for Co^{2+} force field parameters are published by Vedani et Huhta [144] and Amunanto et al. [5], and the work of Kritayakornupong et al. [81] is relevant for the Co^{3+} ion. Due to the difficult nature of metal ion bonds, two-body potentials are believed to cover not all interactions. In general, the interaction between e.g. additional oxygen atoms should be included. Here, only two body potentials were available. Hence, parameters for multibody potentials were adjusted for a two body potential. Table 4.6 shows tested parameters.

ϵ	R_{min}	source
-0.014000	0.387249	Vedani et Huhta [144]
-0.130409	0.955949	Amunanto et al. [5]
-0.130409	1.336291	Kritayakornupong et al. [81]

Table 4.6: Co^{2+} parameter in literature (ϵ and R_{min} as defined in equation (4.18a)).

In addition to the published data, other attempts were made to derive parameters. First of all, the derivation of parameters was tried from cobalt itself. Another attempt was to use better described ions, e.g., Zinc ions, as a basis for Co^{2+} parameter. All these attempts were not successful (data not shown here).

The verification of possible parameters for the Co^{2+} ion was conducted in two steps. First, several parameters were tested on a reduced system, including the main binding residua of the cobalt ion. Second, the best parameters were used to simulate the complete structure, and the results were compared to the published structure.

The parameters in Table 4.6 were used for a 10 ns simulation with a small force on the collagen glutamic acid (GLU). At the end of the simulation, the configuration and binding partner of the cobalt were investigated. Figure 4.18 shows the main configurational changes after 10 ns.

The change of the GLU residuum of the collagen (Figure 4.18b) was prominent. The cobalt ion is bound to both oxygen atoms of the glutamic acid. This bond resisted forces up to 500 pN in the simulations. The small switch also resulted occasionally in complete unbinding of the I domain residua when using the parameters from Amunanto et al. or Kritayakornupong et al. Sometimes it was observed that the cobalt ion bound to two oxygen atoms of the c-terminus of the reduced system. The second oxygen was added during the preparation of the molecule to build a functional c-terminus, because the backbone was discontinued. These results are due to the reduced system and have not been included in the analysis, but they show the high affinity of the cobalt ion to bind to two neighboring oxygen atoms.

Another configurational change was the flipping of the backbone oxygen of the asparagine (ASN) amino acid (Figure 4.18c). The binding to the new oxygen atom changed the coordination of the cobalt ion, but did not result in any large configurational changes.

Interestingly, the last observed configurational change happened only at smaller forces (< 100 pN). Here, the serine residuum (SER) slided along the cobalt ion, with the bond to the oxygen of the rest group dissolved, and building a new bond to the backbone oxygen.

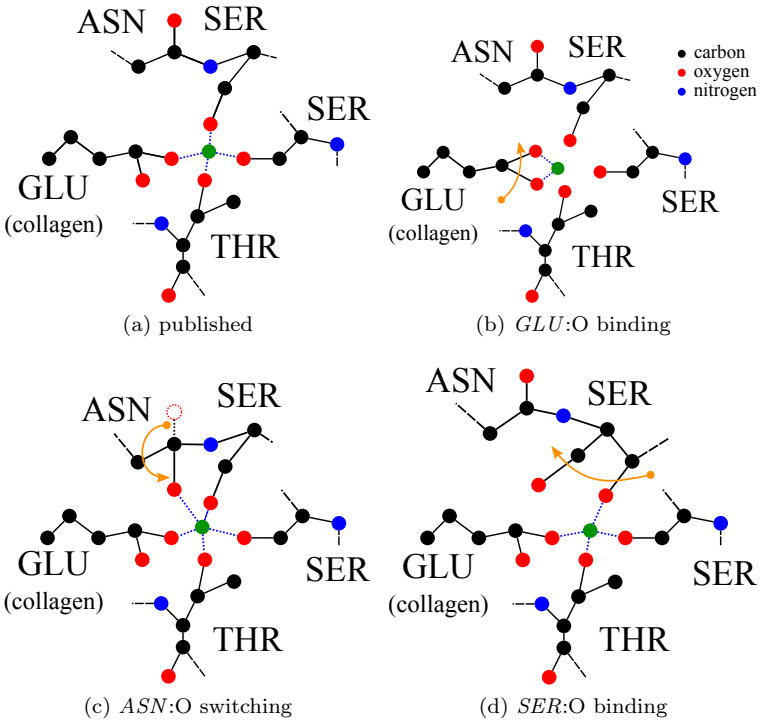

(a) published (b) *GLU*:O binding

(c) *ASN*:O switching (d) *SER*:O binding

Figure 4.18: Configurational changes of the reduced model after 10 *ns* equilibration time.

From all three parameter sets in Table 4.6 the values of Vedani and Huhta [144] preserved the equilibrated configuration best. But in comparison to the original published distance between oxygen atoms and the cobalt ion, the distance to the serine residuum was substantially reduced. To achieve smaller distances to the neighboring oxygen atoms, the van der Waals parameter ϵ was increased from $\epsilon = 0.014\ kcal\ mol^{-1}$ to $\epsilon = 0.029\ kcal\ mol^{-1}$. This indeed resulted in a closer bond between the cobalt ion and the oxygen atoms apart from *SER*, but did not reproduce the original distances. Studying the original structure, it became clear that additional water atoms between SER, and aspartic

acid (*ASP*), and the cobalt ion have a shielding function, which is not present in the reduced structure.

To further investigate the role of additional water, the complete I domain bound to tropocollagen was simulated using ACE2. Two different parameter sets, one from Vedani and Huhta [144] and another with increased ϵ (including and excluding additional water molecules) were simulated. After equilibration, the configuration around the cobalt ion was analyzed. It was observed that the distance of the *SER* 155 residuum increased substantially from 1.89 Å in the minimized configuration to 3.62 Å compared to the original distance of 3.22 Å. The result for the published parameter set plus water is shown in Figure 4.19.

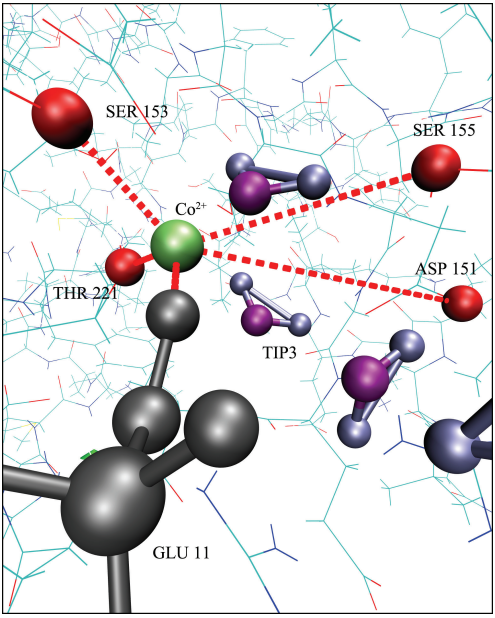

Figure 4.19: Configuration after equilibration with additional TIP3 water molecules.

Although the results, including water molecules in the binding pocket, were closer to the original experimentally derived structure, there are some important issues to raise. Namely the problem of using an implicit water model together with TIP3 water molecules. Basically, it would be possible to exclude those water molecules from an implicit treatment, but not the surrounding residua. This brings some uncertainty to the simulation. Mainly for that reason, the published parameter set by Vedani and Huhta [144] was chosen as Co^{2+} Lennard-Jones parameter (Table 4.6).

Beside the parameter tests, two important findings regarding the CO^{2+} metal ion can be drawn from these simulations:

- The bond strength of both acid residua, aspartic and glutamic acid, bound to the cobalt ion.
- The importance of water. By including water next to the collagen serine, the coordination of the cobalt ion changes. The coordination might further change, once water can flow into the binding pocket, and consequently changes the coordination of the cobalt ion.

Mechanical properties

The mechanics of intergins is a complex process, in which activation and deactivation of integrins and the mechanics of the extracellular tail of integrins play important parts. Previous work modeled the integrin connection as linear spring [37], whereby the focus of the work was not on the force transmission between ECM and cell but on shear stresses caused by bubbles flowing over the cell. Here, the mechanical properties of the I domain of an intergin bound to tropocollagen are investigated with molecular dynamics simulations in order to shed some more light onto integrin mechanics.

The mechanical properties have been computed using the interaction energy E_{int} between the I domain of the $\alpha_2\beta_1$ integrin and the tropocollagen. The energies for different equilibration times t_{equi} can be seen in Figure 4.20. For the first six strains up to $\lambda = 1.25$, the energy values for the different equilibration times are comparable. All res-

ults predict the first significant energy change at strains from $\lambda = 1.15$ to $\lambda = 1.2$. The following energy decrease is covered independently of the equilibration time. Then, the course of energy starts to differ. While the shortest time with $t_{equi} = 250\ ps$ is predicting a strong energy increase with some slowdown at $\lambda = 1.5$, the longer equilibration times suggest a different behavior. Here the energy again decreases after intermediate increase; for a equilibration time of $t_{equi} = 500\ ps$ at $\lambda = 1.45$ and for $t_{equi} = 1000\ ps$ at $\lambda = 1.35$. The data suggests that longer equilibration times allow for another energy plateau at smaller strains. The interaction energy E_{int} suggests a reorientation phase from the start to $\lambda = 1.15$ with no significant force generated, followed by an initial increase in energy at $\lambda = 1.2$, where a significant force between the I domain and the collagen is generated. Then another stable configuration is achieved before the second increase of energy takes place, depending on equilibration time. For longer equilibration times, the second increase is at smaller strains. Another energy plateau region can be observed at the end for the longest equilibration time.

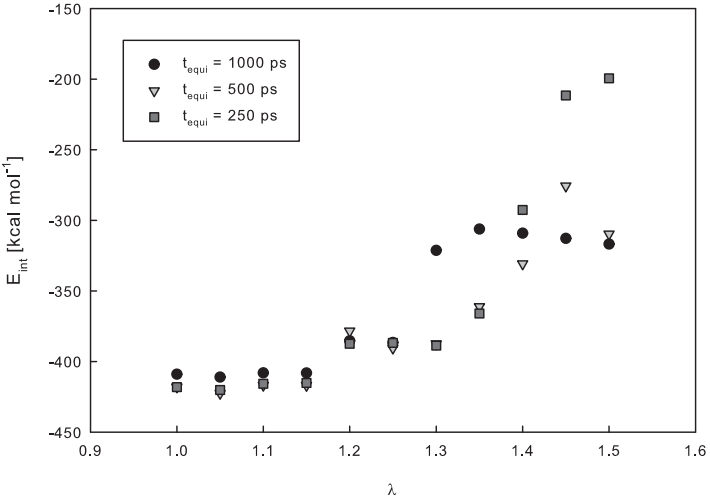

Figure 4.20: Interaction energy E_{int} over FE axial strains λ at various equilibration times t_{equi}.

The development of the forces is presented in Figure 4.21. The plots are drawn over the same range of stretches like in the energy graph in Figure 4.20. The coupling forces are based on the proposed energy difference approach introduced in equation (4.1) and subsequent formulas. The generated Cauchy stresses σ reflect the change of the energy. For higher energy differences, stresses are generated at corresponding strains λ. The first force peak at $\lambda = 1.025$ appears for all equilibration times, though the absolute value is slightly different. For $t_{equi} = 250\ ps$ the stress is 3.4 $pN\ nm^{-1}$, for $t_{equi} = 500\ ps$ 4.6 $pN\ nm^{-1}$ and for $t_{equi} = 1000\ ps$ 2.7 $pN\ nm^{-1}$. Following the first stress peak, a slow increase of stress is observed for $t_{equi} = 250\ ps$ and $t_{equi} = 500ps$. For the longest equilibration time $t_{equi} = 1000\ ps$, the stress behavior is different after the first stress peak. It shows a second stress peak with 6.9 $pN\ nm^{-1}$ at $\lambda = 1.275$ and decreases afterwards to substantially smaller stresses. In general, the stress depends significantly on the length of the equilibration time. The behavior of the longest equilibration time suggests that single events in the binding of the I domain to the tropocollagen are responsible for the bond mechanics.

Looking at the stress results from Figure 4.21, they do not look like a ordinary constitutive description known from continuum modeling. Though stresses are closely related to the actual molecular forces, as shown for the water dimer, the current method of using adjoined strains for computing the energy difference does not allow for storage of elastic energy in the element.

To address this issue, another way of computing the energy difference is proposed in equation (4.13). Here, the difference is computed between the lowest energy value and the current value. The finite element is in consequence able to store energy. The corresponding stress results σ can be seen in Figure 4.22. The first observation is that the stress-strain curves flatten out for larger equilibration times. While at $t_{equi} = 250\ ps$ the stress curves show two clear peaks; the curve at $t_{equi} = 1000\ ps$ shows only one distinctive peak with a mildly decreasing stress afterwards.

Another difference between the different equilibration times is the stress level. It should be noted that the scaling of the y-axis is larger for $t_{equi} = 250\ ps$ than for the other equilibration times. Longer equilibration times produce lower stress levels. For the longest equilibration

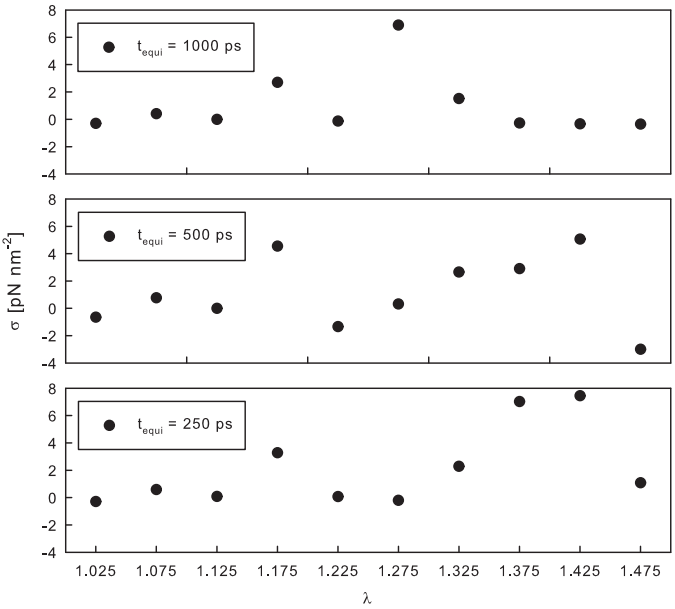

Figure 4.21: Cauchy stresses σ using the differential method.

time, the maximum stress is nearly 2 $pN\ nm^{-1}$. The stress curve shows a small increase at the beginning with a significant stress increase at $\lambda = 1.3$.

For all results in Figure 4.21 and Figure 4.22, a Poisson ratio of $\nu = 0.3$ was used. This is a common value used for molecules, e.g. Bathe [10]. The Poisson ratio influences the stress results. Which Poisson ratio should be used for molecules, has not been finally answered up to now. For that reason, the stress was computed for different Poisson ratios ν: the common value in the literature $\nu = 0.3$, additionally $\nu = 0.0$ and $\nu = 0.49$ as extrema. All three values of ν have legitimate explanations. This difference shall be discussed further in Section 4.4.

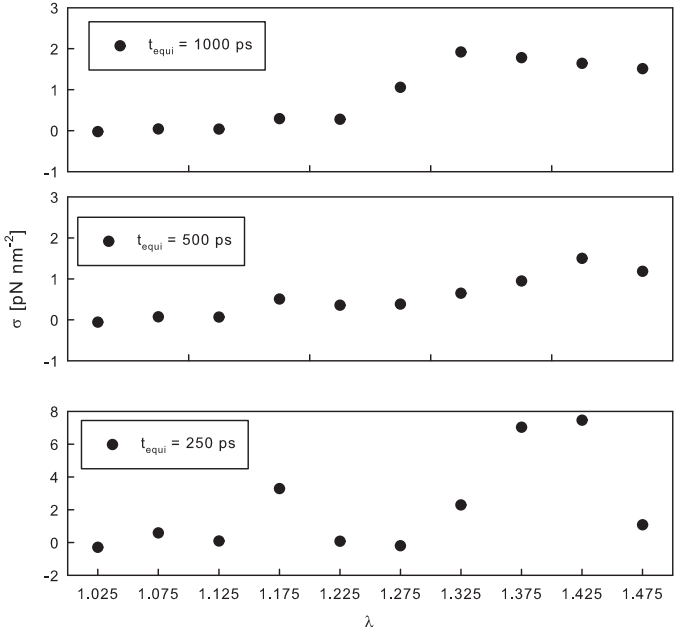

Figure 4.22: Cauchy stresses σ with stored energy approach.

Here, only the differences in the stress shall be shown. The higher the Poisson ratio is, the higher the stresses are. The maximum stresses for $\nu = 0.49$ is $\sigma = 4.4\ pN\,nm^{-1}$, for $\nu = 0.3$ is $\sigma = 2.0\ pN\,nm^{-1}$ and for $\nu = 0.0$ is $\sigma = 0.8\ pN\,nm^{-1}$.

One of the advantages of the proposed method is that the molecular structure and the configurational changes are fully computed. Hence, relevant amino acids, which coordinate the metal ion, can be observed. The distances between the main binding partners of the metal ion, given in Figure 4.14c, can be easily followed. Figure 4.24 shows the distances between the oxygen of the collagen glutamine and the other binding partners: the oxygen atoms of the two serine residue and the

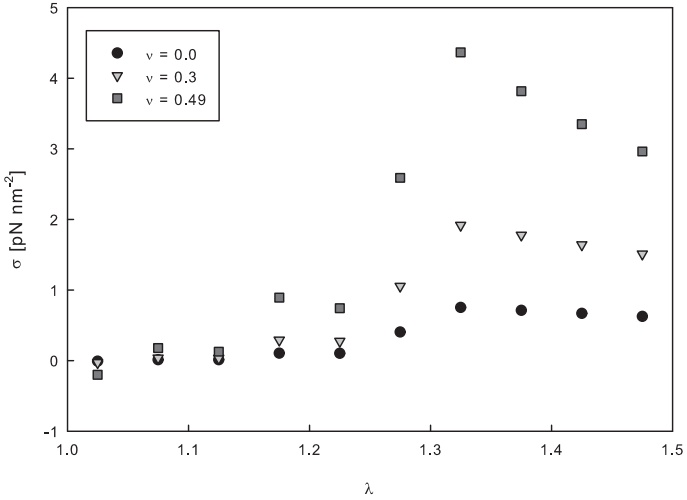

Figure 4.23: Cauchy stress σ for different ν.

threonine residuum. The distances between all oxygen atoms stay constant at the beginning, while the I domain is pulled away. Because all observed residue belong to loops of the I domain, it is likely that the first steps flatten the loops. Consequently no force is generated and the distance between all oxygen atoms remain constant. At the first force peak, the distances of both serine oxygen atoms increase while the distance of the threonine oxygen remains constant. Looking at the three-dimensional structure, it becomes clear that both serine residues unbind from the metal ion. At the second large distance change at step 6 in Figure 4.24, the second stress peak in Figure 4.21 is produced and the metal ion is unbound from the glutamine of the collagen. Interestingly, the distance of the α carbon and the oxygen of the glutamine is constant all the time. Here it was expected that the rest group would also stretch out, but the results suggest that it is already stretched at the beginning of the simulation.

The metal ion contributes significantly to the mechanical properties of the I domain-tropocollagen bond. However, there are some other

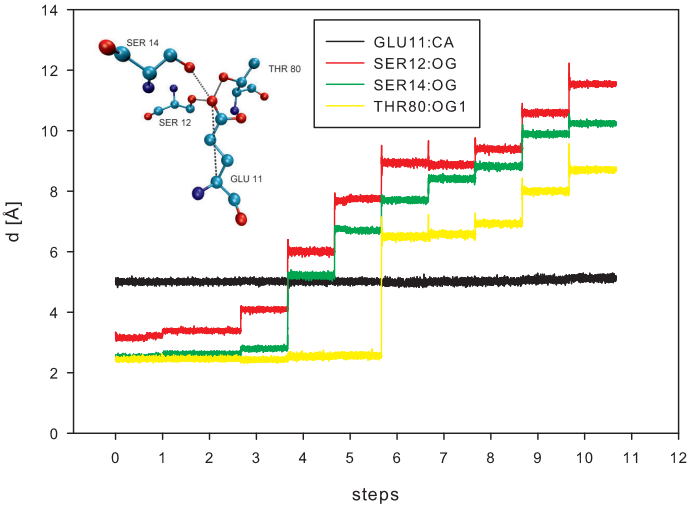

Figure 4.24: Distances between Co^{2+} binding partners at different steps.

bonds as well which contribute. In the original structure four H-bonds [50] exist between collagen and I domain. All H-bonds, except one, are dissolved during pulling. The remaining H-bond is between the histidine 117 of loop 3 (L3) of the I domain and the hydroxyproline 15 of the tropocollagen (Figure 4.25). The configuration in Figure 4.25 shows the last step. The H-bond keeps helix 4 in place which can be seen in Figure 4.26. The different colors show the configuration at different steps. Red indicates the configuration at step 0, white the configuration at step 5, and blue the configuration of the last step. During all steps, helix 4 remains at the same height. Consequently, the upper part of β-sheet D (hidden in the figure) which is connected to helix 4 by a short loop is fixed and cannot move away from the collagen. Since the other β-sheets move and are connected to β-sheet D, the lower part of β-sheet D moves up. Because the upper part is fixed and the lower part moves up, β-sheet D consequently turns. The lower end of β-sheet D is connected by a loop to the lower end of helix 6. Hence, the turning is transferred to the helix. This turn can be observed in Figure 4.26.

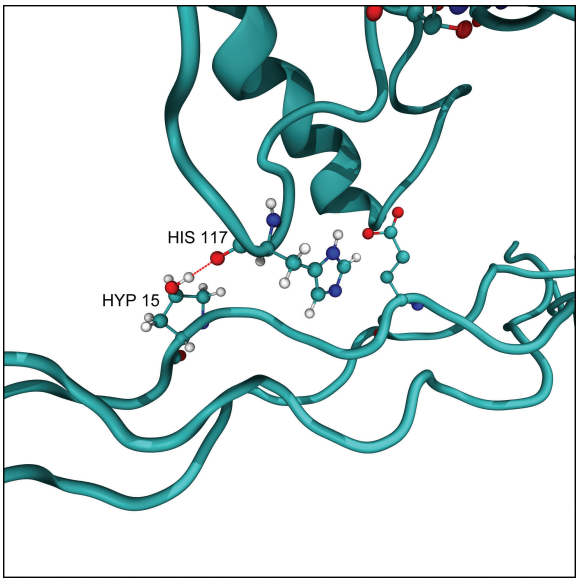

Figure 4.25: H bond between I domain and tropocollagen

4.3.4 Energy curve for a continuum material model

The current scheme makes it necessary to compute E_{int} at every strain. This is a computationally expensive approach. It would be better if the material behavior would have a continuous description. It would be computationally more efficient and would avoid the necessity to compute the molecular structure every time. For that reason, the small strain regime of the integrin was computed with more data points and longer equilibration times ($t_{equi} = 2ns$). The computed interaction energy points are used as a basis for a natural spline fit. The resulting curve can be used in FE simulations as an input for the integrin material model. Figure 4.27 shows the energy data points and the fitted spline.

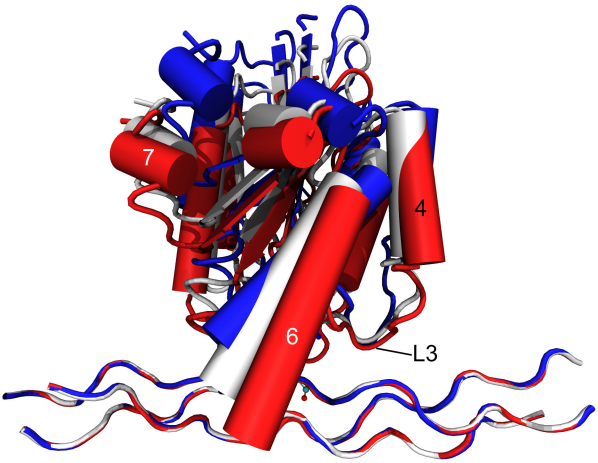

Figure 4.26: Movement of α-helix 6

Interestingly, the curve in Figure 4.27 shows a new intermediate state at around $\lambda = 1.10$ which was not resolved before. The equation and coefficients for the fitted curve can be found in Appendix B.

4.4 Discussion

The binding mechanism of integrins to the extra-cellular matrix (ECM) has been studied before, both theoretically as well as experimentally. Experimentally, the forces, which are necessary to pull cells away from substrates, can be measured by Atomic Force Microscopy (AFM). By analyzing the force-distance curve from the AFM, the force of individual bonds can be isolated. Li et al. [85] measured the force for the $\alpha_5\beta_1$ integrin-fibronectin interaction while Taubenberger et al. [138] analyzed

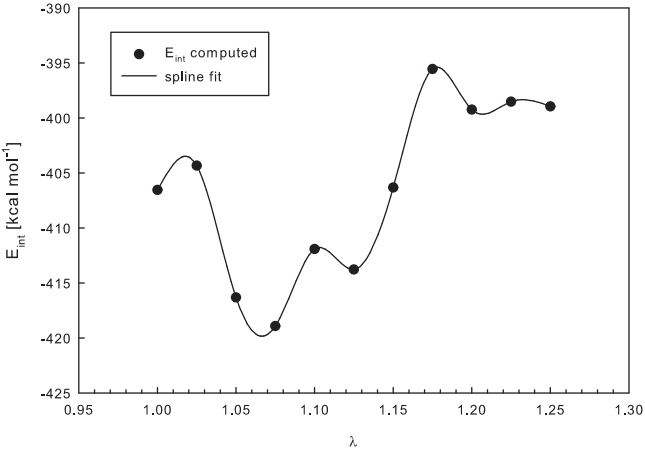

Figure 4.27: Fit of interaction energy E_{int} data points with cubic splines.

the force-distance curves of the $\alpha_2\beta_1$ integrin interaction with type I collagen. Possible binding mechanisms of the integrin-fibronectin bond were investigated by steered molecular dynamics [80]. The importance of the metal ion-dependent adhesion sites (MIDAS) was already mentioned by Emsley et al. [49, 50]. Especially, the coordination of the metal ion plays an important role. This property has been investigated with molecular dynamics simulations by Craig et al. [34] and the importance of MIDAS sites for cell mechanics was highlighted by Gao et al. [54]. The binding site of the integrin to collagen type I was subject to long-term ($> 100\,ns$) molecular dynamics simulations [156], but with an eye towards the equilibrated configuration of the integrin-collagen complex in comparison with the integrin-gel interaction. As focal adhesions consist of integrin bundles, the mechanics of complete focal adhesions is of interest for cell mechanics. Thermodynamical motivated models from Yang and Zaman [153] try to predict the free energy of focal adhesion with respect to distance and adhesion surface coverage.

The forces of single bonds can be investigated by Atomic Force Microscopy. Li et al. [85] probed the force between different fibronectin structures and the $\alpha_5\beta_1$ RGD loop, which includes a metal ion as well. They found forces for single unbinding events of $69 \pm 1.5\ pN$ (mean $\pm$ SE). After activating the integrin, the force increased to $93 \pm 1.5\ pN$. Due to AFM tip fluctuations, which generate forces of around 20 pN, forces lower than 30 pN were not considered as unbinding events in the work of Li et al. The force-distance curve for the $\alpha_2\beta_1$ integrin-collagen interaction was investigated by Tannenberger et al. [138]. Similar to the results of Li et al., they found two force levels. The lower force niveau was at 30 to 40 pN at a loading rate (AFM tip) of 2 $pN\ sec^{-1}$. Lower rupture forces of 15 to 20 pN were reported by Fabry's group (personal communication).

Before discussing the integrin results, one important point regarding molecular dynamics simulations and force levels should be addressed. In general, it is known that molecular dynamics simulations require larger forces for, e.g. configurational changes than necessary in reality. This has been mainly attributed to the lower timescales of typical MD simulations. All-atom simulations of proteins in the range of several nanoseconds are still computationally challenging. Processes in reality take much more time than simulated timescales. Recently the gap between experimental and simulation results got a step closer [84]. For Tritin, a prominent protein for mechanical investigations, rupture forces while unfolding were investigated at different pulling velocities. By increasing the simulation time, it was possible to reduce the pulling velocity and rupture forces. Results are now closer to experimental AFM results, though there is still a gap left. Interestingly, the velocity vs. rupture force curve can be nicely fitted by a model developed by Hummer et al. [63].

In this work, we were interested in the mechanical behavior of the integrin-collagen interaction through a MIDAS interface at small strains. The intention of this work is to derive mechanical properties which are usable for Finite Element simulations. In the first part of this work, a water dimer was studied to investigate the coupling algorithm between Molecular Dynamics and Finite Element. The results and the relation to published work were discussed in Chapter 4.2.2. Here the

results of the I domain interactions of the $\alpha_2\beta_1$ integrin with tropocollagen are discussed.

The maximum computed stresses are, depending on the treatment of the energy, $\sigma_d = 6.9\ pN\ nm^{-2}$ or $\sigma_s = 1.9\ pN\ nm^{-2}$. Here the subscript d refers to the current difference method and s to the storage method in Chapter 4.1.3. The highest forces are due to the glutamine-cobalt ion bond breakage. This can be seen in Figure 4.24, where the appropriate distance increases at the step where the highest force is computed. Both stresses make sense, depending on the point of view. The higher stress of σ_d reflects the actual molecular force in the system, but is problematic in case of an energy plateau. It is unlikely that this configuration represents a molecular stable position, as thermal energy is higher than a possible depth of this plateau. But due to averaging, mechanically, it would be a stable position. In that case the second stress σ_s makes more sense, because the energy difference between the lowest and the current interaction energy is used. For the discussion of rupture forces, the use of σ_d makes more sense because of two points. First, the maximum stress is higher. Second, the rupture force is more correlated to single unbinding events as is σ_d. The maximum occurring force is $F_d = 7.8\ pN$ if an area of $A = 0.88\ nm^2$ is considered, computed from the finite element. This is smaller than experimental results, which report lowest rupture forces at around 20 pN. Smaller forces than 20 pN are experimentally difficult to detect due to fluctuation of the AFM tip. Hence, smaller forces are absolutely possible but have not been considered experimentally. Another reason for the smaller forces is that the I domain is not completely pulled away from the tropocollagen. Unlike experiments, the presented simulations cover small strains. This results in remaining interactions at the end of the simulation (Figure 4.25 and Figure 4.26) whereas experimentally, no interactions exist anymore. It can be concluded that the computed stresses by the coupling of the I domain of $\alpha_2\beta_1$ integrin to tropocollagen are reasonable and within an expected range. For a continuous description of the material behavior, the energy values E_{int} were fitted with a spline. This allows an easy evaluation of energy differences at different strains and serves as a material model for FE simulations.

The coordination of the cobalt ion plays an important role in the

interaction. One of the advantages of using the proposed technique is the instant availability of molecular changes for analysis. As Schulten normally points out, molecular dynamics allows the power of a computational microscope. This is also valid for the structure used here. But due to the implicit treatment of the water, the coordination of the metal ion was changed, which should be taken into account. The Co^{2+}-ion was coordinated only by the oxygen atoms of the two serine and one threonine residuum on the I domain, and the glutamic acid of the tropocollagen. Following the structure over time, the two serine residua first unbind from the metal ion before the glutamic acid - metal ion bond is broken. Our results show a different behavior than the structure proposed by Emsley et al. [49]. In the unbound structure of Emsley and coworkers, the coordination of the two serine residua is conserved. The missing coordination from the glutamic acid is substituted by a direct bond to the threonine. The early loss of the serine coordination in the simulations might be an artifact of implicit water. We speculate that the infiltration of additional water atoms, as found in the original structure from the PDB, generally weakens the coordination of the glutamic acid.

Another shortcoming of the implicit water model is connected to a possible coordination of the metal ion through additional water molecules. These additional water molecules might flow into the binding pocket of the I-domain during the unbinding. The rest group of the glutamic acid gets pulled out and, together with the movement of the tertiary structures of the I-domain, might open space for water molecules to flow in. These water molecules can then play a role in the coordination of the metal ion and influence the binding between the tropocollagen and the I-domain. Currently no explicit water is used in the simulation, so this effect won't be taken into account.

Beside the direct coordination of the metal ion, the unbound structure shows one more significant difference to the computed structure. In the unbound structure, there exists an additional helix in contrast to the bound structure. The development of a helix cannot be observed in the simulation. There might be two good reasons for that. The first reason might be the applied boundary conditions; in particular, the α-carbons of the upper loops, which were chosen to pull the I domain away. Because of the remaining H-bond and the chosen

α-carbons, helix 6 is not pulled up and starts to turn. This configurational change is not reported in the unbound structure. Another configurational change, important for the formation of the new helix, is similar in the computed structure and the published one: the large movement of helix 7. Second, the simulations are not performed until complete unbinding. Especially the remaining H-bond interaction in Figure 4.25, between the backbone of the histidine and the remaining group of the hydroxyproline, might stop larger configurational changes of loop 1 to 3, which is observed in the unbound structure.

The Poisson ratio ν is an important continuum parameter for the mechanical treatment of the molecular results. There is no clear rule what Poisson ration ν shall be used for molecules, though in general $\nu = 0.3$ is used. Looking at the computed structure, there are arguments for different values of ν. Even in case of implicit water, it is not straightforward to compute a volume, which represents the molecule. One possibility would be to compute the solvent excluded surface (SES) and the enclosed volume. Connecting them to a Poisson ratio on the fly proves difficult. A connection of volume change and an appropriate Poisson ratio or material parameter for a penalty function would be needed. Taking explicit water into account, the selection of ν does not become easier. In MD simulations, the water box is usually static. This is in contrary to the deformation of the element. For all these reasons, stresses have been computed at two extreme Poisson ratio values and $\nu = 0.3$, a value commonly used in the literature. Comparing the highest force value $F_d = 16.9\ pN$ from simulations (for $\nu = 0.49$) to reported rupture forces, the force is in the range of expected values. Though ν is influencing the absolute value of stresses, the general course of the stress-strain curve is not changed.

Future investigations should address the coordination of the metal ion and the influence of pulling direction and collagen strain. The first one might prove challenging as the underlying force field to represent metal ion interactions is not fully embodying all these interactions. This is a general problem for all metal ions and is not satisfactorily solved for the time being. One improvement to the simulation might be the use of explicit water, which was omitted here due to computational costs. One improvement, which is already included in the code base, is the use of

a second characteristic direction aligned with tropocollagen. It would allow a mechanical map of the I domain-tropocollagen interaction in dependency of pulling direction and collagen strain, which could greatly enhance understanding of mechanotransduction.

Chapter 5

Conclusion & Outlook

Inflammation due to mechanical ventilation is dangerous for patients, especially when ventilated over a longer time span. The correct ventilation strategy can help patients, but the selection of this strategy is non-trivial without detailed knowledge of the inflammation origin. The mechanobiological environment of alveolar pneumocytes was investigated with the purpose to obtain more insight into the inflammation origin. The working theory is that mechanical stimuli, generated by mechanical ventilation, are transferred from the tissue to the cell and provoke inflammation intracellularly. In order to model the stimuli transfer, one important component is the mechanical behavior of parenchym, pneumocytes and focal adhesions, the distinctive connection points between the extracellular matrix (ECM) and the cell. These three parts have been studied in addition to experimental measurements of local alveolar strain.

For the simulation of the mechanobiological environment, not only material description of the different components are necessary, but the geometry of alveoli as well. For the first time, Neutron Computed Tomography (NCT) was used to image the lung. Although NCT was not able to resolve alveoli, the characteristics of neutrons, to discriminate between water and air, resulted in the resolution of lung structures in the size of 50 μm. Starting from the trachea, it was possible to follow the airway tree consistently up to the 6^{th} generation, and in some

cases, even up to the 10^{th} generation.

Mechanical ventilation can cause over-stretching of alveolar tissue. In order to investigate local strains in single alveoli in comparison to externally applied global strain, a uniaxial tensile machine was placed beneath a fluorescence microscope. The tensile machine stretched the tissue while the microscope imaged the same alveoli at different strains. Additionally, a force sensor was placed between the tissue and the tensile machine and forces were recorded during pulling. At the maximum global stretch $\lambda_{global} = 1.45$, the local stretch is $\lambda_{local} \approx 1.25$. The local stretch shows first a linear regime from $\lambda = 1.00$ to 1.25 with respect to the global stretch, followed by non-linear characteristics. While stretches are highly heterogeneous for different alveoli, local stress-stretch curves are comparable. This finding suggests that stress levels on a local scale are in a comparable range. Another possibility to use the recorded image data is to take it as a basis for a simplified geometric reconstruction of single alveoli as shown in Figure 5.1.

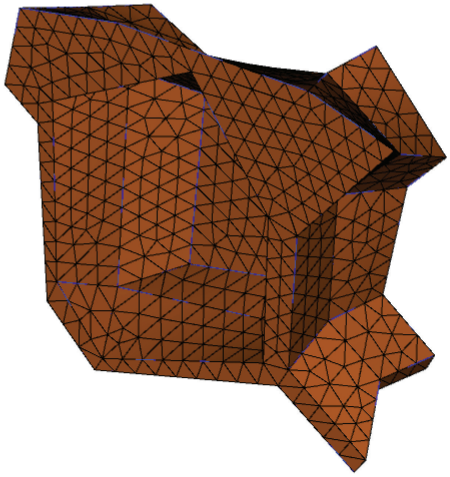

Figure 5.1: Avlveolar geometry obtained from three-dimensional microscopy stacks.

The alveolar strain is transferred to cells; in general, to type I or type II cells, which make up the epithelial. For the Finite Element (FE) simulation of the cell, an appropriate material law for the cell is necessary. Here, a cell model was formulated, composed by strain energy density functions, representing the different mechanically relevant constituents of the cell. It consists of a homogeneous term representing the actin network and an anisotropic term for the actin stress fibers in tension and microtubules in compression. The formulation was discussed in terms of stress-free reference configuration and convexity. It was found that for compression the current framework proves difficult because the convexity criteria is generally not fulfilled. The proposed formulation can not circumvent this problem. Additionally, the model fulfills the important stress-free reference configuration. To cover the active behavior of the cell, a new term was introduced, which describes the contractibility of the cell. It allows the computation of the actin stress fiber direction in the reference configuration and enhances the elastic stress computation by contractile stresses.

Tensile stresses are generated because the cell contracts and is, at the same time, connected to the surrounding ECM by focal adhesions. Vice versa, tissue strain is transferred to the cell by focal adhesions and results in cell stretching. This makes focal adhesion an important part of the mechanobiological environment. In order to simulate the mechanical behavior of focal adhesions or integrins, the components of integrins, in detail, the molecular bond between the I domain of the $\alpha_2\beta_1$-integrin and tropocollagen, was investigated. The continuum based material description of the bond was enhanced with homogenized molecular information. The I domain was pulled away from the tropocollagen and the difference in interaction energy between the original and current configuration was used to compute the mechanical properties. The basic assumption is that the energy change on the molecular scale is equal to the energy change on the continuum scale. The method allows for the detection of single unbinding events and gives a precise mechanical description of the molecular interactions. Stresses generated in FE by molecular unbinding events are around 7.8 pN. As an additional benefit, it allows to study the molecular changes, as atoms are fully resolved on the molecular scale.

Vision of and outlook to a mechanobiological model The current work is a first assembly of small stones in a mosaic, where many stones are still missing. The driving force of the current work was the vision to better understand some aspects of the force transfer from the organ to the molecular level. But this work is still far from finished. Some of the questions regarding the force transfer from the ECM to the cell could be answered, but new questions were raised during the course of research.

One question in particular was the treatment of the Poisson ratio for parenchym and molecules. The question regarding the Poisson ratio of the parenchym emerged from the experiments with the alveolar tissue. A first assumption during the experiments was that the tissue is incompressible due to the liquid filled-alveoli. As outlined in detail in the discussion of the experimental chapter, the assumption was found difficult to justify. More detailed measurements of the Poisson ratio in the large strain regime would be beneficial for simplified models. The Poisson ration is somewhere related to the description of the volume change during large strains, which is another interesting area of research. It includes e.g. the extension of penalty approaches to enforce incompressibility to properly describe the volume change of tissue. These models would be beneficial for the mechanical description of alveolar tissue strips in bioreactors.

The Poisson ratio is an important parameter in the mechanical description of proteins by simplified continuum models, too. One idea could be the computation of the solvent excluding surface of proteins and the enclosed volume to derive a description of the volume change. This model could be then an enhancement to the here applied model.

Experimental improvement to measure alveolar strains is another important step to enhance model building and validation of models. To improve the measurement of strains, the tissue should have distinctive markers. Possible markers could be quantum dots or microscopic holes in the tissue, which are generated by bombardment of the tissue with micro-particles. In the latter case the magnitude and amount of particles must be carefully checked to ensure that mechanical properties are not changed. Indeed the best way to mark the tissue would be a fluorescence marker, which are located directly at focal adhesions.

Until now, the use of these markers have been successfully shown for single cell experiments, but not for tissue strips. Here an important step would be the development of a carrier which allows the infection of cells, located in their natural tissue, with the marker. This would have the great benefit that the strains between the focal adhesions are measured, which is exactly what is important.

The experimental data from the alveolar experiments can be also used as a basis for geometric reconstruction of alveoli. A possible meshed geometry can be seen in Figure 5.1. Here a linear connection between the measurement points was assumed. Additionally, connected walls to the edges of the alveoli were partially reconstructed as well. Surely more advanced methods could be used to reconstruct alveoli, though the automatic segmentation of the tissue is probably very difficult due to the brightness differences, which are inherent to fluorescence microscopy. However, using even simple models as the one shown here could allow more insight into the connection between cells and tissue, once a cellular layer is added on the inner surface of the alveoli.

The next step for further developing the here proposed mechanical models to mechanobiological models is the inclusion of biological motivated models. Examples are the calcium transport in the bronchioli or models, which describe the intracellular production and transport of inflammation related proteins. The basis for these models could be diffusion based models which describe the transport of proteins as concentration parameter. This would allow the simulation of a biochemical answer due to a mechanical stimulus. Careful investigations in the coupling of biochemical models to mechanical models are the basis of a comprehensive mechanobiological model.

Appendix A

Extension of the CHARMM 22 force field

New amino acids are added to the CHARMM 22 force field [89] in the topology file and the parameter file. The following are the extensions which have been used.

A.1 Hydroxyproline

Topology extension: *top_all22_prot.inp*

```
RESI HYP         0.00
GROUP                    !       HD1 HD2
ATOM N    N     -0.2900 !      |   \ /
ATOM CA   CP1    0.0200 !      N---CD  HG
ATOM HA   HB     0.0900 !      |    \  /
ATOM CD   CP3    0.1800 !      |     CG
ATOM HD1  HA     0.0000 !      |    /  \
ATOM HD2  HA     0.0000 !   HA-CA--CB  OG2--HG2
GROUP                    !      |   / \
ATOM C    C      0.5300 !      | HB1 HB2
ATOM O    O     -0.5300 !    O=C
GROUP                    !      |
ATOM CB   CP2   -0.1800
ATOM HB1  HA     0.0900
```

```
ATOM HB2  HA     0.0900
GROUP
ATOM CG   CP2    0.1400
ATOM HG   HA     0.0900
ATOM OG2  OH1   -0.6600
ATOM HG2  H      0.4300
BOND C CA C +N
BOND N CA CA CB CB CG CG CD N CD
BOND CA HA CB HB1 CB HB2 CD HD1 CD HD2 CG HG
BOND CG OG2 OG2 HG2
DOUBLE O C
IMPR N -C CA CD
IMPR C CA +N O                !IMPR N CA CD +C C CA N O
DONOR HG2 OG2
ACCEPTOR O C
IC CD  -C  *N   CA   1.4468 122.5296 -179.2170 122.5076 1.4550
IC N   CA  C    +N   1.4550 111.6376  -31.0428 120.0469 1.3161
IC +N  CA  *C   O    1.3161 120.0469 -179.5571 120.4223 1.2316
IC N   CA  CB   CG   1.4550 101.8808   29.6080 103.6605 1.5362
IC N   CA  CB   HB1  1.4550 101.8808  152.0681 112.9350 1.0925
IC N   CA  CB   HB2  1.4550 101.8808  -86.5729 108.9663 1.0930
IC CA  CB  CG   HG   1.5360 103.6605   79.0616 109.5554 1.0926
IC CD  N   CA   CB   1.4468 114.9587  -11.2918 101.8808 1.5360
IC CD  N   CA   HA   1.4468 114.9587 -129.2290 110.5162 1.0924
IC CD  N   CA   C    1.4468 114.9587  109.5875 111.6376 1.5380
IC HA  CA  N    -C   1.0924 110.5162   50.0429 122.5076 1.3162
IC CA  N   CD   CG   1.4550 114.9587  -11.8599 102.4794 1.5305
IC CA  N   CD   HD1  1.4550 114.9587 -131.8901 111.1069 1.0924
IC CA  N   CD   HD2  1.4550 114.9587  106.0401 109.5406 1.0925
IC N   CA  C    O    1.4550 111.6376  149.4002 120.4223 1.2316
IC CA  CB  CG   OG2  1.5360 103.6605 -158.7449 112.5784 1.4300
IC CD  CG  OG2  HG2  1.5305 112.2089   31.3937 109.5000 1.0300
IC N   CD  CG   CB   1.4468 102.4794   29.9288 103.3139 1.5362
PATCHING FIRS PROP
```

Parameter extension: *par_all22_prot.inp*

```
BONDS
...
OH1  CP2   428.000     1.4300 ! HYP
```

```
ANGLES
...
H    OH1  CP2   65.000   109.5000 ! HYP
OH1  CP2  CP2   50.000   112.5000 ! HYP
OH1  CP2  CP3   50.000   112.2000 ! HYP
OH1  CP2  HA    45.900   111.0000 ! HYP

DIHEDRALS
...
H    OH1  CP2  CP2      0.9900  2   180.00 ! HYP
H    OH1  CP2  CP3      0.9900  2   180.00 ! HYP
X    CP2  OH1  X        0.1400  3     0.00 ! HYP
```

A.2 Co^{2+}

Topology extension: *top_all22_prot.inp*

```
MASS   107 CO   58.933195 CO
...
RESI CO2       2.00
GROUP
ATOM CO   CO   2.00
PATCHING FIRST NONE LAST NONE
...
```

Parameter extension: *par_all22_prot.inp*

```
CO     0.000000  -0.014000     0.387249
```

ACE parameter extension: *acepar22_prot.inp*

```
CO 24.3296
```

Appendix B

Cubic spline fit of energy data

In order to get a continuous material formulation for the integrin description, the computed energy values are fitted with a spline function. This function is piecewise defined by polynomials. The equation for the interaction energy E_{int} is the following:

$$E_{int,p}(\lambda) = \sum_{i=0}^{3} c_i \cdot (\lambda - \lambda_p)^i \text{ for } \lambda_p < \lambda < \lambda_{p+1} \tag{B.1}$$

The spline coefficients are given in the following table:

p	λ^p	c_0	c_1	c_2	c_3
0	1.000	−921.54	257.50	0.00	$-2.71\ 10^5$
1	1.025	102.96	−250.52	−20320.67	$4.47\ 10^5$
2	1.050	462.21	−428.55	13199.48	−8766.97
3	1.075	−865.02	214.99	12541.96	$-3.97\ 10^5$
4	1.100	−615.26	96.83	−17268.10	$4.17\ 10^5$
5	1.125	−446.05	15.19	14002.45	$-1.08\ 10^5$
6	1.150	−1509.94	513.31	5922.30	$-3.69\ 10^5$
7	1.175	−620.29	117.12	−21770.07	$4.48\ 10^5$

8	1.200	−108.97	−131.94	11807.59	$-2.15\ 10^5$
9	1.225	−520.58	54.86	−4335.50	57806.64

Table B.1: Spline coifficients.

The original computed energy values are:

λ	E_{int}
1.000	−406.540
1.025	−404.336
1.050	−416.316
1.075	−418.917
1.100	−411.914
1.125	−413.771
1.150	−406.323
1.175	−395.558
1.200	−399.241
1.225	−398.523
1.250	−398.958

Table B.2: Interaction energies E_{int} with equilibration time $t_{equi} = 2\ ns$.

Bibliography

[1] M. Abramoff, P. Magelhaes, and S. Ram. Image processing with ImageJ. *Biophotonics International*, 11(7):36–42, Jul 2004.

[2] B. Alberts, D. Bray, J. Lewis, M. Raff, K. Roberts, and P. Walter. *Molecular Biology of the Cell*. Garland Science, 2002.

[3] G. Albu, W. Habre, F. Fontao, D. R. Morel, and F. Petak. The contribution of the pulmonary microvascular pressure in the maintenance of an open lung during mechanical ventilation. *Respir Physiol Neurobiol*, 157(2-3):262–269, Dec 2006.

[4] A. M. Alencar, S. P. Arold, S. V. Buldyrev, A. Majumdar, D. Stamenović, H. E. Stanley, and B. Suki. Physiology: Dynamic instabilities in the inflating lung. *Nature*, 417(6891):809–811, Jun 2002.

[5] R. Armunanto, C. Schwenk, A. Setiaji, and B. Rode. Classical and QM/MM molecular dynamics simulations of Co2+ in water. *Chemical Physics*, 295(1):63–70, Nov 2003.

[6] S. Badia, P. Bochev, R. Lehoucq, M. Parks, J. Fish, M. A. Nuggehally, and M. Gunzburger. A force-based blending model foratomistic-to-continuum coupling. *International Journal for Multiscale Computational Engineering*, 5(5):387–406, 2007.

[7] S. Badia, M. Parks, P. Bochev, M. Gunzburger, and R. Lehoucq. On atomistic-to-continuum coupling by blending. *Multiscale Model Sim*, 7(1):381–406, Jan 2008.

[8] J. Ball. Convexity conditions and existence theorems in nonlinearconvexity conditions and existence theorems in nonlinear elasticity. *Archive for Rational Mechanics and Analysis*, 63(4):337–403, Dec 1977.

[9] G. Bao and S. Suresh. Cell and molecular mechanics of biological materials. *Nat Mater*, 2(11):715–725, Nov 2003.

[10] M. Bathe. A finite element framework for computation of protein normal modes and mechanical response. *Proteins*, 70(4):1595–1609, Mar 2008.

[11] T. Belytschko and S. Xiao. Coupling methods for continuum model with molecular model. *International Journal for Multiscale Computational Engineering*, 1(1):1543–1649, Jan 2003.

[12] Benninghoff and Drenckhahn. *Anatomie: Makroskopische Anatomie, Histologie, Embryologie, Zellbiologie.* Urban & Fischer Verlag/Elsevier GmbH, 2003.

[13] H. M. Berman, J. Westbrook, Z. Feng, G. Gilliland, T. N. Bhat, H. Weissig, I. N. Shindyalov, and P. E. Bourne. The protein data bank. *Nucleic Acids Res*, 28(1):235–42, Jan 2000.

[14] A. A. Birukova, S. Chatchavalvanich, A. Rios, K. Kawkitinarong, J. G. Garcia, and K. G. Birukov. Differential regulation of pulmonary endothelial monolayer integrity by varying degrees of cyclic stretch. *Am J Pathol*, 168(5):1749–1761, May 2006.

[15] D. Boal. *Mechanics of the Cell.* Cambridge University Press, 2001.

[16] J. Bonet and R. Wood. Nonlinear continuum mechanics for finite element analysis. *Cambridge University Press*, 2004.

[17] A. Bremer, R. C. Millonig, R. Sütterlin, A. Engel, T. D. Pollard, and U. Aebi. The structural basis for the intrinsic disorder of the actin filament: the "lateral slipping" model. *J Cell Biol*, 115(3):689–703, Nov 1991.

[18] K. K. Brewer, H. Sakai, A. M. Alencar, A. Majumdar, S. P. Arold, K. R. Lutchen, E. P. Ingenito, and B. Suki. Lung and alveolar wall elastic and hysteretic behavior in rats: effects of in vivo elastase treatment. *J Appl Physiol*, 95(5):1926–36, Nov 2003.

[19] B. Brooks, R. Bruccoleri, B. Olafson, D. States, S. Swaminathan, and M. Karplus. Charmm - a program for macromolecular energy, minimization, and dynamics calculations. *J Comput Chem*, 4(2):187–217, Jan 1983.

[20] A. Buckingham. The hydrogen bond, and the structure and properties of H_2O and $(H_2O)_2$. *Journal of Molecular Structure*, 250(2-4):111–118, Nov 1991.

[21] J. P. Butler, H. Miki, S. Squarcia, R. A. Rogers, and J. L. Lehr. Effect of macroscopic deformation on lung microstructure. *J Appl Physiol*, 81(4):1792–1799, Oct 1996.

[22] J. P. Butler, I. M. Tolic-Norrelykke, B. Fabry, and J. J. Fredberg. Traction fields, moments, and strain energy that cells exert on their surroundings. *Am J Physiol Cell Physiol*, 282(3):C595–C605, Mar 2002.

[23] N. Calimet, M. Schaefer, and T. Simonson. Protein molecular dynamics with the generalized Born/ACE solvent models. *Proteins*, 45(2):144–158, Nov 2001.

[24] D. Carney, J. DiRocco, and G. Nieman. Dynamic alveolar mechanics and ventilator-induced lung injury. *Crit Care Med*, 33(3 Suppl):S122–128, Mar 2005.

[25] F. S. A. Cavalcante, S. Ito, K. Brewer, H. Sakai, A. M. Alencar, M. P. Almeida, J. S. Andrade, A. Majumdar, E. P. Ingenito, and B. Suki. Mechanical interactions between collagen and proteoglycans: implications for the stability of lung tissue. *J Appl Physiol*, 98(2):672–679, Feb 2005.

[26] P. Chandran, C. Wolf, and M. Mofrad. Band-like stress fiber propagation in a continuum and implications for myosin contractile stresses. *Cellular and Molecular Bioengineering*, 2(1):13–27, Mar 2009.

[27] B. T. Chen, A. T. Yordanov, and G. A. Johnson. Ventilation-synchronous magnetic resonance microscopy of pulmonary structure and ventilation in mice. *Magn Reson Med*, 53(1):69–75, Jan 2005.

[28] X. Chen, Q. Cui, Y. Tang, J. Yoo, and A. Yethiraj. Gating mechanisms of mechanosensitive channels of large conductance, I: a continuum mechanics-based hierarchical framework. *Biophys J*, 95(2):563–580, Jul 2008.

[29] D. Chiumello, E. Carlesso, P. Cadringher, P. Caironi, F. Valenza, F. Polli, F. Tallarini, P. Cozzi, M. Cressoni, A. Colombo, J. J. Marini, and L. Gattinoni. Lung stress and strain during mechanical ventilation for acute respiratory distress syndrome. *Am J Respir Crit Care Med*, 178(4):346–355, Aug 2008.

[30] J. Chu, B. Trout, and B. Brooks. A super-linear minimization scheme for the nudged elastic band method. *J Chem Phys*, 119(24):12708–12717, Jan 2003.

[31] M. M. A. E. Claessens, M. Bathe, E. Frey, and A. R. Bausch. Actin-binding proteins sensitively mediate f-actin bundle stiffness. *Nat Mater*, 5(9):748–753, Sep 2006.

[32] E. Clark and J. Brugge. Integrins and signal transduction pathways: the road taken. *Science*, 268(5208):233–239, Apr 1995.

[33] K. J. Clemetson and J. M. Clemetson. Integrins and cardiovascular disease. *Cell Mol Life Sci*, 54(6):502–513, Jun 1998.

[34] D. Craig, M. Gao, K. Schulten, and V. Vogel. Structural insights into how the MIDAS ion stabilizes integrin binding to an RGD peptide under forces. *Structure*, 12(11):2049–2058, Nov 2004.

[35] A. Curtis. Cell forces in tissues. *Med Eng Phys*, 27(9):773–779, Nov 2005.

[36] L. Curtiss, D. Frurip, and M. Blander. Studies of molecular association in H_2O and D_2O vapors by measurement of thermal conductivity. *J. Chem. Phys.*, 71(6):2703–2711, Sep 1979.

[37] H. Dailey and S. Ghadiali. Multi-scale modeling of cellular deformation and adhesion during acute lung injury. *J Biomech*, 39(Suppl 1):S599–S599, Aug 2006.

[38] H. L. Dailey and S. N. Ghadiali. Influence of power-law rheology on cell injury during microbubble flows. *Biomech Model Mechanobiol*, 9(3):263–279, Jun 2010.

[39] H. L. Dailey, L. M. Ricles, H. C. Yalcin, and S. N. Ghadiali. Image-based finite element modeling of alveolar epithelial cell injury during airway reopening. *J. Appl. Physiol.*, 106(1):221–232, Jan 2009.

[40] E. H. J. Danen and A. Sonnenberg. Integrins in regulation of tissue development and function. *J Pathol*, 200(4):471–480, Jul 2003.

[41] J. de Rijdt and F. van Duijneveldt. Convergence to the basis-set limit in ab initio calculations at the correlated level on the water dimer. *J Chem Phys*, 97(7):5019–5030, Oct 1992.

[42] S. Deguchi, T. Ohashi, and M. Sato. Tensile properties of single stress fibers isolated from cultured vascular smooth muscle cells. *J Biomech*, 39(14):2603–2610, Jan 2006.

[43] V. S. Deshpande, R. M. McMeeking, and A. G. Evans. A bio-chemo-mechanical model for cell contractility. *Proc Natl Acad Sci*, 103(38):14015–14020, Sep 2006.

[44] V. S. Deshpande, R. M. McMeeking, and A. G. Evans. A model for the contractility of the cytoskeleton including the effects of stress-fibre formation and dissociation. *Proceedings of the Royal Society A: Mathematical, Physical and Engineering Sciences*, 463(2079):787 – 815, Mar 2007.

[45] G. Diercksen. SCF-MO-LCGO studies on hydrogen bonding. the water dimer. *Theoretical Chemistry Accounts: Theory, Computation, and Modeling (Theoretica Chimica Acta)*, 21(4):335–367, Dec 1971.

[46] J. D. DiRocco, L. A. Pavone, D. E. Carney, C. J. Lutz, L. A. Gatto, S. K. Landas, and G. F. Nieman. Dynamic alveolar mechanics in four models of lung injury. *Intensive Care Med*, 32(1):140–148, Jan 2006.

[47] M. S. Dunnill. Effect of lung inflation on alveolar surface area in the dog. *Nature*, 214(5092):1013, Jun 1967.

[48] M. Eastwood, D. A. McGrouther, and R. A. Brown. A culture force monitor for measurement of contraction forces generated in human dermal fibroblast cultures: evidence for cell-matrix mechanical signalling. *Biochim Biophys Acta*, 1201(2):186–192, Nov 1994.

[49] J. Emsley, S. L. King, J. M. Bergelson, and R. C. Liddington. Crystal structure of the I domain from integrin $\alpha_2\beta_1$. *J Biol Chem*, 272(45):28512–28517, Nov 1997.

[50] J. Emsley, C. G. Knight, R. W. Farndale, M. J. Barnes, and R. C. Liddington. Structural basis of collagen recognition by integrin $\alpha_2\beta_1$. *Cell*, 101(1):47–56, Mar 2000.

[51] P. Fratzl, K. Misof, I. Zizak, G. Rapp, H. Amenitsch, and S. Bernstorff. Fibrillar structure and mechanical properties of collagen. *J Struct Biol*, 122(1-2):119–122, 1998.

[52] J. J. Fredberg and R. D. Kamm. Stress transmission in the lung: Pathways from organ to molecule. *Annu Rev Physiol*, 68:507–541, Mar 2006.

[53] O. Gajic, J. Lee, C. H. Doerr, J. C. Berrios, J. L. Myers, and R. D. Hubmayr. Ventilator-induced cell wounding and repair in the intact lung. *Am J Respir Crit Care Med*, 167(8):1057–1063, Apr 2003.

[54] M. Gao, M. Sotomayor, E. Villa, E. H. Lee, and K. Schulten. Molecular mechanisms of cellular mechanics. *Physical Chemistry Chemical Physics*, 8(32):3692–706, Aug 2006.

[55] T. C. Gasser, R. W. Ogden, and G. A. Holzapfel. Hyperelastic modelling of arterial layers with distributed collagen fibre orientations. *J R Soc Interface*, 3(6):15–35, Feb 2006.

[56] J. Haile. *Molecular Dynamics Simulation*. Wiley, 1997.

[57] B. Han, M. Lodyga, and M. Liu. Ventilator-induced lung injury: Role of protein-protein interaction in mechanosensation. *Proc Am Thorac Soc*, 2(3):181–187, Oct 2005.

[58] T. Hawkins, M. Mirigian, M. S. Yasar, and J. L. Ross. Mechanics of microtubules. *J Biomech*, 43(1):23–30, Jan 2010.

[59] A. V. Hill. The heat of shortening and the dynamic constants of muscle. *Proceedings of the Royal Society B: Biological Sciences*, 126(843):136–195, Oct 1938.

[60] G. A. Holzapfel. *Nonlinear Solid Mechanics*. Wiley, 2000.

[61] G. A. Holzapfel, T. C. Gasser, and R. W. Ogden. A new constitutive framework for arterial wall mechanics and a comparative study of material models. *Journal of Elasticity*, 61(1-3):1–48, Jul 2000.

[62] F. G. Hoppin, G. C. Lee, and S. V. Dawson. Properties of lung parenchyma in distortion. *J Appl Physiol*, 39(5):742–751, Nov 1975.

[63] G. Hummer and A. Szabo. Kinetics from nonequilibrium single-molecule pulling experiments. *Biophys J*, 85(1):5–15, Jul 2003.

[64] J. D. Humphrey. On mechanical modeling of dynamic changes in the structure and properties of adherent cells. *Mathematics and Mechanics of Solids*, 7(5):521–539, 2002.

[65] W. Humphrey, A. Dalke, and K. Schulten. VMD: visual molecular dynamics. *J Mol Graph*, 14(1):33–8, 27–8, Feb 1996.

[66] D. E. Ingber. Integrins as mechanochemical transducers. *Curr Opin Cell Biol*, 3(5):841–848, Oct 1991.

[67] D. E. Ingber. How cells (might) sense microgravity. *FASEB J*, 13(9001):3–15, May 1999.

[68] D. E. Ingber. Tensegrity I. cell structure and hierarchical systems biology. *J Cell Sci*, 116(7):1157–1173, Apr 2003.

[69] D. E. Ingber. Tensegrity II. how structural networks influence cellular information processing networks. *J Cell Sci*, 116(8):1397–1408, Apr 2003.

[70] D. E. Ingber. Cellular mechanotransduction: putting all the pieces together again. *FASEB J*, 20(7):811–827, May 2006.

[71] M. Itskov, A. Ehret, and D. Mavrilas. A polyconvex anisotropic strain energy function for soft collagenous tissues. *Biomech Model Mechanobiol*, 5(1):17–26, Mar 2006.

[72] R. A. Jamal, P. J. Roughley, and M. S. Ludwig. Effect of glycosaminoglycan degradation on lung tissue viscoelasticity. *Am J Physiol Lung Cell Mol Physiol*, 280(2):L306–315, Feb 2001.

[73] G. A. Jeffrey. *An introduction to hydrogen bonding*. Oxford University Press, Jan 1997.

[74] J. Jones. On the determination of molecular field. II. From the equation of state of a gas. *Proceedings of the Royal Society of London. Series A*, 106(738):463–477, Oct 1924.

[75] R. D. Kamm and M. R. Kaazempur-Mofrad. On the molecular basis for mechanotransduction. *Mech Chem Biosyst*, 1(3):201–209, Sep 2004.

[76] T. G. Klingele and N. C. Staub. Alveolar shape changes with volume in isolated, air-filled lobes of cat lung. *J Appl Physiol*, 28(4):411–414, Apr 1970.

[77] T. Koch, T. Nguyen, J. Pauli, C. Mierke, J. Butler, J. Fredberg, and B. Fabry. Force generated by the isolated smooth muscle cell in a three-dimensional collagen gel. *J Biomech*, 39 (Suppl 1):S234, Jul 2006.

[78] J. Korsgaard. On the representation of symmetric tensor-valued isotropic functions. *Int J Eng Sci*, 28(12):1331–1346, Jun 1990.

[79] J. Korsgaard. On the representation of two-dimensional isotropic functions. *Int J Eng Sci*, 28(7):653–662, 1990.

[80] A. Krammer, H. Lu, B. Isralewitz, K. Schulten, and V. Vogel. Forced unfolding of the fibronectin type III module reveals a tensile molecular recognition switch. *Proc Natl Acad Sci USA*, 96(4):1351–1356, Feb 1999.

[81] C. Kritayakornupong, K. Plankensteiner, and B. Rode. Structural and dynamical properties of Co(III) in aqueous solution: Ab initio quantum mechanical/molecular mechanical molecular dynamics simulations. *J Chem Phys*, 119(12):6068–6072, Sep 2003.

[82] C. Lambert, B. Nusgens, and C. Lapiere. Mechano-sensing and mechano-reaction of soft connective tissue cells. *Adv Space Res*, 21(8-9):1081–1091, 1998.

[83] V. M. Laurent, S. Henon, E. Planus, R. Fodil, M. Balland, D. Isabey, and F. Gallet. Assessment of mechanical properties of adherent living cells by bead micromanipulation: Comparison of magnetic twisting cytometry vs optical tweezers. *J Biomech Eng*, 124(4):408–421, Aug 2002.

[84] E. H. Lee, J. Hsin, M. Sotomayor, G. Comellas, and K. Schulten. Discovery through the computational microscope. *Structure*, 17(10):1–12, Oct 2009.

[85] F. Li, S. D. Redick, H. P. Erickson, and V. T. Moy. Force measurements of the $\alpha_5\beta_1$ integrin-fibronectin interactions. *Biophys J*, 84(2):1252–1262, Feb 2003.

[86] C. Lim, E. Zhou, and S. Quek. Mechanical models for living cells–a review. *J Biomech*, 39(2):195–216, 2006.

[87] H. D. Litzlbauer, C. Neuhaeuser, A. Moell, S. Greschus, A. Breithecker, F. E. Franke, W. Kummer, and W. S. Rau. Three-dimensional imaging and morphometric analysis of alveolar tissue from microfocal x-ray-computed tomography. *Am J Physiol Lung Cell Mol Physiol*, 291(3):L535–545, Sep 2006.

[88] F. London. Properties an applications of molecular forces. *Z Phys Chem B*, 11:222–251, 1930.

[89] A. MacKerell, D. Bashford, M. Bellott, R. Dunbrack, J. Evanseck, M. Field, S. Fischer, J. Gao, H. Guo, S. Ha, D. Joseph-McCarthy, L. Kuchnir, K. Kuczera, F. Lau, C. Mattos, S. Michnick, T. Ngo, D. Nguyen, B. Prodhom, W. Reiher, B. Roux, M. Schlenkrich, J. Smith, R. Stote, J. Straub, M. Watanabe, J. Wiorkiewicz-Kuczera, D. Yin, and M. Karplus. All-atom empirical potential for molecular modeling and dynamics studies of proteins. *J Phys Chem B*, 102(18):3586–3616, Jan 1998.

[90] J. N. Maina and J. B. West. Thin and strong! The bioengineering dilemma in the structural and functional design of the blood-gas barrier. *Physiol. Rev.*, 85(3):811–844, Jul 2005.

[91] C. Martin, S. Uhlig, and V. Ullrich. Videomicroscopy of methacholine-induced contraction of individual airways in precision-cut lung slices. *Eur Respir J*, 9(12):2479–87, Dec 1996.

[92] R. J. Mason. Biology of alveolar type II cells. *Respirology*, 11(Suppl 1):S12–S15, Jan 2006.

[93] S. Meissner, L. Knels, and E. Koch. Improved three-dimensional fourier domain optical coherence tomography by index matching in alveolar structures. *J Biomed Opt*, 14(6):064037, Jan 2009.

[94] S. Meissner, L. Knels, A. Krueger, T. Koch, and E. Koch. Simultaneous three-dimensional optical coherence tomography and intravital microscopy for imaging subpleural pulmonary alveoli in isolated rabbit lungs. *J Biomed Opt*, 14(5):054020, Jan 2009.

[95] S. Meissner, L. Knels, C. Schnabel, T. Koch, and E. Koch. Three-dimensional fourier domain optical coherence tomography in vivo imaging of alveolar tissue in the intact thorax using the parietal pleura as a window. *J Biomed Opt*, 15(1):016030, Jan 2010.

[96] M. Mertens, A. Tabuchi, S. Meissner, A. Krueger, K. Schirrmann, U. Kertzscher, A. R. Pries, A. S. Slutsky, E. Koch, and W. M. Kuebler. Alveolar dynamics in acute lung injury: heterogeneous distension rather than cyclic opening and collapse. *Crit Care Med*, 37(9):2604–2611, Sep 2009.

[97] R. Metzke, H. Runck, C. Stahl, B. Schillinger, E. Calzada, M. Mühlbauer, M. Schulz, M. Schneider, H.-J. Priebe, W. Wall, and J. Guttmann. Neutron computed tomography of rat lungs. *Phys. Med. Biol.*, 56:N1, Jan 2011.

[98] S. M. Mijailovich, D. Stamenović, R. Brown, D. E. Leith, and J. J. Fredberg. Dynamic moduli of rabbit lung tissue and pigeon ligamentum propatagiale undergoing uniaxial cyclic loading. *J Appl Physiol*, 76(2):773–782, Feb 1994.

[99] R. E. Miller and E. B. Tadmor. A unified framework and performance benchmark of fourteen multiscale atomistic/continuum coupling methods. *Model Simul Mater Sc*, 17(5):053001, Jan 2009.

[100] W. Mitzner, J. Fallica, and J. Bishai. Anisotropic nature of mouse lung parenchyma. *Ann Biomed Eng*, 36(12):2111–2120, Dec 2008.

[101] M. K. Mofrad and R. Kamm. *Cytoskeletal Mechanics: Models and Measurements*. Cambridge University Press, 2006.

[102] A. Mogilner and G. Oster. Cell motility driven by actin polymerization. *Biophys J*, 71(6):3030–3045, Dec 1996.

[103] A. Moretto, M. Dallaire, P. Romero, and M. Ludwig. Effect of elastase on oscillation mechanics of lung parenchymal strips. *J Appl Physiol*, 77(4):1623–1629, Oct 1994.

[104] C. B. Morrey. Quasi-convexity and the lower semicontinuity of multiple integrals. *Pacific Journal of Mathematics*, 2(1):25–53, 1952.

[105] F. H. Netter. *Farbatlanten der Medizin: Atmungsorgane*. Thieme Georg Verlag, 1982.

[106] J. Odutola and T. Dyke. Partially deuterated water dimers: Microwave spectra and structure. *J Chem Phys*, 72(9):5062–5070, May 1980.

[107] P. Pelosi, P. R. M. Rocco, D. Negrini, and A. Passi. The extracellular matrix of the lung and its role in edema formation. *An Acad Bras Cienc*, 79(2):285–297, Jun 2007.

[108] C. E. Perlman and J. Bhattacharya. Alveolar expansion imaged by optical sectioning microscopy. *J. Appl. Physiol.*, 103(3):1037–1044, Sep 2007.

[109] T. D. Pollard. Rate constants for the reactions of ATP- and ADP-actin with the ends of actin filaments. *J Cell Biol*, 103(6):2747–2754, Dec 1986.

[110] S. M. Rausch, D. Haberthur, M. Stampanoni, J. C. Schittny, and W. A. Wall. Local strain distribution in real three-dimensional alveolar geometries. *Ann Biomed Eng*, 39(11):2835–2843, Nov 2011.

[111] S. M. Rausch, C. Martin, P. B. Bornemann, S. Uhlig, and W. A. Wall. Material model of lung parenchyma based on living precision-cut lung slice testing. *J Mech Behav Biomed Mater*, 4(4):583–592, May 2011.

[112] A. R. Ressmeyer, A. K. Larsson, E. Vollmer, S. E. Dahlèn, S. Uhlig, and C. Martin. Characterisation of guinea pig precision-cut lung slices: comparison with human tissues. *Eur Respir J*, 28(3):603–611, Sep 2006.

[113] F. Rico, P. Roca-Cusachs, N. Gavara, R. Farre, M. Rotger, and D. Navajas. Probing mechanical properties of living cells by atomic force microscopy with blunted pyramidal cantilever tips. *Phys. Rev. E*, 72(2):021914, Aug 2005.

[114] E. L. Ritman. Micro-computed tomography of the lungs and pulmonary-vascular system. *Proc Am Thorac Soc*, 2(6):477–480, Jan 2005.

[115] U. R. Rodgers and A. S. Weiss. Cellular interactions with elastin. *Pathol. Biol.*, 53(7):390–398, Sep 2005.

[116] M. Schaefer, C. Bartels, F. Leclerc, and M. Karplus. Effective atom volumes for implicit solvent models: comparison between Voronoi Volumes and Minimum Fluctation Volumes. *J Comput Chem*, 22(15):1857–1879, Jan 2001.

[117] M. Schaefer and M. Karplus. A comprehensive analytical treatment of continuum electrostatics. *Journal of Physical Chemistry*, 100(5):1578–1599, Feb 1996.

[118] S. Scheiner. Ab initio studies of hydrogen bonds: the water dimer paradigm. *Annu Rev Phys Chem*, 45:23–56, Jan 1994.

[119] K. Schenke-Layland. Non-invasive multiphoton imaging of extracellular matrix structures. *J Biophotonics*, 1(6):451–462, Dec 2008.

[120] B. Schillinger, E. Calzada, and F. Grünauer. The design of the neutron radiography and tomography facility at the new research reactor FRM-II at Technical University Munich. *Int J Radiat Applic Instrum, Part A*, 61(4):653–657, Oct 2004.

[121] J. Schröder and P. Neff. Invariant formulation of hyperelastic transverse isotropy based on polyconvex free energy functions. *Int J Solids Struct*, 40(2):401–445, 2003.

[122] J. Schröder and P. Neff. On the construction of polyconvex anisotropic free energy functions. *IUTAM Symposium on Computational Mechanics of Solid Materials at Large Strains*, 108:171–180, Aug 2003.

[123] S. Schumann, C. A. Stahl, K. Möller, M. Schneider, R. Metzke, W. A. Wall, H. J. Priebe, and J. Guttmann. Contact-free determination of material characteristics using a newly developed pressure-operated strain-applying bioreactor. *J Biomed Mater Res B Appl Biomater*, 86(2):483–492, Aug 2008.

[124] M. Schutz, S. Brdarski, P.-O. Widmark, R. Lindh, and G. Karlstrom. The water dimer interaction energy: Convergence to the basis set limit at the correlated level. *J Chem Phys*, 107(12):4597–4605, Sep 1997.

[125] K. Silverstein, A. Haymet, and K. Dill. A simple model of water and the hydrophobic effect. *Journal of the American Chemical Society*, 120(13):3166–3175, Apr 1998.

[126] K. Silverstein, A. Haymet, and K. Dill. The strength of hydrogen bonds in liquid water and around nonpolar solutes. *Journal of American Chemical Society*, 122(33):8037–8041, Aug 2000.

[127] S. Skrzyński, A. Sionkowska, and A. Marciniak. DSC study of collagen in disc disease. *J Biophys*, 2009:819635, Jan 2009.

[128] A. J. M. Spencer. *Applications of Tensor Functions in Solid Mechanics*, chapter Isotropic Polynomial Invariants and Tensor Functions. Springer Verlag, 1987.

[129] J. Stricker, T. Falzone, and M. L. Gardel. Mechanics of the f-actin cytoskeleton. *J Biomech*, 43(1):9–14, Jan 2010.

[130] T. Sugihara, J. Hildebrandt, and C. J. Martin. Viscoelastic properties of alveolar wall. *J Appl Physiol*, 33(1):93–98, Jul 1972.

[131] B. Suki, A. L. Barabási, Z. Hantos, F. Peták, and H. E. Stanley. Avalanches and power-law behaviour in lung inflation. *Nature*, 368(6472):615–618, Apr 1994.

[132] B. Suki, S. Ito, D. Stamenovic, K. R. Lutchen, and E. P. Ingenito. Biomechanics of the lung parenchyma: critical roles of collagen and mechanical forces. *J Appl Physiol*, 98(5):1892–1899, May 2005.

[133] B. Suki, K. R. Lutchen, and E. P. Ingenito. On the progressive nature of emphysema: Roles of proteases, inflammation, and mechanical forces. *Am J Respir Crit Care Med*, 168(5):516–521, Jun 2003.

[134] T. M. Svitkina, E. A. Bulanova, O. Y. Chaga, D. M. Vignjevic, S. ichiro Kojima, J. M. Vasiliev, and G. G. Borisy. Mechanism of filopodia initiation by reorganization of a dendritic network. *J Cell Biol*, 160(3):409–21, Feb 2003.

[135] A. Tabuchi, M. Mertens, H. Kuppe, A. R. Pries, and W. M. Kuebler. Intravital microscopy of the murine pulmonary microcirculation. *J Appl Physiol*, 104(2):338–346, Feb 2008.

[136] Y. Tang, G. Cao, X. Chen, J. Yoo, A. Yethiraj, and Q. Cui. A finite element framework for studying the mechanical response of macromolecules: Application to the gating of the mechanosensitive channel MscL. *Biophys J*, 91(4):1248–1263, Jan 2006.

[137] Y. Tang, J. Yoo, A. Yethiraj, Q. Cui, and X. Chen. Gating mechanisms of mechanosensitive channels of large conductance, II: systematic study of conformational transitions. *Biophys J*, 95(2):581–596, Jul 2008.

[138] A. Taubenberger, D. A. Cisneros, J. Friedrichs, P.-H. Puech, D. J. Muller, and C. M. Franz. Revealing early steps of $\alpha_2\beta_1$ integrin-mediated adhesion to collagen type I by using single-cell force spectroscopy. *Mol Biol Cell*, 18(5):1634–1644, May 2007.

[139] The Acute Respiratory Distress Syndrome Network. Ventilation with lower tidal volumes as compared with traditional tidal volumes for acute lung injury and the acute respiratory distress syndrome. the acute respiratory distress syndrome network. *N Engl J Med*, 342(18):1301–1308, May 2000.

[140] X. Trepat, M. Grabulosa, F. Puig, G. N. Maksym, D. Navajas, and R. Farre. Viscoelasticity of human alveolar epithelial cells subjected to stretch. *Am J Physiol Lung Cell Mol Physiol*, 287(5):L1025–1034, Jul 2004.

[141] X. Trepat, F. Puig, N. Gavara, J. J. Fredberg, R. Farre, and D. Navajas. Effect of stretch on the structural integrity and micromechanics of human alveolar epithelial cell monolayers exposed to thrombin. *Am J Physiol Lung Cell Mol Physiol*, 290(6):L1104–1110, Jun 2006.

[142] D. J. Tschumperlin, F. Boudreault, and F. Liu. Recent advances and new opportunities in lung mechanobiology. *J Biomech*, 43(1):99–107, Jan 2010.

[143] S. Uhlig. Ventilation-induced lung injury and mechanotransduction: stretching it too far? *Am J Physiol Lung Cell Mol Physiol*, 282(5):L892–896, May 2002.

[144] A. Vedani and D. Huhta. A new force-field for modeling metalloproteins. *Journal of the American Chemical Society*, 112(12):4759–4767, Jan 1990.

[145] J. Wackerfuss. Molecular mechanics in the context of the finite element method. *Int J Numer Meth Eng*, 77(7):969–997, Jan 2009.

[146] W. Wall, L. Wiechert, A. Comerford, and S. Rausch. Towards a comprehensive computational model for the respiratory system. *Int J Numer Method Biomed Eng*, 26(7):807–827, Jul 2010.

[147] J. Wang and J.-S. Lin. Cell traction force and measurement methods. *Biomech Model Mechanobiol*, 6(6):361–371, 2007.

[148] Z. Wei, V. S. Deshpande, R. M. McMeeking, and A. G. Evans. Analysis and interpretation of stress fiber organization in cells subject to cyclic stretch. *J Biomech Eng*, 130(3):031009, Jun 2008.

[149] J. K. Weigel, D. Steinmann, P. Emerich, C. A. Stahl, D. v Elverfeldt, and J. Guttmann. High-resolution three-dimensional 19f-magnetic resonance imaging of rat lung in situ: evaluation of airway strain in the perfluorocarbon-filled lung. *Physiol Meas*, 32(2):251–262, Feb 2011.

[150] L. Wiechert, R. Metzke, and W. Wall. Modeling the mechanical behavior of lung tissue at the microlevel. *J Eng Mech*, 135(5):434–439, May 2009.

[151] S. Xantheas. On the importance of the fragment relaxation energy terms in the estimation of the basis set superposition error correction to the intermolecular interaction energy. *J Chem Phys*, 104(21):8821–8824, Jun 1996.

[152] S. Xiao and T. Belytschko. A bridging domain method for coupling continua with molecular dynamics. *Computer Methods in Applied Mechanics and Engineering*, 193(17-20):1645–1669, May 2004.

[153] T. Yang and M. H. Zaman. Free energy landscape of receptor-mediated cell adhesion. *J Chem Phys*, 126(4):045103, Jan 2007.

[154] H. Yuan, E. Ingenito, and B. Suki. Dynamic properties of lung parenchyma: mechanical contributions of fiber network and interstitial cells. *J Appl Physiol*, 83(5):1420–1431, Nov 1997.

[155] H. Yuan, S. Kononov, F. Cavalcante, K. Lutchen, E. Ingenito, and B. Suki. Effects of collagenase and elastase on the mechanical properties of lung tissue strips. *J Appl Physiol*, 89(1):3–14, Jul 2000.

[156] M. H. Zaman. Understanding the molecular basis for differential binding of integrins to collagen and gelatin. *Biophys J*, 92(2):L17–19, Jan 2007.

[157] C. Zhu, G. Bao, and N. Wang. Cell mechanics: mechanical response, cell adhesion, and molecular deformation. *Annu Rev Biomed Eng*, 2:189–226, Aug 2000.

[158] J. Zielkiewicz. Structural properties of water: comparison of the SPC, SPCE, TIP4P, and TIP5P models of water. *J. Chem. Phys.*, 123(10):104501, Sep 2005.